# Improving the sparks assisted chemical engraving (SACE) for industrial application

Frédéric Charbonneau

A Thesis

In

The Department

of

Mechanical and Industrial Engineering

Presented in Partial Fulfillment of the Requirements

for the Degree of Master of Applied Science

Concordia University

Montréal, Québec, Canada

November 2016

CONCORDIA UNIVERSITY
School of Graduate Studies

This is to certify that the thesis prepared

By: _____

Entitled: _____

and submitted in partial fulfillment of the requirements for the degree of

_____

complies with the regulations of the University and meets the accepted standards with respect to originality and quality.

Signed by the final examining committee:

_____ Chair
Dr. Robin .L. Drew, PhD

_____ Examiner
Dr. Luc Stafford, PhD

_____ Examiner
Dr. Sivakumar Narayanswamy, PhD

_____ Supervisor
Dr. Rolf Wuthrich, PhD

Approved by _____
Chair of Department or Graduate Program Director

_____
Dean of Faculty

Date _____

# Abstract


## Improving the SACE machining for industrial application

Frédéric Charbonneau,

Parameters influencing the discharge phenomenon and the etch capability of Sparks-Assisted Chemical Engraving (SACE) have been investigated in the last decade for a potential industrial application of this technology. Recently, Posalux SA, a company who evolves in the high-tech machine tool field, began the development of a commercial machine which uses the SACE process to etch glass. Since, the first commercialization of SACE, future customers' needs have to be taken into account: the initial cost of the machine, the process cost, the machining speed, the reproducibility, the quality of the machining. The cost of the machine is determined by the company who work with customers to find a good compromise between the cost and the performances. Therefore, this thesis focus on the three other characteristics (the process cost, the machining speed and the quality of the machining). Those characteristics can be improved by tuning the parameters used during the machining such as: proprieties of the electrical signal, tool geometry, electrolyte type, electrolyte flow, machining strategy, etc. The optimization of those parameters has the benefit of not changing the mechanical structure of the commercial machine (not invasive). Therefore, this work contributes in the development of the technology by providing a way to optimize the process, found the interaction between the parameters, found a scientific explanation for this optimization and provide some prove of concept for the industrial application of the process. Special attention has been devoted to the use of a square electrical signal with an offset. Those variables have been empirically optimized to increase the machining quality and the machining speed. Based on those results, an explanation model was developed to describe the process. This explanation is based on direct observation, optical emission spectroscopy and thermodynamic considerations.

# Acknowledgements

I take the opportunity to acknowledge the support and assistance of the people who had faith in me and without who this work would not have been possible.

A special mention to my supervisor, Professor Rolf Wüthrich, who believed in my capability and my work. He gave me his trust to accomplish the task and follow my instinct. Rolf, your knowledge and your experience were a substantial help in the accomplishment of my research.

A big thanks for my colleagues for their support and the useful project discussions, especially Lucas Hof, Andrew Morisson and Masiar Rahman. Also, I will thank the technician's team of Concordia University for their technical support and to make available useful equipment's, especially Gilles Huard and Robert Oliver. I would like to also thank Professor Luc Stafford and his team for the great help and experience in spectroscopy. Without them a big picture of the SACE machining will be unknown. A great thank you goes to Posalux SA (Switzerland) and their team, for their financial support. Posalux SA is a company that well understand the importance of the R&D to keep the head in the technology development.

In last but not less a big thank to my parents who always support me and believe in me. Without all your encouragement this thesis would never have been accomplished. You have been my moral support and my inspiration. Also, I would like to mention my brother, all member of my family and my friends who support me in difficult moment, they know who there are!

I will thank you all my life…

*Frédéric Charbonneau*

# Remerciements

J'aimerais prendre le temps pour remercier tous ceux et celles qui m'ont supporté et ont cru en moi tout au long de ma maîtrise.

Une mention spéciale pour mon superviseur, Professeur Rolf Wüthrich qui a su croire en mes capacités à accomplir la tâche. Grâce à sa supervision et à son expertise cette thèse a pu être réalisée.

Un gros merci à mes collègues pour leur aide tant au niveau technique qu'intellectuel sans quoi la réalisation de ce document aurait été difficile. Je remercie en particulier Lucas Hof, Andrews Morisson et Masiar Rahman. Je remercie aussi l'équipe de techniciens de l'Université Concordia, Gilles Huard et Robert Oliver, pour leur support technique et pour avoir mis à ma disposition des équipements essentiels. Je suis reconnaissant au Professeur Luc Stafford et à son équipe du département de physique de l'Université de Montréal pour avoir mis à ma disposition des équipements d'étude spectroscopique et pour leur expertise. Cette aide a été d'un apport considérable à la compréhension des principes physiques impliqués dans le processus SACE. Mais encore, je remercie Posalux SA (Suisse) pour l'aide financière qu'il apporte à notre groupe de recherche. Posalux SA est une compagnie qui sait voir l'importance de la R&D pour rester à la fine pointe de la technologie.

Finalement, je voudrais remercier tout particulièrement mes parents pour leur support exemplaire pour avoir cru en moi. Sans vous ou vos encouragements, rien de tout cela n'aurait été possible. Aussi, j'aimerais remercier pour leurs supports mon frère, les autres membres de ma famille et mes amis(es). Ceux qui ont été d'un grand support se reconnaitrons.

Je vous remercie tous encore une fois…

*Frédéric Charbonneau*

*To my parents and my family I dedicate this work.*

# Contents

# List of Figures

# List of Tables

# List of Equations

# List of Symbols

## Latin Symbols

| | |
|---|---|
| $A_{ij}$ | *Einstein Coefficient* |
| $E_{nm}$ | *Energy of the upper level* |
| $f$ | *Oscillator strength* |
| $g$ | *Statistic weight of the lower level* |
| $g_i$ | *Degeneracy of the upper level* |
| $h$ | *Tool-electrode length deep in the electrolyte* |
| $I^{crit}$ | *Critical current* |
| $I_{nm}$ | *Relative intensity of the sparks emission* |
| $\Delta I_{Hilevel}$; $\Delta I_{Lolevel}$ | *Current during High-level; Low-level* |
| $K_B$ | *Boltzmann constant* |
| $L$ | *characteristic length* |
| $n_e$ | *Electron density* |
| $r$ | *Polishing radius* |
| $R$ | *Machining radius* |
| $Re$ | *Reynold's number* |
| $r_{hole}$ | *Drilled hole radius* |
| $r_{tool}$ | *Tool-electrode radius* |
| $T_e$ | *Electrons temperature* |
| $1/\Delta t_b$ | *Mean detachment frequency of bubbles* |
| $\Delta t_f$ | *Gas film life time* |
| $\widetilde{U}$ | *Normalized voltage* |
| $U^{crit}$ | *Critical voltage* |
| $U_d$ | *Water electrolysis voltage* |
| $U^{lim}$ | *Limit voltage* |
| $\Delta V_{Hilevel}$; $\Delta V_{Hilevel}$ | *Voltage during High-level; Low-level* |
| $\Delta t_{Hilevel}$; $\Delta t_{Lolevel}$ | *Duration of High-level; Low-level* |
| $W_{tot}$ | *Total energy* |

## *Geek Symbols*

| | |
|---|---|
| $\rho$ | *Electrolyte density* |
| $v$ | *Electrolyte speed* |
| $\mu$ | *Electrolyte viscosity* |
| $\theta$ | *Tool-electrode bevel angle* |
| $\omega$ | *Tool-electrode rotation speed* |
| $\varepsilon_{ij}$ | *Transition energy* |
| $\lambda$ | *Wavelength* |
| $\Delta\lambda$ | *Stark broadening* |
| $\alpha_{1/2}$ | *Fractional semi-half-width* |

*Acronyms*

| | |
|---|---|
| *CAD* | *Computer-Aided Design* |
| *ECDM* | *Electro Chemical Discharge Machining* |
| *CNC* | *Computer Numerical Control* |
| *HAZ* | *Heat-Affected Zone* |
| *MEMS* | *MicroElectroMechanical systems* |
| *SACE* | *Sparks Assisted Chemical Engraving* |
| *TCL* | *Tool Command Language* |
| *TW-ECDM* | *Tool Wire Electro Chemical Discharge Machining* |
| *WEDG* | *Wire Electro-Discharge Grinding* |

*Dietro ogni problema c'è un'opportunità* Galileo Galilei

# 1 Introduction

In the last decade, new versatile fabrication techniques have been developed in various fields for a large range of applications. We can think about the new interest in 3D printing, the use of CNC machining or the extended use of laser machining in various applications. Those new fabrication methods have a common point: they are versatile and can fabricate complex objects or systems from a base material and a computer-aided design (CAD) drawing with a robotic system. Therefore, those techniques are highly desirable for quick custom fabrication of small production quantity or prototyping. This is at the opposite of the other more traditional fabrication process, which focus on mass productions and are more cost and time consuming to put in place.

Sparks-Assisted Chemical Engraving (SACE) is in the spirit of those new fabrication methods. SACE is an electrolytic based machining process which uses the etching propriety of $OH^-$ ions and the cathode effects to locally etch glass. With this technique, glass can be micromachined to form various structures only limited by the imagination of the user. The micromachining of glass is a key technology for microfluidic, optoelectronic, microelectromechanical systems (MEMS) and biomedical domains. Glass is used in those fields because of its unique properties such as its transparency, its biocompatibility and its thermal and mechanical properties.

## 1.1 Problem Statement

When an electrical potential is applied between two electrodes dipped inside a conductive liquid, there is gas accumulation at the surface of those two electrodes. This phenomenon is called electrolysis. If one of those electrodes is smaller in size than the other and a voltage higher than a critical voltage is applied between the two electrodes, the production of gas at the smaller electrode can build a compact gas film. This gas film insulates the electrode from the conductive liquid. This happened when the current density is higher or equal to 1 $A/mm^2$. To maintain the electro-chemical reaction, electrical

discharges (sparks) are emitted from the small electrode through the gas film. This phenomenon is known and has been studied since the 19th century. In our context, those electrical discharges can be used to locally provide the chemical species and heat needed to etch glass. Finally, if the smallest electrode is linked to a robotic head it is possible to move the electrode over a glass work-piece and machine complex structure on it. The biggest problem this technology faces off is the difficulty to control the gas film formation and the amount of thermal energy provide by the electrical discharges. This lack of control can make the machining speed and the machining quality hazardous, which is not desirable for an industrial application of the technology.

## 1.2 Motivation and Challenges

Posalux SA, a company evolving in the high-tech machine tool field, recently began the development of a commercial machine implementing the SACE process to etch glass. For this first commercialization of the SACE process, future customers' needs have to be taken into account: the cost of the machine, the process cost, the machining speed, the repeatability and the quality of the machining. Because the SACE process is adapted to customized products and R&D, machine cost is an issue, because it cannot depreciate on a large-scale production. For mass production, the machine cost is not an issue. Consequently, the machine design needs to be competitive.

Therefore, those customers' needs have to be investigated to improve the SACE technology for the market. The cost of the machine is determined by the company who works closely with customers to find a good compromise between cost and machine performances. Hence, three characteristics have to be improved by a R&D research group:

- *The machining speed*: to compete with other technologies which can etch glass (laser machining) the SACE machining speed has to be equal or higher than with laser machining. This allows quick machining suitable for customized production and prototyping.

- *The machining quality*: again, the machining quality has to be equal or higher than with laser machining. A machining process for R&D or customized production has to minimize the use of post-processing, because post-processing increases the effective machining time, adds complexity to the process and substantial cost.
- *The repeatability*: the final results have to be consistent and predictable to prevent the need to do empirical tests before every new machined structure.

To improve those three characteristics, an optimization of the machining parameters has to be done and a better understanding of the SACE process has to be developed. The optimum machining point is defined as the combination of machining parameters which allows a high machining speed (typically similar to the laser machining) and a good surface quality after machining. The machining parameters studied in this thesis are: property of the electrical signal, tool geometry, electrolyte type, electrolyte flow and machining strategy. Those parameters are already mentioned in the literature but need more investigation to be successfully used in an industrial application.

## 1.3 Contribution

Three different approaches have been used to optimize and explain the SACE process: the chemical approach, the thermo-hydrodynamic approach and the spectroscopic approach. The viability of those approaches in term of further optimization and uses for industrial application and SACE process understanding is discussed. The main contributions of this thesis are the following:

I. *Machining parameter determination and optimization to improve the machining quality*: the machining parameters investigated are the electrical input signal, tool electrode geometry, electrolyte type, electrolyte flow and machining strategy. This optimization has been done by semi-empirical analysis using visual observation of the machined zone.

II. *Explanation of the existence of this machining optimum point*: this explanation includes visual observation, I-t signal treatment and spectroscopic analysis of sparks emission.

III. *Development of a new machining strategy allowing a faster machining*: this machining strategy is based on a fast rough machining followed by a surface polishing at low voltage.

IV. *SACE application in real context*: use of SACE for two applications to prove the applicability of the SACE in an industrial context. Gorilla glass was machined to prove the versatility of SACE and glass-to-glass bonding after SACE micromachining was done for the same purpose.

One of the possible questions which can be raised up by this introduction is: why not benchmark the SACE process with other comparable technologies such Laser machining? First, when this work was made we do not have access to the other technologies. Secondly, some of those other technologies did not have all the flexibility of the SACE machining and they are not for the same niche application. Thirdly, benchmarking to other technologies such as the Laser machining does not follow the main goal of this work which is the improvement of the SACE process. The benchmarking is more important for a marketing perspective than a scientific perspective. With a benchmarking we do not focus on the understanding of the process.

# 2 SACE Fundamentals

This chapter provides an overview of the current understanding and knowledge of the SACE machining process. It is important to have a good appreciation of this work to fully understand the state-of-the-art SACE machining. Hence, in this chapter an overview of the different parameters affecting the SACE machining in terms of quality, speed and repeatability is provided. The importance of studying those parameters is revealed by the number of possible applications for the SACE technology: drilling holes, milling channels, cutting brittle materials [1], creating interconnections for micro-fluidic devices [2], 3D micro-machining, machining of a revolving glass rod [3], micro-texturing [4].

## 2.1 SACE Machining Process

Spark assisted chemical engraving was first introduced in 1968 under the name of electrochemical spark machining (ECSM). Since then constant research has been done to improve the control of the process. The basic idea comes from the application of an electro-chemical phenomenon called anode or cathode effect. This phenomenon occurs when two not dimensionally equivalent electrodes are placed in a conductive liquid (electrolyte) and an electrical potential is applied between them. Under some electrical conditions, the production of gas at the electrodes surface collapse on the smaller electrode (tool-electrode) and sparks occur in a gas film formed around it. In a highly conductive electrolyte, the gas film formation occurs at 20-30V. In SACE machining, the tool-electrode is usually 100 times smaller than the other electrode. Normally, the tool-electrode is the cathode. This choice of polarity is not benign. Reverse polarity on the other hand, has some drawbacks such as electrode erosion. When a dielectric material is placed in the vicinity of those sparks with proper chemical species inside the electrolyte, a chemical attack of the dielectric material occurs (Figure 1(a)) on the action of the sparks. A good way to describe how this mechanism works is to observe the stationary current-voltage (I-U) characteristic of the

system (Figure 1(b)). The stationary I-U curve of the SACE machining (Figure 1(b)) can be divided in five different regions. Each letter refers to (Figure 1(b)) [5]:

- *(0-A) Thermodynamic Region*: nothing important for us happens in this region. The electrolysis of water takes place only after $U_d$; for water $U_d$=2V.
- *(A-B) Ohmic Region*: electrolysis of water occurs in this region. The voltage increases at the same rate as the current. More current equals to more water dissociation. In other words, the quantity of gas created at the tool-electrode and the counter-electrode surface is proportional to the water electrolysis rate.
- *(B-C) Limiting Current Region*: the quantity of gas created at the tool-electrode surface creates bubbles and coalescence between each other and prevents further current to pass through the electrolyte; there is a stagnation of the reaction.
- *(C-D) Transition Region*: a gas film is created around the tool-electrode and isolates the tool-electrode from the electrolyte.
- *(D-E) Arc Region*: current transport occurs through the gas film via micro-arc discharges.

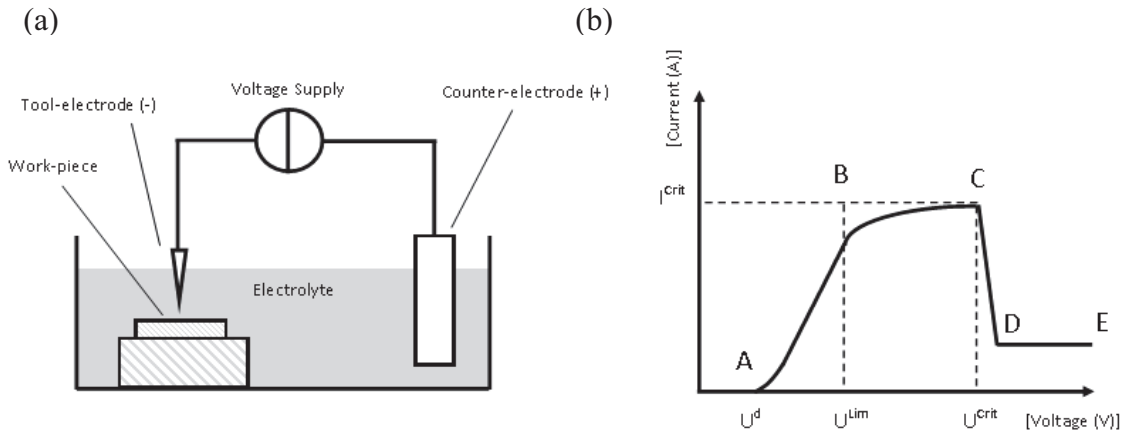


*Figure 1 : (a) schematic view of the SACE machining process (b) Stationary I-U characteristics of the gas film formation.*

The value of $U^{lim}$ and $U^{crit}$ from (Figure 1(b)) strongly depends on the electrolyte properties such as the type of electrolyte, the concentration, the viscosity and tool-electrode characteristics. A model has been developed to explain the gas film formation mechanism based on a stochastic model and the probability of two adjacent bubbles to collapse and stay on the tool-electrode surface [6].

To etch glass, $OH^-$ radicals are needed inside the electrolyte. Materials are removed from the work-piece by the action of $OH^-$ radicals present in the solution and those created by the electrolysis reaction helped by thermal energy from the spark. When the gas film is in contact with other materials, such as the work-piece, this process becomes more complicated. To this point, most publications about the SACE machining proprieties refer to the hole drilling or channel milling to judge the machining parameters efficiency in a situation closer to the application. Holes drilling is a particular case because, during SACE drilling the machining speed decrease in a reverse exponential way (Figure 2). This is reported and explained in [7]:

- *Discharge regime*: this happens in the first 200µm of drilling. In this region the machining speed can reach 100µm/s and is controlled by the number of discharges present in the gas film.
- *Hydrodynamic regime*: for depths higher than 200µm machining speed drops significantly, typically some few µm/s (Figure 2). The machining speed becomes limited by the ability of the electrolyte to reach the tip of the tool, because during the holes drilling, the gas film can obstruct the entire hole entrance and stop the machining observed and photographed by [8]. Also, the material removal rate is limited by the ability of heated materials to be remove from the bottom of the hole.

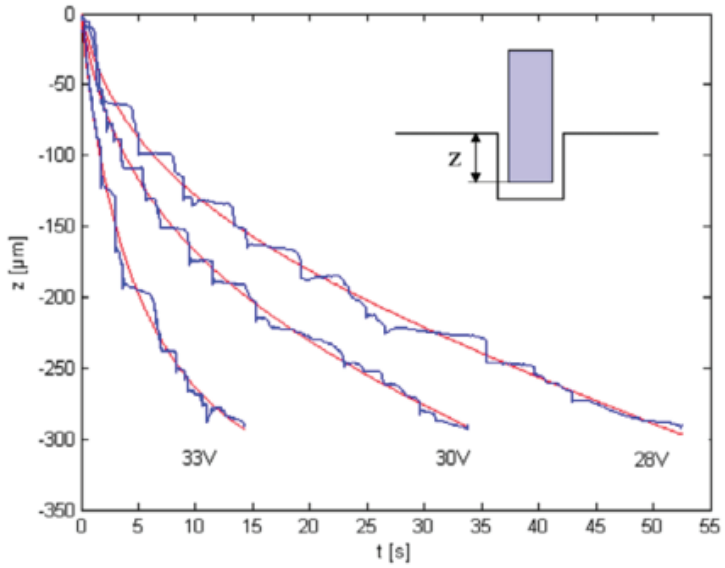


*Figure 2 : Typical drilling depth in function of the machining time for different DC voltage, use with the authorization of Journal of micromechanics and microengineering* [7].

## 2.2 Parameter Influencing the Process

The material removal process and the gas film dynamics is not yet fully understood. This is due to the complexity of the process. Two main hypotheses about the machining mechanism have been developed: thermal machining and chemical machining [9].

The thermal machining hypothesis assumes that the work-piece is intensively heated in the vicinity of the tool-electrode thus resulting in a melting or a vaporisation of the material work-piece in this region. The temperature in the gas film can reach around 500ºC. By comparing this value with the work-piece transition temperature which is around 550 ºC for soda-lime glass and around 1200ºC for fused quartz (two common work-piece material) the affirmation which said the SACE process is purely thermal doesn't seem to be right. However, it was shown experimentally in [10] that each discharge peaks locally increases the temperature of the work-piece above the melting temperature of the machined zone (at a micrometer scale). But on the other hand, they made an estimation which said 77-96% of the discharge energy is provided to the electrolyte and only 2-6% to the work-piece. Another experimental proof of the thermal machining hypothesis is the exponential increasing of the removal rate with the applied voltage.

The second hypothesis is the chemical etching characterized by Equation 1:

*Equation 1*

$$2NaOH + SiO_2 \rightarrow NaSiO_3(s) + H_2O$$

As mentioned in section 2.1, the $OH^-$ radical is well known for its capability to etch glass. The chemical etching of glass strongly depends on the electrolyte concentration of $OH^-$ radicals. Nevertheless, the SACE machining process is probably a combination of thermal and chemical etching, because the chemical etching increases significantly with the temperature. In addition to that, several parameters can influence the SACE and have been targeted over time in many publications. Figure 3 presents a wrap-up of the most common known parameters which influence the SACE machining. In the next subsections of this chapter, an explanation of the influence of those parameters is provided. Each subsection refers to a family of parameters intending SACE machining.

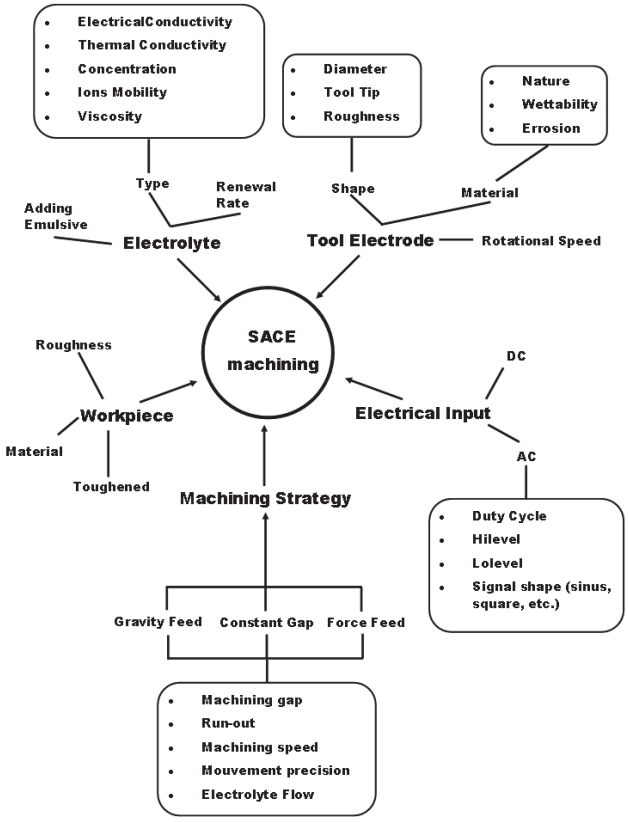


*Figure 3 : Schematic representation of the various parameters which influences the SACE machining process.*

Let's describe qualitatively the work-piece surface after SACE machining, before discussing the different parameters governing SACE. The impact of a set of parameters is often analyzed by visual appearance of the work-piece surface itself and by the presence of defects. The surface quality after SACE machining can be divided in different categories [11]:

- *Well-defined edges and smooth surface*: this is the desired machining, where every cut and drilling is perfectly defined and clean. There is no Heat-Affected Zone (HAZ), no micro-crack and has a minimal over-cut (Figure 4(a)). In the case of a drilling, there is a minimum of taper effect.
- *Smooth or unsmooth jagged outline contours*: jagged contours can affect the post-processing of SACE machining such as the sealing of a machined device (Figure 4(b)).
- *Heat-Affected Zone (HAZ) and micro cracks*: this usually happened at high input voltage (for DC input) and can significantly affect machined structures integrity and its features (Figure 4(c)).

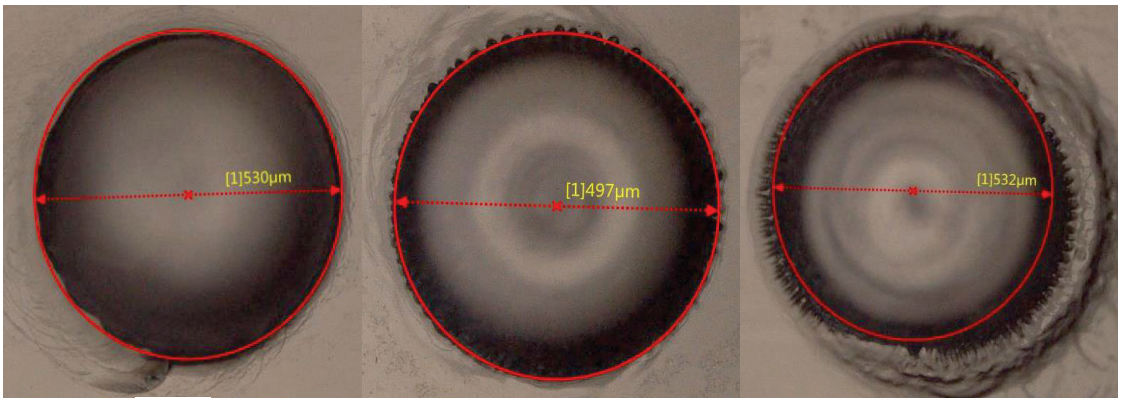


(a) (b) (c)

*Figure 4 : Examples of hole drilling quality after machining in a NaOH 30wt% electrolyte with a 250µm tool Ø spinning at 500 rpm for a pulse voltage: period=3ms; duty cycle= 50% (a) High-level=37V, Low-level=27V (b) High-level=31V, Low-level=22V (c) High-level=29V, Low-level=20V.*

### *2.2.1 Electrolyte*

As underlined in sections 2.1 and 2.2, the choice of the electrolyte is crucial in SACE machining. NaOH and KOH are the most commonly used electrolyte salts. They are relatively cheap and can provide a good amount of $OH^-$ radicals. Other electrolytes have been tested such as NaCl or $NaNO_3$, but they appear to be less effective. The material removal rate during machining is higher with NaOH and KOH than with NaCl, which can be attributed to the lack of $OH^-$ radicals in a NaCl solution. The type of electrolyte and its concentration changes the conductivity, the critical voltage, the ions mobility, the viscosity and the heat capacity of the electrolyte. These properties can have an influence on the gas film formation and its stability. .

Table 1 presents the evolution of I-U characteristic for different NaOH concentrations. Note the evolution of $U^{crit}$ in accordance to its concentration: this means the spark region can start at different voltage. A different $U^{crit}$ leads to a different input energy in the system, which has to be taken into account.

What is the relation between the machining speed and the electrolyte concentration? In [12], it was show that the machining speed increases with the concentration of the electrolyte. The authors present a series of experiences where holes entrance and holes exit in the case of through drilling varied with the electrolyte concentration. The latter has to be chosen carefully because this choice will affect the other machining parameters. Either way, to have a better machining speed or quality, we cannot just increase the electrolyte concentration. In particular, an increase of the electrolyte concentration generally includes a significant increase of the tool wear [13] and machining over-cut [14], [15].

Adding substances in the electrolyte can change positively its capability. In [5] the authors introduces a wetting agent in the electrolyte to change its performance (last row .

Table 1). In [5], the authors have highlighted the fact that mixing the electrolyte with a wetting agent (in this case soap) has a positive impact on the machining quality. With the same idea, another research group have clamed that surfactant such SDS can be added to the electrolyte to improve the machining quality [16]. But their results could not be reproduced in the frame of this study.

*Table 1 : Evolution of I-U propriety of different electrolytes in function of the concentration* [5].

| Electrolyte | $U^{crit}$ (V) | $I^{crit}$ (A) |
|---|---|---|
| **10wt% NaOH** | 29.0 | 0.55 |
| **20wt% NaOH** | 21.5 | 0.8 |
| **30wt% NaOH** | 21.1 | 1.30 |
| **40wt% NaOH** | 18.7 | 1.50 |
| **30wt% NaOH with soap** | 13.7 | 0.53 |

### *Electrolyte Flow*

The electrolyte motion and flow around the machining zone has an important impact on the machining quality and the machining speed. The influence of the electrolyte flow can be separated into two macroscopic characteristics: the electrolyte level and the electrolyte flow.

- *Electrolyte Level*: this is the height of electrolyte above the work-piece surface. If this level is too low, we will observe a local drying around the machining zone. Electrolyte dry out prevents machining. An example of the local drying effect is present in Figure 5, where after local drying, one can see materials deposition on the work-piece surface and poor machining quality. On the other hand, if this level is too high, the system will need more current to enter the spark region. This increase of current can be prohibitive to the process in terms of gas film stability and electrical system limitation.
- *Electrolyte Flow*: this is the general electrolyte circulation in the processing cell. This circulation has an impact on the gas film stability and the heat energy distribution.

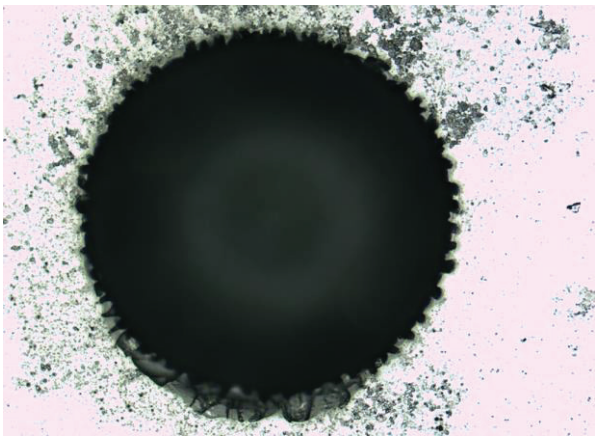

*Figure 5 : Hole drilling with material deposition during local drying near the machining zone: 30wt% NaOH, 40V DC, 500rpm.*

Later in this study in regards to electrolyte flow, we will make a distinction between two flows: the bulk flow and the microscopic flow (Figure 6). The bulk flow is the general flow in the processing cell generated by the pumping system. The microscopic flow is the electrolyte flow at the machining zone (at the vicinity of the tool-electrode), generated by the tool-electrode motion and the gas film dynamics. This flow is important during the hydrodynamic regime.

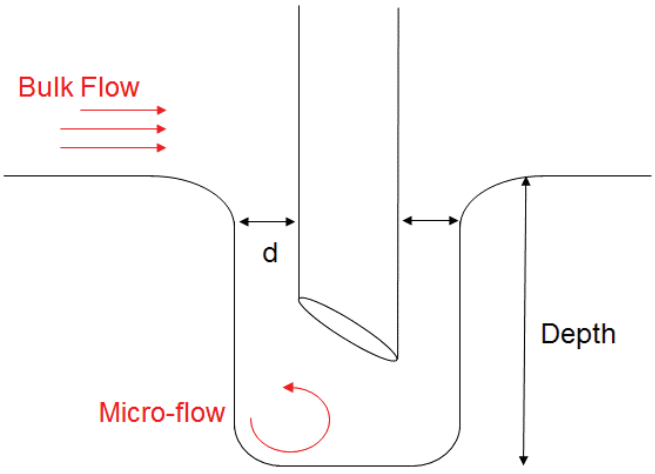


*Figure 6 : Schematic view of the two flows during hole drilling.*

### *2.2.2 Tool-Electrode*

The tool-electrode usually used in SACE machining is a metallic cylinder or a wire in the case of TW-ECDM. The most common materials used for the tool-electrode are tungsten carbide, stainless steel, copper and brass. The tool-electrode material impacts the critical voltage and the average current in the arc region. Tungsten carbide is predominantly used because of its high wear resistance, high stiffness and its low thermal expansion. The tool-electrode material expansion coefficient has an impact on SACE machining. In constant gap machining, the tool-electrode position must be adjusted according to the thermal expansion [17] and in gravity feed machining, the force on the tool-electrode can significantly increase with the thermal expansion. According to [17], the tool wear rate during SACE machining is around 0.5 μm/s for tungsten carbide electrodes at 32V DC in NaOH 30wt%. This rate can change with the electrolyte concentration and the voltage input level. However, the current signal with tungsten carbide tool-electrode is less stable, resulting in non-uniform machining and HAZ [18].The surface roughness of the tool-electrode has an impact on the gas film properties [18]. The gas film thickness depends on the tool-electrode roughness (Figure 7(b)). Rougher the tool-electrode, wider is the gas film. [6] and [19] developed a gas film formation model based on percolation theory which depends on nucleation sites related to the tool-electrode roughness (Figure 7(a-b)). The surface roughness can also be in relation to the tool-electrode wettability. For example, a tool-electrode with poor wettability has more affinity to the gas, which results in an easier gas film formation.

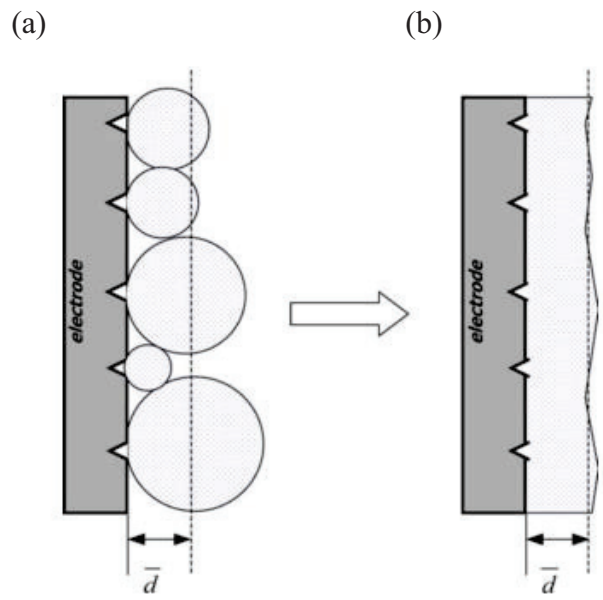


*Figure 7 : (a) growing of gas bubbles from nucleation sites and (b) formation of the gas film after coalescence, the value $\bar{d}$ refers to the mean gas film thickness, use with the authorization of International Journal of Machine Tools & Manufacture* [5].

Another property of the tool-electrode influencing the machining is its geometry. According to [20], the tool tip has an influence on the material removal rate and the over-cut. They compared a cylindrical tool-electrode with a flat taper tool-electrode and a taper tool-electrode with a spherical tip. They pointed out the fact that the material removal rate is significantly less with a cylindrical tool-electrode than with a taper tool-electrode or a tool-electrode with a spherical tip. Also, the machining over-cut is higher with the cylindrical tool-electrode than with a taper tool or a spherical tip tool-electrode. They claim that tool-electrode spherical tip increases the amount of electrolyte available at the machining zone. This is also reported by [21].

In [22] the authors test the effect of two other tool-electrode geometries: a cylindrical tool-electrode and a flat sidewall-flat front tool-electrode (Figure 8). The flat sidewall-flat front tool-electrode significantly decreases the over-cut and the taper effect in the case of hole drilling. They claim the flat side decreases the influence of the discharge to the inert wall side. More the tool-electrode is flattered, less taper effect is present. However, the machining speed decreases. The decrease of the machining speed can be caused by the large amount of energy consumed to heat the excess of electrolytes near the

machining zone [22]. Another explanation for the reduction of the machining speed in correlation to hole diameter reduction is related to the quantity of electrolytes which can reach the hole bottom.

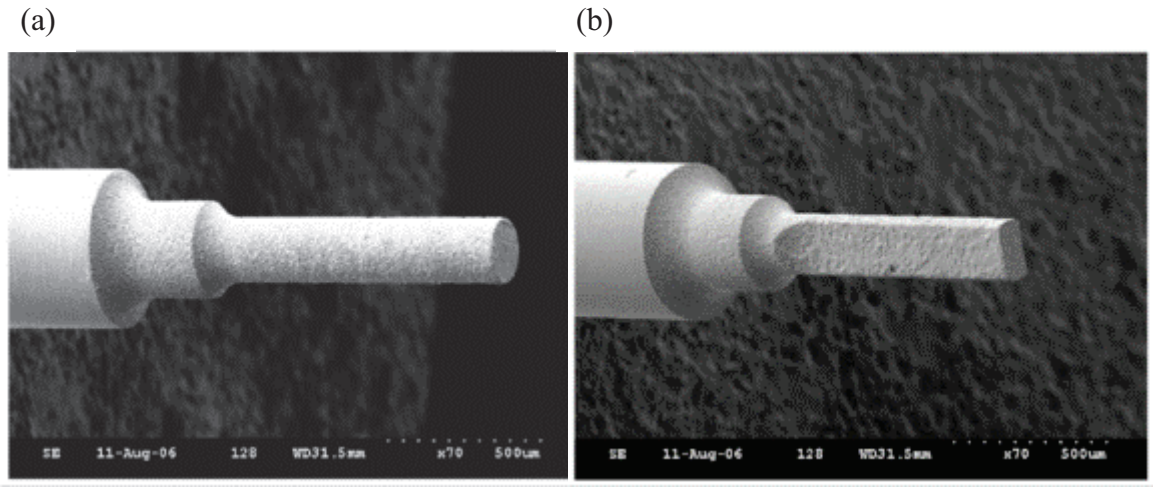


*Figure 8 : Different geometry shape (a) cylindrical tool-electrode (b) flat sidewall-flat front tool, use with the authorization of International Journal of Advanced Manufacturing Technology* [22].

Other techniques have been used to improve the material removal rate or the machining quality such as vibrating tool-electrode [23] and tool-electrode spinning. The most significant effect of a vibrating tool occurs during deep drilling (hydrodynamic regime). According to [22], the tool-electrode spinning has an impact on the HAZ. HAZ during hole drilling reach a minimum around 1500 rpm for: 40V rectangular pulse $T_{on}$: $T_{off}$=2ms:1ms in 5M KOH.

### *2.2.3 Work-Piece*

The work-piece material has an impact on the selected machining input parameters. The most common materials used in SACE is Soda-lime glass, Borosilicate glass, Quartz [24] and Silica. In fact every material with $SiO_2$ links can be machined. Also, it is possible to machine ceramics [14],[20], [15] or glass-fiber-epoxy composite [25]. The choice of the work-piece depends on the application field. Thus, for a fixed work-piece material other parameters are required to explain variation of properties of the work-piece [26].

### *2.2.4 Electrical Input*

The electrical input signal has a significant impact on the machining quality and speed. The average time to build a gas film is related to the applied voltage [5], [27]. A higher voltage corresponds to a higher machining speed [14]. However, as reported in several publications, high voltage machining results in the formation of thermal cracks and HAZ. Several research group observed that a large over-cut and the formation of an entrance taper angle is unavoidable when a DC voltage is used [28]. The over-cut depends on the voltage level. Another approach was developed to use rectangular pulse voltage signals with an offset was developed to overcome this problem. The use of a pulse voltage input without an offset increase significantly the complexity of the problem. But at the same time, the machined work-piece has a better quality. [28] presents the results of using a pulsed voltage for the reduction of the over-cut during machining. They attribute this to the reduction of the average thermal heating because during pulse-off time there is no spark (also highlighted by [22]). It appears that the use of rectangular voltage pulses can reduce the HAZ [29]. A drawback of this methods is the fact that the material removal rate decreases when the pulse voltage frequency increases and the duty cycle decrease. This can also be explained by the reduction of the local thermal energy. According to [29], the effect of the duty cycle becomes negligible when the tool diameter is large (500-700µm). [30] have shown the drawback of using pulse voltage without offset: the pulse voltage machining without offset increases the standard deviation in SACE machining. The use of a pulse voltage can thus affect the repeatability of machining. They explain this mostly by the increase of the machining time (i.e. lower material removal rate). Another possible explanation of this is the fact that electrolysis is not continuous when a pulse voltage is applied. In such cases, it becomes difficult to build a gas film and this makes the discharges unstable [27]. However, to reduce the SACE machining standard deviation and increase the machining speed a pulse voltage with an offset can be used [30].

***Machining Methods***

Using a machining method over another can affect the machining rate and the machining quality. Commonly there are four machining methods used for SACE (Gravity feed, constant velocity feed, constant gap machining and closed loop machining). [31], [32] provide a good overview of those machining methods with their pros and cons. Here are the three main machining methods:

- *Gravity feed*: this is the most common drilling method used. A constant force is applied between the tool-electrode and the work-piece. The advantage of this method is the possibility to directly monitor the drilling or the machining progress. This method is not desirable for small tool-electrode because of a possible tool-electrode break during machining. As highlighted by [31], this method is not desirable for machining deeper than 200µm. Passed this depth, the machining speed decreases significantly.
- *Constant velocity feed*: a constant motion of the tool-electrode in the machining direction is applied. To be certain there is no contact between the work-piece and the tool-electrode, the speed must be under the average material removal rate. If the speed is higher, this can lead to a breaking of the tool-electrode. This speed strongly depends on the applied voltage, on the tool-electrode diameter and in the case of drilling the depth. [33] suggest there is an upper limit for the feed rate around 10-30µm/s with a cylindrical tool-electrode of 600µm diameter. But again, this value depends on several factors such as the voltage level, the type and the concentration of the electrolyte. The distance between the tool-electrode and the work-piece during machining cannot be measured.
- *Constant gap machining*: a constant gap is maintained between the tool-electrode and the work-piece. This method comes from travel wire electro discharge machining (TW-ECDM) and was adapted to SACE machining. The benefits of this method is the constant fresh electrolyte circulation around the machining tool-electrode. The main problem with this method is how to measure the gap and maintain it during machining. To be able to maintain a constant gap, the work-piece

surface position has to be precisely determined on all expected regions before the machining itself. Also, the tool-electrode gap has to be constantly adjusted during machining because of the thermal expansion.

As described in the results section, the machining quality is also dependent on the run-out of the tool-electrode. In fact, any rotating system has a run-out and this run-out can be an obstacle during machining.

# 3 Machining Set-up and Experimental Methods

In this section, technical information about the two SACE set-ups used for this study is provided. Two set-up have been used alternatively in for this study. One of the set-up is located in the Electrochemical Green Engineering group in Concordia University, Montreal. The other set-up is located in Posalux SA, Switzerland. The Posalux SA set-up is the first commercial prototype for the micromachining market as mentioned in section 1. It is important to understand the capabilities of those set-ups to fully appreciate the results of this study. The improvement and optimization of the mechanical part of the SACE machine of Concordia University and by extension the Posalux SA set-up was fully reported by [32]. Also, because most of the SACE tests conducted for this study are holes drilling, the drilling method used is explained in this chapter.

## 3.1 Laboratory Set-up (Concordia University)

In this section, the mechanical and electrical properties of the Concordia University set-up is presented (Figure 9). The set-up described in this section is similar to a set-up previously used by [32]. This set-up has the capacity to precisely move the tool-electrode on the work-piece by using a cartesian robots. All the tool-electrode motion is assisted and controlled by a computer interface. The upcoming sections present in more details the set-up component. The working system (machine-head and processing cell) is surrounded by a ventilation system to prevent any contamination of the working environment by toxic and dangerous vapor. The vapor emanation from the SACE are: $H_2O$, $O_2$, $H_2$, $K^+$, $Na^+$, $OH^-$ and other machining sub-products.

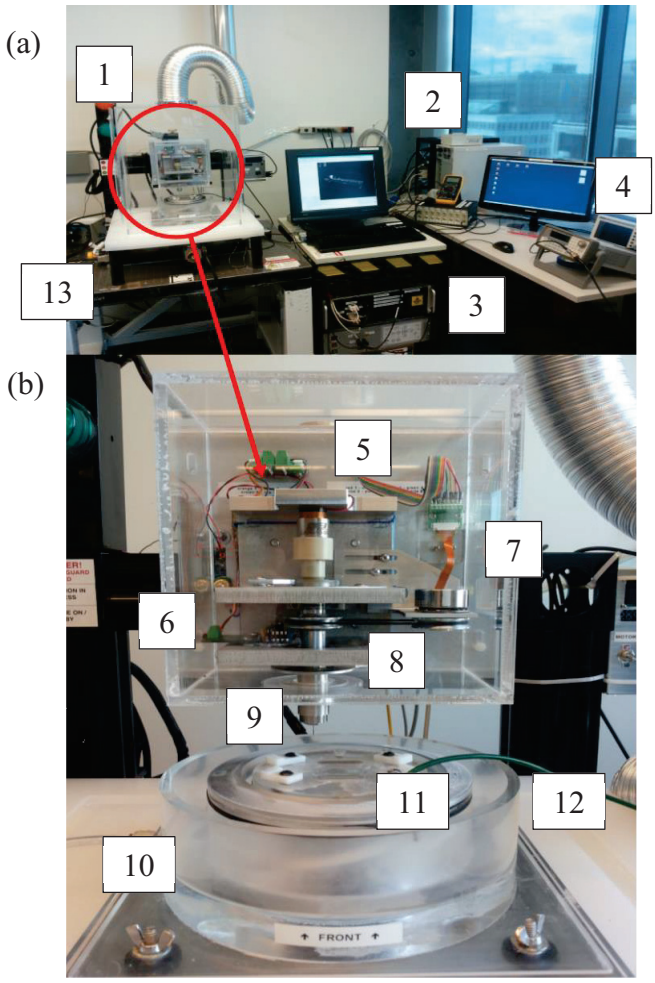


1. Machine-head
2. Computer Control
3. Amplifier
4. Function generator
5. Voice coil
6. Optical sensor
7. Spindle motor
8. Flexible structure
9. Tool electrode
10. Processing cell
11. Work-piece holder
12. Counter electrode
13. Electrolyte pump

*Figure 9 : (a) SACE machining facility including the control computer, the circuit and the aeration system. (b) the SACE machine-head and the processing cell close-up. The machine-head with is optical sensor, voice coil, spindle motor and tool electrode is mounted on a Z axis and a flexible structure. The processing cell contain the counter electrode and the work-piece holder. The electrolyte level above the work-piece is maintain by an overflow. An outside cylinder container collect the overflow of electrolyte.*

### *3.1.1 Mechanical System*

The set-up is mounted on a XYZ-stage (Cartesian robot) from Newport. The machine-head is mounted on the Z axis (M-ILS50CC) and the processing cell is mounted on a XY-stage (M-ILS150CC). Each of those three axes has a precision around 1µm. The tool-electrode is held in the machine-head by a spindle-collet which is maintained by a precise fitting. Different spindle-collet can be placed on the tool shaft to accommodate different tool-electrode diameters. The tool-electrode shaft is maintained in place by two bearings connected to two flexible structures (Figure 10). Those flexible structures allow

the tool shaft to move freely with a low stiffness and damping in the Z direction but restrain the motion in X and Y directions. This allows precise determination of the force apply to the tool-electrode and precise motion on the work-piece. The flexible structure is equipped with stoppers to prevent any machine-head crash. The tool shaft is also free to rotate on its axis. The tool-electrode shaft rotation is controlled by an electrical motor connected via a rubber belt. This motor allows a spinning range from 300 to 3000 rpm.

The machine-head also incorporates an optical sensor (SFH9201 from OSRAM Opto Semiconductors) and a voice coil actuator (LA-08-10-000 from BEI Kinco Magnetics). The optical sensor and the voice coil are used to control the tool-electrode axial position  This allows us to use the machine-head as a profile-meter to detect the surface of the work-piece.

*Figure 10 : Picture of the flexible structure which allow the machining heat to move freely in the Z direction and constrained the motion in the X and Y axis.*

### *3.1.2 Controller and Data interface*

The control of the set-up is implemented on a dSPACE and a XPS controller (Figure 11). Also, a servo drive controls the voice coil and a second one the rotational speed of the spindle. The motion of the XYZ-stage, the voice coil and the spindle is controlled by programming TCL scripts which are uploaded to the Newport controller.

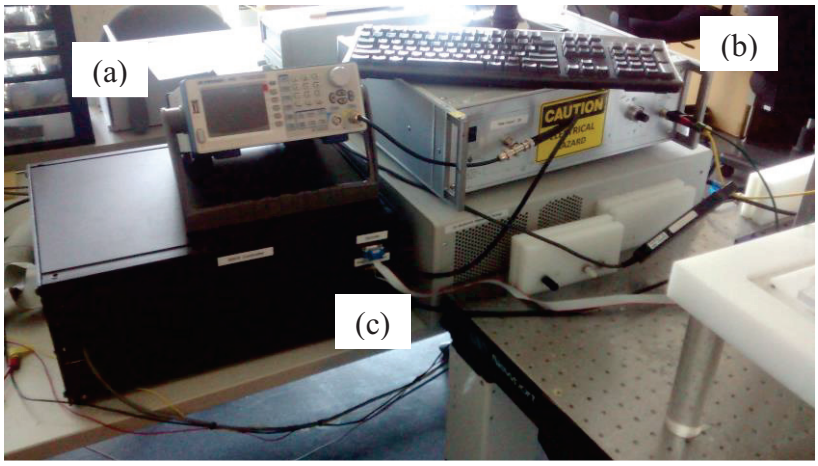


*Figure 11 : Picture of the controller system and the electrical circuit (a) function generator (b) amplifier (c) XPS controller*

### *3.1.3 Electrical System*

The signal input is generated by a function generator (Agilent 33220A 200 MHz function/arbitrary waveform generator). The function generator allows us to test the influence of different electrical input to the SACE machining. This function generator can be used to generate DC voltage or a pulse signal, sinusoidal signal, rectangular signal, triangular signal, etc. The operating range is between 1µHz and 20MHz in frequency and ±10V output voltage. The output of the function generator is controlled by the controller (section 3.1.2). The signal of the function generator is amplified by a homemade amplifier before passing through the system. This amplifier is limited to 2A and 38V.

### *3.1.4 Processing Cell*

The processing cell contains the counter electrode, the electrolyte and the work-piece holder. All the processing cell is made of acrylic. This material was chosen because of it's corrosion resistance and affordability. The processing cell is composed of two concentric cylinders (Figure 9(b)). Inside the inner cylinder there is the counter electrode and the work-piece holders. The counter electrode (anode) is a stainless steel A151-318 sheet fixed inside to the periphery of the inner cylinder's wall. This counter electrode is connected to the electrical system by an electrical wire. Electrolyte filled the inner cylinder and the electrolyte level is controlled by an overflow system. To make sure there is no

contamination of the electrolyte, no other material than acrylic and stainless steel is in contact with the electrolyte through the electrolyte cell.

The two cylinders are connected by an electrolyte circulation system and a pump (Masterflex model 77200-12). This pump is computer drive and can provide a flow rate from 2.1 to 560mL/min. A tube placed at the bottom of the external cylinder collects the electrolyte, under the action of the pump and continually fills the inner cylinder by the bottom. This electrolyte circulation prevents local dry out of the workpiece and heat accumulation at the machining zone. The injection of fresh electrolyte by the bottom helps to have a constant and stable flow in the machining zone. The stability of the electrolyte flow is important for the repeatability of the machining.

## 3.2 Posalux SA Set-up (Prototype of commercial Machine)

It is not possible to fully present the specific technical propriety of this machine because a substantial part of its innovative system is protected for intellectual property. However, we can present the technical capability which are used to sell the machine. This machine is controlled by g-code and a LabVIEW interface, which is processed by a Siemens IPC 477D Win AC RTX controller. An XYZ-stage is used to control and move the tool electrode. All the machine is in a personal protection box which contain a ventilation system connected to an air filter and an electrolyte circulation system (Figure 12). The machining head of this set-up is in contrary to the other set-up not connected to a flexible structure but all the machining head is placed under air pressure. The spindle is designed such that the tool-electrode has virtually no run-out. As we will see, the hydrodynamic around the tool-electrode has a significant impact on the quality and the machining speed. Therefore, the run-out can induce random electrolyte motion around the tool-electrode and affect the machining. The commercial machine can, as the laboratory setup, be used as profile meter in order to detect the glass surface. Finally, the processing cell incorporates an electrolyte nozzle. This electrolyte nozzle allows the user to have a directional bulk flow in the processing cell.

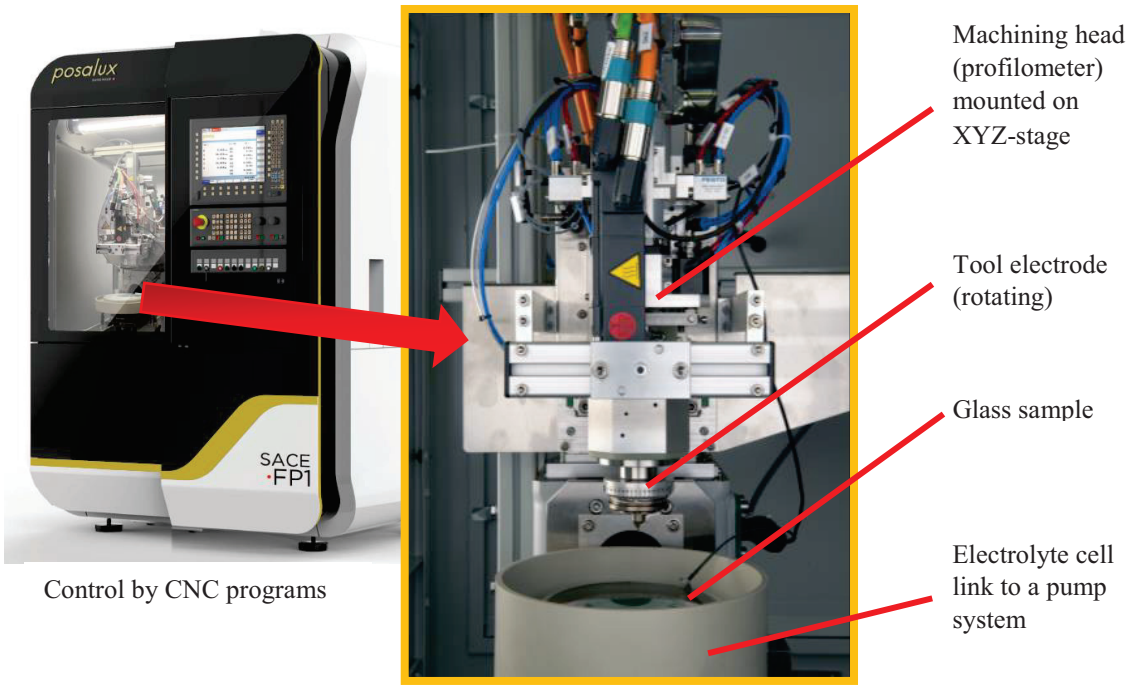


*Figure 12 : Picture of the Posalux SA commercial SACE machine with a quick description of the machining head.*

## 3.3 Holes drilling Method

The drilling method used for this study is explaining step by step in this section. This method is a combination of velocity feed drilling and gravity feed drilling.

I. The surface is detected using the optical sensor capability of the tool-electrode shaft. As presented in (section 3.1.1), when the tool electrode touches the work-piece, the flexible structure which maintains the tool-electrode shaft bend and this bending is detected by an optical sensor (Figure 13(a)).

II. The tool-electrode is moved 100µm above the work-piece surface to start the rotation and the machining voltage (Figure 13(b)). This step was added because when the tool tips touches the work-piece surface while rotating (especially at high tools tip angles), the tool has a tendency to move randomly on the work-piece surface. This random motion is prohibitive to the machining quality and the machining position, such as when we drill a slippery surface with a drill press (Figure 14).

III. The voltage and the spindle is applied and the tool head is slowly put in contact with the work-piece (Figure 13(c)). The 300µm depth is machined in 8 steps. At the beginning of each step the tool-electrode is put in contact with the work-piece surface and the tool-electrode head is moved forward by 37.5µm for a 300 µm depth hole (Figure 13(d)). Those value of 8 steps and 37.5µm was chosen after some preliminary empirical tests. This motion is absorbed by the flexible structure and the optical sensor signal drops. The drilling occurs and when the optical sensor level returns to its initial position and another step is applied until the depth of 300µm is reached.

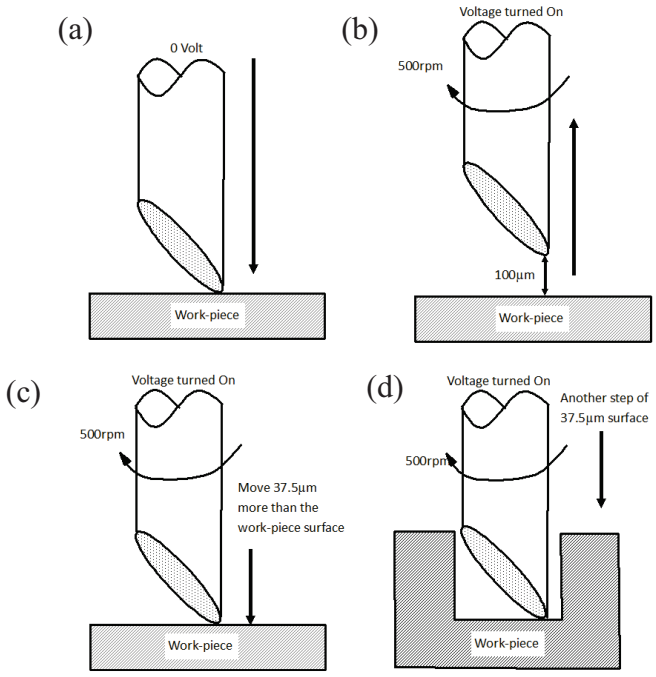


*Figure 13 : (a) work-piece surface detection (b) tool-electrode move 100µm above the work-piece surface and spindle/voltage turn on (c) the tool-electrode is slowly put in contact with the work-piece and an additional motion of 37.5µm is apply (d) when the optical sensor signal return to is initial position another step is apply.*

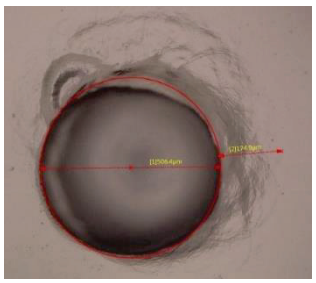

*Figure 14 : Picture of a hole drilling without the step (b).*

## 3.4 I-t Analysis Set-up

To investigate the current as a function of time (I-t), an auxiliary electrochemical cell is used (Figure 15). Two electrodes submerged in a glass cell are connected to a power amplifier (same as used in section 3.1) driven by a function generator (Agilent 33220A 200 MHz function/arbitrary waveform generator). The input voltage from the function generator and the I-t signal is observed using an oscilloscope and an Agilent current probe model N2774A—50MHz. The signal is acquired using a Matlab script which communicates with the oscilloscope. With the scope we cannot take a long time interval of the signal. Because of that, we have to take multiple time intervals to have significant results. The electrolytic cell is equipped with a water-cooling system to keep the temperature constant during the test (23 ºC), since the current in the cell generates signifcant heat when a voltage is applied between the two electrodes. This cooling system allows to remove the temperature variation from the parameters. The tool-electrode is placed on a micrometer stage to adjust the length of the electrode depth in the electrolyte. For all tests, the tool-electrode dipping length inside the solution is 2mm. A circular counter electrode of 6cm inner diameter and 2cm height made out of a stainless steel surounds the tool-electrode. The relative position between the tool-electrode and the counter electrode is kept constant between each test because this distance can influence the results.

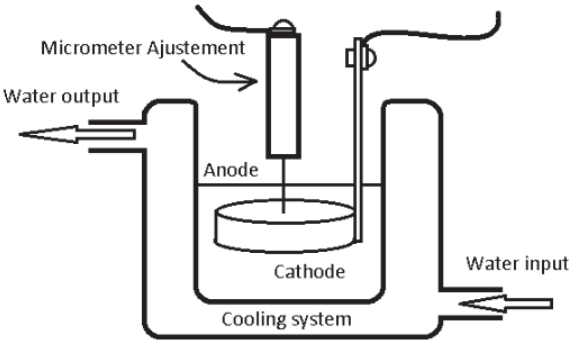


*Figure 15 : Schematic view of the electrolytic cell. The electrolytic cell is surrounded by a water cooling system. A constant water flow enter by the bottom of the cell and exit at the top. The catalytic reaction is fully isolated from the cooling system by a wall.*

# PART I : Electrolyte Approah

# 4 Electrolyte Optimization

The electrolyte is one of the most important components in the SACE process. In particular, the constituent ions ensue charge circulation (current) for the electrolytic process and the gas production. Also, the electrolyte provides the etching species needed to machine glass. The optimization of the electrolyte can provide faster machining and better quality. In this chapter, we will see that a KOH based electrolyte should be prioritized over a NaOH based electrolyte with comparable concentrations. SACE machining with KOH based electrolyte is much faster and provides better surface quality than with NaOH based electrolytes. This result can be explained by the low viscosity of KOH based electrolyte compared to a NaOH based electrolyte. In addition to that, an investigation of usage of surfactants (wetting agent) in SACE is provided.

First of all, let us introduce electrolyte intrinsic properties which influence the SACE process. Those characteristics can be divided in four categories: electrolyte nature, electrical conductivity, electrolyte thermal conductivity and the electrolyte gas film dynamics (the gas film stability does not depend only on the electrical parameters but also on the environment around the tool-electrode).

- *Electrolyte Nature*: as presented in (section 0), the two main electrolyte salts used in SACE are NaOH and KOH. These are chosen because of their low cost and their high $OH^-$ ion concentration in aqueous form. As said, $OH^-$ is the chemical etching species for glass. Because of that, the focus of this chapter is put on those two salts (NaOH and KOH).
- *Electrolyte Electrical Conductivity*: the electrical conductivity depends on the electrolyte concentration and on the ions mobility inside it. The electrical conductivity increases with the concentration until the concentration reaches a maximum value. After this point, the conductivity decreases with the concentration. The existence of a maximum value comes from the increase of ions recombination and the decreases of ions mobility inside the electrolyte at high concentrations.

Typically, for NaOH based electrolyte, the maximum concentration before the electrolyte conductivity decreasing is 30wt% whereas for KOH based electrolyte the maximum is above 50wt%. These values are valid at 50ºC. This concentration evolves proportionally with the temperature.

- *Electrolyte thermal conductivity*: the thermal conductivity of the electrolyte has an impact on the temperature near the machining zone. The electrolyte heat evacuation capability can have an influence on the machining speed and the machining quality. If less heat is evacuated from the machining zone, the machining quality will decrease while HAZ and defects (e.g. micro-cracks) appearance will increase. On the other hand, if all the heat is evacuated from the machining zone, the machining speed will decrease significantly. Besides that, the thermal conductivity in the case of SACE is strongly related to the electrolyte circulation and its viscosity.
- *Gas film stability*: the gas film building and collapsing is intimately linked to the contact angle between the electrolyte and the tool-electrode. The affinity between the tool-electrode and the electrolyte can facilitate the formation of the gas film. If the contact angle between the tool-electrode is greater than 90º (Figure 16(a)), the gas film formation is in theory easier (low wettability) because a part of the job is done. On the other hand, if the contact angle between the tool-electrode is smaller than 90º (Figure 16(b)), the gas film formation is more difficult (high wettability). This contact angle can be change by adding surfactant in the electrolyte.

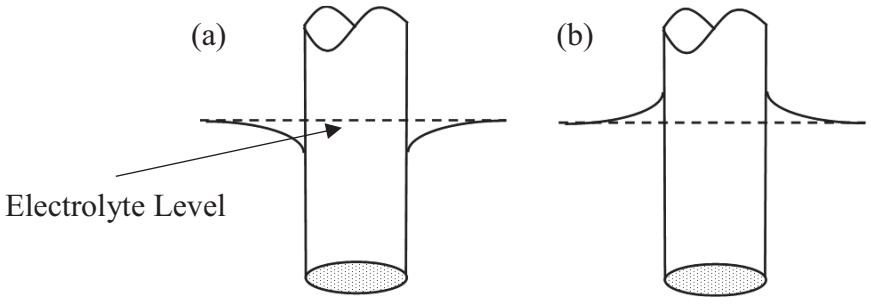


*Figure 16 : Schematic view of the contact angle between a tool-electrode and the electrolyte (a) contact angle greater than 90º between the tool-electrode material and the electrolyte (b) contact angle smaller than 90º between the tool-electrode material and the electrolyte.*

## 4.1 Electrolyte Concentration Effect

The electrolyte optimization passes by its concentration. The electrolyte concentration determines the electrolyte electrical conductivity and it viscosity. Those two characteristics (electrical conductivity and viscosity) have an important influence on the gas film dynamics and the SACE machining itself. If the electrical conductivity is too low, a higher input voltage will be needed to have a gas film formation and spark discharges. A higher input voltage corresponds to an increases of the temperature at the machining zone and more HAZ. Consequently, the conductivity must high to be able to machine at low voltage. The viscosity influences not only the gas film dynamics but also the two electrolyte flows (section 0). A more viscous electrolyte will reduce the motion around the machining zone, particularly during drilling where the machining speed is strongly dependent on the microscopic flow. A high conductivity and a low viscosity is required.

Therefore, a more subsequent analysis of the electrical conductivity evolution as a function of the electrolyte concentration is needed (for the two main electrolyte salts). At concentration lower than 30wt% NaOH for a temperature of 50ºC, the conductivity of the electrolyte increases with the concentration, as presented before. After this value, the conductivity decreases[1] with the concentration because of the ionic recombination inside the solution [34]. This can be expressed by an empirical formula [35]. Therefore, for SACE a concentration over 30wt% NaOH only increases the viscosity of the solution but does not improve the electrical characteristic of the electrolyte. This value is around 50wt% for the KOH at 50ºC and around 30wt% at 15 ºC [36]. Consequently, this study focus on electrolyte concentrations under those two values. If we neglect the ionic recombination inside the electrolyte the $OH^-$ concentration is proportional to the concentration of Salt (Figure 17). Therefore, to have the same conductivity with KOH as with NaOH, the concentration in wt% has to be higher because of the higher molecular weight of KOH. Also because a KOH based electrolyte is significantly less viscous, we can increase its concentration without significantly influencing the electrolyte motion. Therefore, the goal

[1] Occidental Chemical Corporation (OxyChem), Basic Chemicals Group, Occidental Tower, 5005 LBJ Freeway, Dallas, TX 75244

is to find a trade-off between the addition of $OH^-$ radical, the electrical conductivity and the viscosity of the electrolyte.

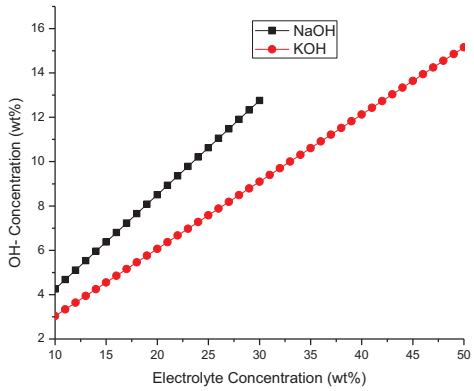


*Figure 17 : Evolution of the OH- concentration inside the electrolyte for the two main electrolyte salt (without ionic recombination)*

### *4.1.1 Machining Tests*

To test the influence of the electrolyte concentration on the machining speed and the machining quality, we used the same experimental method presented in section 3.3. 50 holes of 300µm deep were drilled with a cylindrical tool-electrode with a 60º bevel (chapter 6.1). Those tests were made with the set-up presented in section 3.1. The tool-electrode had a diameter of 500µm. The electrical input signal was 34V high-level, 17.5V low-level with a 2.5ms period along a 0.1ms off-time. The tool-electrode had a 500rpm rotation speed. Four different electrolytes were tested: 20wt% NaOH, 30wt% NaOH, 26wt% KOH and 50wt% KOH. Note that the 20wt% NaOH and 26wt% KOH have roughly the same concentration of cation and the same conclusion holds for the 30wt% NaOH and 50wt% KOH. This section shows the influence of the electrolyte concentration by discussing the drilling time and the drilling quality.

Because the tool-electrode has a large diameter the machining time is much higher when we use the 20wt% NaOH (921±130 seconds over 10 holes drilling). Because of this very high machining time, this electrolyte concentration was disqualified from the analysis. Table 2 shows the average machining time for the three other electrolytes. Notice that the

machining time presented in Table 2 includes the motion of the tool electrode and the machining themselves. The motion of the tool-electrode is the same for every holes. We clearly see as the electrolyte concentration is increasing, the machining time decreases. The machining time decreases by a factor of 3 when we double the concentration of the electrolyte in the case of the KOH and by a factor of 9 when we double the NaOH concentration. The decreasing of the drilling time with the increases of the electrolyte concentration probably comes from the increasing of the conductivity and etch agents concentration associated with it.

*Table 2 : Average drilling time of a 300$\mu$m deep hole for different electrolytes with a tool-electrode diameter of 100$\mu$m.*

| Electrolyte | 26wt% KOH | 50wt% KOH | 20wt% NaOH | 30wt% NaOH |
|---|---|---|---|---|
| **Average machining time** | 37±13 seconds | 12±5 seconds | 921±130 seconds | 100±17 seconds |

It is concluded that the electrolyte based on KOH salt is better in terms of machining speed. This comes from the fact KOH is less viscous than NaOH (Table 3) and has a better circulation around the machining zone. Because of this the electrolyte is more prone to reach the hole bottom during drilling.

*Table 3 : Electrolyte viscosity in relation to the concentration (wt%) and the temperature. This data comes from OxyChem Caustic Potash and Caustic Soda Handbook[2].*

| Electrolyte Concentration | Viscosity at 20°C | | Viscosity at 50 °C | |
|---|---|---|---|---|
| | NaOH Viscosity (cP) | KOH Viscosity (cP) | NaOH Viscosity (cP) | KOH Viscosity (cP) |
| **10wt%** | 1.75 | 1.24 | 0.95 | 0.40 |
| **20wt%** | 4.40 | 1.60 | 1.95 | 0.93 |
| **30wt%** | 15 | 2.30 | 4.25 | 1.30 |
| **40wt%** | 40 | 3.40 | 8.50 | 1.8 |
| **50wt%** | - | 5 | 17 | 2.75 |

Let us now discuss the quality of machining. Three measures were used to analyze the influence of the electrolyte concentration and its type on the machining quality: the average hole entrance diameter, the HAZ extension and a general visual observation of the

[2] Occidental Chemical Corporation (OxyChem), Basic Chemicals Group, Occidental Tower, 5005 LBJ Freeway, Dallas, TX 75244

holes after the machining. The HAZ extension is the maximal distance between the perfectly circular hole entrance and the further HAZ. This information was determined from microscopic pictures using data performing software (Keyence VHX-5000). Table 4 displays the evolution of the holes entrance diameter and the HAZ extension with the electrolyte concentration.

*Table 4 : Average holes entrance diameter and the average HAZ extension for different electrolyte concentrations and two different salts (tool-electrode diameter of 100μm).*

| **Electrolyte** | **26wt% KOH** | **50wt% KOH** | **30wt% NaOH** |
|---|---|---|---|
| **Average Hole entrance Diameter** | 851±18μm | 679±21μm | 771±37μm |
| **Average HAZ extension** | 35±15μm | 39±13μm | 43±8μm |

As presented, the average hole entrance diameter depends on the machining time (Table 2 and Table 4). An increasing of the machining time of about 60% corresponds to a 20% increase of the hole entrance diameter (KOH result from Table 2 and Table 4). This comes from the fact that more time the tool-electrode passes on a specific place on the work-piece, the more affected the work-piece will be (increasing the radial etch surface). Therefore, the more time the tool-electrode will pass inside a hole the more its edge will be flared. This effect is less important with electrolyte based on NaOH salt.

The HAZ extension does not vary a lot between the three electrolytes used (Table 4). Therefore, we can conclude that there is always a minimum HAZ extension for a specific set of electrical input. However, the NaOH has a relatively larger HAZ extension than KOH, but with less variation in results (more repeatability with NaOH). Moreover, a direct visual observation of the hole entrance can give an idea of the electrolyte viscosity impact. Figure 18 show the general look of the hole entrance for the different electrolytes. The machining quality seems to decrease with the increasing of the viscosity. A viscous electrolyte generates jagged outline contours on the contrary a less viscous electrolyte does not. The jagged outline contour seems to be generated by a non-uniform microscopic flux.

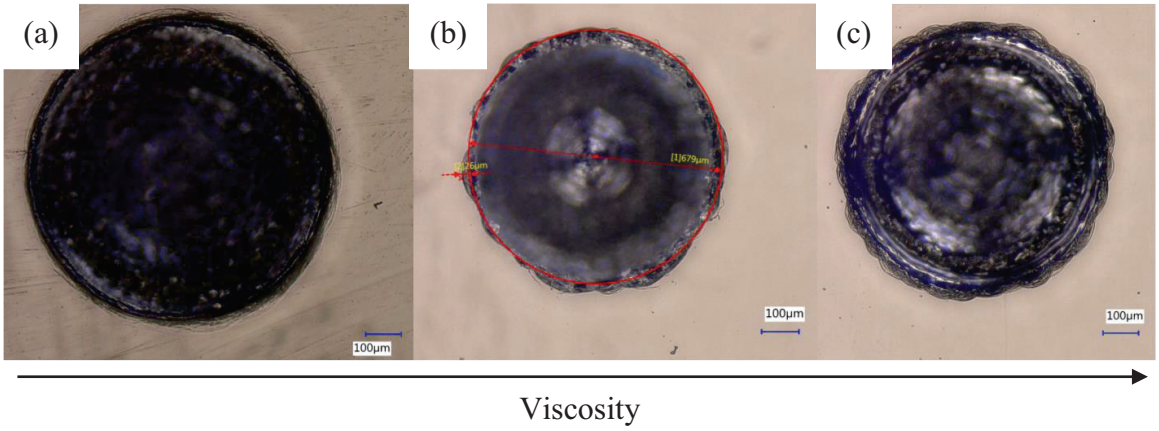


*Figure 18 : Example of hole entrance for different electrolytes (a) 26wt% KOH (b) 50wt% KOH (c) 30wt% NaOH.*

That being said, electrolyte base on KOH is clearly better in terms of drilling quality and speed. The machining speed can be improved by eight times by using 50wt% KOH over 30wt% NaOH. Also, KOH generates less defect and the type of defect generated are smoother. Finally, the general geometry of drilled holes with KOH is less flared. Because of all those facts, the KOH must be prioritized over NaOH. For the two set-ups used in this study, the best quality is obtained with 26wt% KOH without a big compromise on the machining quality.

Similar results can be observed in micro-channels machining. Figure 19 shows the general visual of micro-channels machined for two different electrolytes (50wt% KOH and 30wt% NaOH). In both pictures, we used the same set of electrical input parameters previously used for the drilling presented at the beginning of this section. With both electrolytes we observe jagged outline contours. The latter is less significant and the general shape is sharper when using 50wt% KOH. In addition to that, the groove machined with 50wt% KOH is deeper than with 30wt% NaOH, probably because of the same reasons presented before for the hole drilling (KOH electrolyte is less viscous).

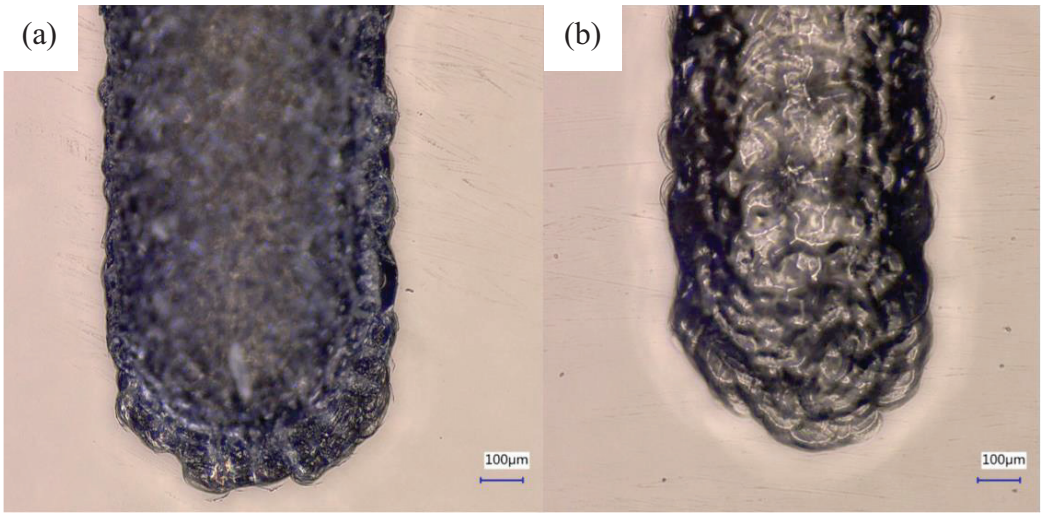


*Figure 19 : Example of hole entrance for different electrolytes (a) 50wt% KOH (b) 30wt% NaOH.*

In addition to that, tests were also made at Posalux SA to observe the effect of the electrolyte type on more complex geometries (pillars machining). Figure 20 shows the results of those tests. Again KOH has a better quality than NaOH. For further explanation about those tests see chapter 9.1.

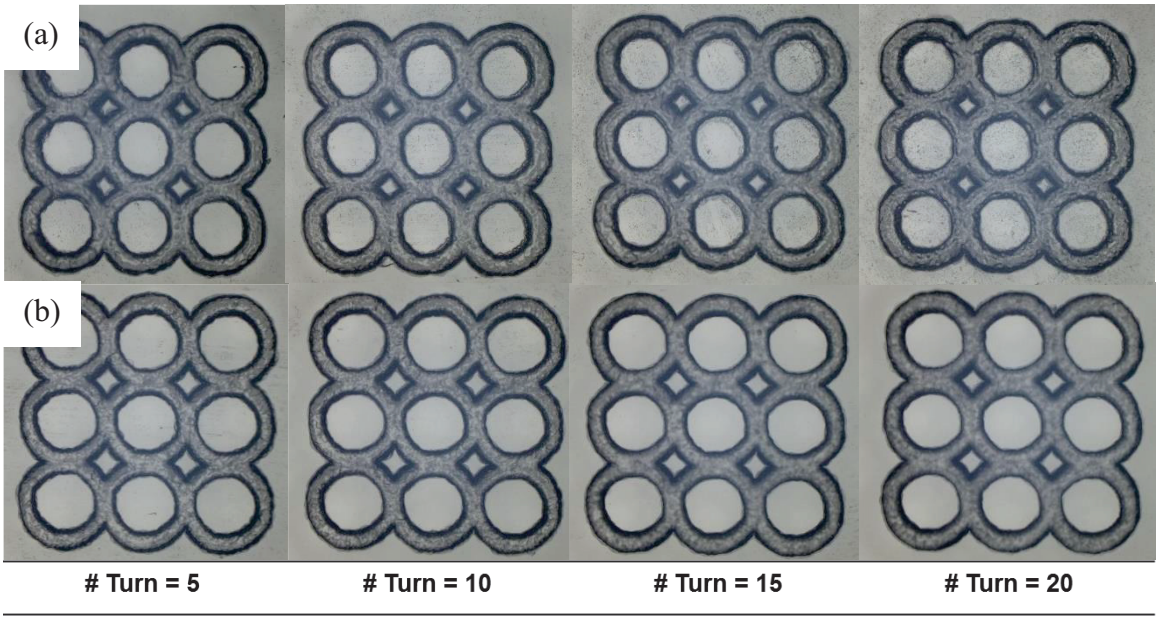


*Figure 20 : Difference in pillars of 100µm depth machined with polishing procedure (a) NaOH 20wt% (b) KOH 26wt%.*

## 4.2 Wetting agents (surfactant) Effect

As presented in section 0, it was suggested to add a wetting agent (surfactant) to the electrolyte to improve SACE machining quality. The effect of surfactant has been reported by [5] and more recently by [16]. In [5] the authors clearly expose the improvement in terms of surface quality for holes drilling by the use of a wetting agent. They explain this improvement of the quality by the reduction of the critical voltage. As a matter of fact, they did not use a pure wetting agent for those tests, they used a soap which contains wetting agents. Unfortunately, they do not specify the nature or the name of this soap. Therefore, we can speculate on the components of this soap or its combination, which induced this phenomenon. [16] presumed that the surfactant was one of the main wetting agents in modern soap and it was the component which lead to the result of [5]. They used a common surfactant from the soap industry the SDS. They noted an increase of the current density with the use of SDS during SACE machining. They also demonstrated a positive impact of the SDS on the machining speed (27% reduction of the machining time). Therefore, in this sub-section, the impact of different surfactants is investigated to better understand the influence of a wetting agent on SACE. But first, let us present a summary of the surfactant nature.

### *4.2.1 Surfactant theory*

Surfactants are used in various industrial products. In particular, surfactants are used in the chemical industry to make detergents and to separate DNA in biological research. More specifically surfactants can be used to make emulsifiers, dispersive agents, foaming agents, etc.

Surfactants are composed of a hydrophilic head and a hydrophobic tail. The hydrophobic tail is composed of a carbonic string. Because of its nature, surfactants tend to be adsorbed on liquid surfaces in order to reduce the free energy of specific phase boundary [37]. In the case of SACE, those interfaces are between the electrode and the electrolyte, between the electrolyte and the gas (bubble nearby the electrode). At a specific concentration, all surfaces and interfaces become covered by unimers of surfactants. After

this point micelles are created inside the liquid (Figure 21). Those micelles are composed of surfactant unimers placed in a spherical pattern to protect the hydrophobic tails of the aqueous environment. This transitional concentration is called the critical micelle concentration (CMC). At the CMC point and at a higher concentration, the only active surfactants unimers are those present at the interface. The micelles are simply an inactive reserve of unimers.

The hydrophilic head can be polar or not. In the case of an ionic surfactant, the head is negatively charged on the contrary the head is positively charged for a cationic surfactant. There also exists zwitterion surfactants. These have dipolar molecules with both a negative and positive ion head. This can be expressed according to environment.

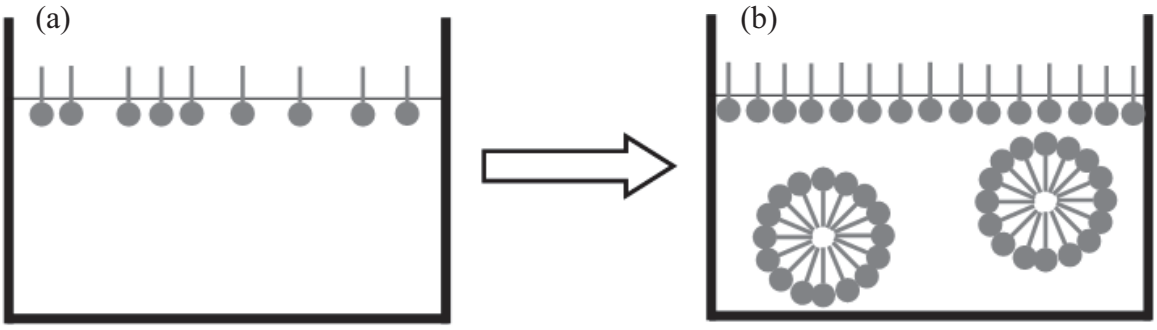


*Figure 21 : Schematic view of two liquid containers with a surfactant (a) the surfactant did not reach the CMC point, (b) concentration of surfactant over the CMC point and formation of micelles.*

In this study five different surfactants were used: Betaine, CTAB, TWEEN 80, SDS, Triton X-100. To test the effect of the hydrophilic head polarization, a variety of surfactant types were selected: 2 non-ionic, 1 Cationic, 1 Ionic, and 1 Zwitterion surfactant (Table 5).

*Table 5 : List of surfactants used in this work. The chemical formula shows the composition of a surfactant molecule (hydrophobic tail, hydrophilic head). The hydrophobic tail is composed of a carbon and hydrogen chain $C_nH_m$.*

| Surfactant | Type | Chemical Formula |
|---|---|---|
| **Betaine** | Zwitterion | $C_5H_{11}NO_2$ |
| **CTAB** | Cationic | $C_{19}H_{42}BrN$ |
| **TWEEN 80** | Non-ionic | $C_{64}H_{126}O_{26}$ |
| **SDS** | Ionic | $C_{12}H_{25}NaO_4S$ |
| **Triton X-100** | Non-ionic | $C_{14}H_{22}O(C_2H_4O)_n$ |

Because of the high concentration of electrolyte used in SACE machining, the mixing between surfactant and the electrolyte is difficult. The CMC point decreases with the increasing of the base salt concentration. This comes from the increasing of the ionic force inside the electrolyte. Prior to this, it is difficult to add the exact volume of surfactants inside the electrolyte to obtain a concentration under the CMC point. Typically, the CMC point for SDS in water is around 7-10mM and decreases exponentially with increasing concentration. In the next section we will see that the accuracy of the tests are limited. To find the optimum quantity of surfactants to add, a series of different surfactant concentrations have been tested.

### *4.2.2 Effect on the Critical Voltage*

The authors in [5] showed the influence of the wetting agent on the critical voltage. But, as we will see this effect is not observed in the frame of this work. The set-up presented in section 3.4 was used to observe the effect of the surfactant on the I-U properties. With this data acquisition technique, we can see the evolution in the critical voltage or in the critical current as presented in [5]. Figure 22 and Figure 23 show the evolution of the I-U curve as a function of the concentration of Triton X-100 in 26wt% KOH electrolytes. Figure 22 shows results in forward mode and Figure 23 in backward mode.

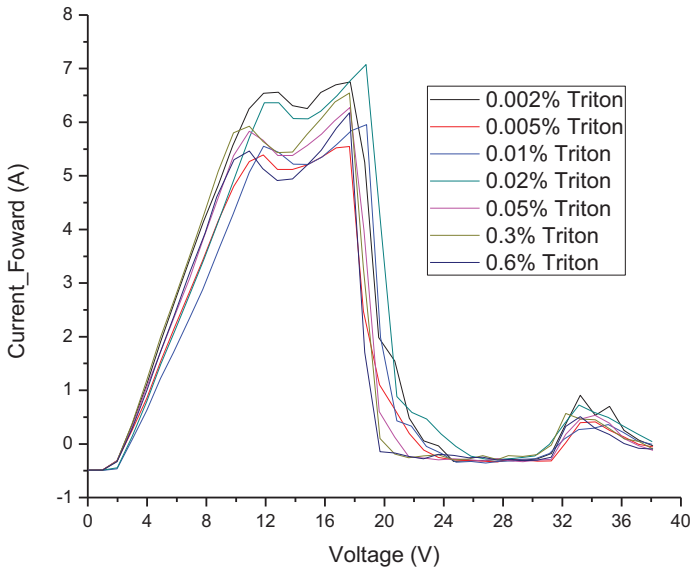


*Figure 22 : I-U curves in forward mode for different concentration of Trition X-100. The concentration is in %vol/vol.*

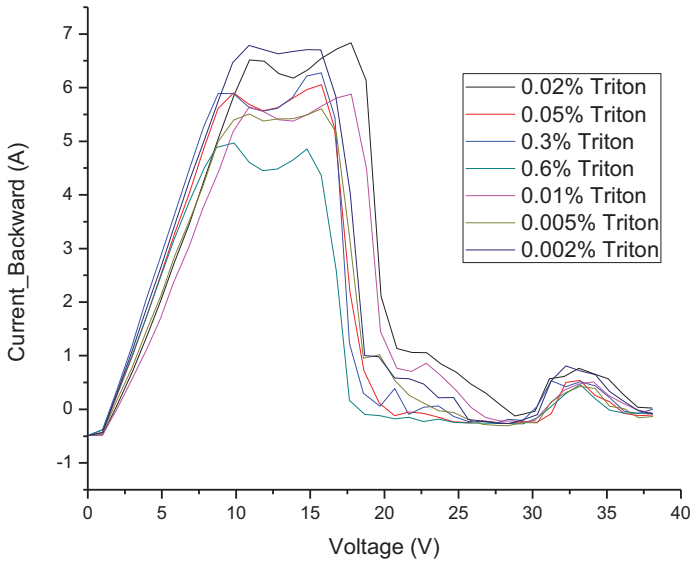


*Figure 23 : I-U curves in backward mode for different concentration of Trition X-100. The concentration is in %vol/vol.*

The values of the critical voltage and the critical current are listed in

Table 6. As we can see, the augmentation of the surfactant concentration increases the critical current up to a maximal value, than decrease along with the concentration

afterwards. The same obervation holds for the critical voltage. As for Triton X-100, the critical current increased until the concentration reached 0.02%vol/vol (volume of Triton X-100/ volume of electrolyte). This maximum value is the CMC point is characterized visually by the creation of white precipitates inside the solution. This precipate is an amalgam of micelles. They seem to have a negative impact on the system and interfere with the process. After a certain amount of time, the precipitate materials accumulate around electrodes.

*Table 6 : Critical voltage and critical current for different concentration of Triton X-100 in a 26wt% KOH electrolyte. Note the first row regroup the result of the electrolyte without surfactant.*

| **Triton Con.** | **Foward mode** | | **Backward mode** | |
|---|---|---|---|---|
| ***% Vol/Vol*** | ***Critical U (V)*** | ***Critical I (A)*** | ***Critical U (V)*** | ***Critical I (A)*** |
| **0.000%** | 17.65 | 5.43 | 16.73 | 5.228 |
| **0.005%** | 17.64 | 5.546 | 15.74 | 5.608 |
| **0.010%** | 18.8 | 5.956 | 17.77 | 5.876 |
| **0.020%** | 18.76 | 7.074 | 17.76 | 6.834 |
| **0.050%** | 17.68 | 6.274 | 15.76 | 6.056 |
| **0.299%** | 17.65 | 6.544 | 15.74 | 6.278 |
| **0.547%** | 17.69 | 6.75 | 15.7 | 6.702 |
| **1.039%** | 17.66 | 3.394 | 15.74 | 2.122 |

Other surfactants (Betaine, CTAB, TW-80 and SDS) give similar results (Figure 25). The CMC concentration obviously changes with the type of surfactant used.

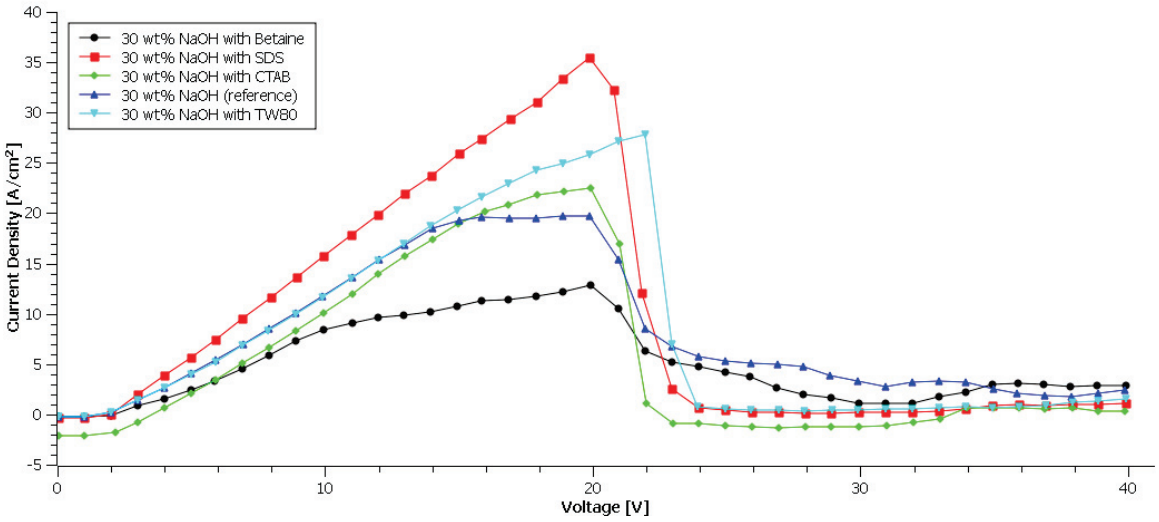


*Figure 24 : I-U characteristic curves for different surfactants (the surfactant concentration for each electrolyte is at the specific CMC point of each surfactant).*

The variation of the critical current with the surfactant concentration probably comes from the change of the contact angle between the tool-electrode and the electrolyte. To observe the contact angle between these two elements a high-speed camera and a data processing software camera were used (Figure 25 (a) and (b)). A tool-electrode attached to a micrometer stage is dipped inside the electrolyte. No electrical signal was applied. The focus of the high-speed camera was done on the tool-electrode and the electrolyte interface.

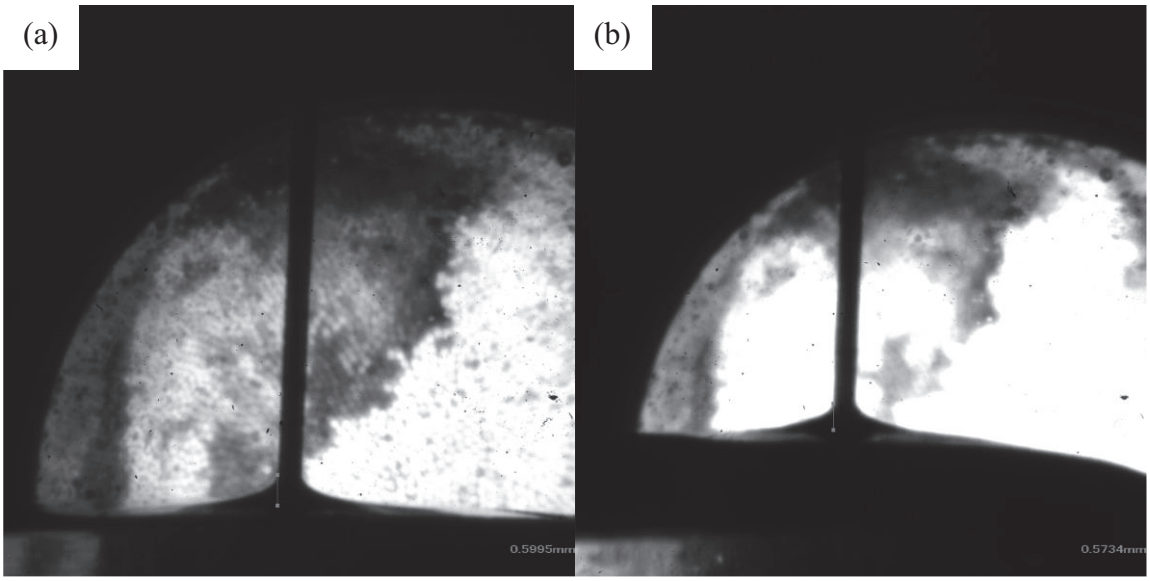


*Figure 25 : Picture taken with a high speed camera of the meniscus height between the tool-electrode and the electrolyte (a) 30wt% NaOH electrolyte (b) 30wt% NaOH with TW-80 surfactant.*

Table 7 shows the meniscus height for different electrolytes with surfactants. Meniscus heights has been found using an image processing program. The meniscus height is proportional to the contact angle, by capillary action. Thereby, the meniscus height is a good indication about the affinities between the tool-electrode and the electrolyte.

*Table 7 : Meniscus height in terms of the electrolyte use.*

| Electrolyte | meniscus height [mm] |
|---|---|
| ***30 wt% NaOH (reference)*** | 0.5995 |
| ***30 wt% NaOH with Betaine*** | 0.8448 |
| ***30 wt% NaOH with CTAB*** | 0.5888 |
| ***30 wt% NaOH with TW-80*** | 0.5734 |
| ***30 wt% NaOH with SDS*** | 0.513 |

By the I-U signal and the meniscus height, we can say that the surfactants do not have a significant impact on the critical voltage, critical current and on the contact angle. The variation of the critical voltage is only about 6% of maxima for Triton X-100. All considered, this is not large and cannot by itself explain the effect of surfactants on SACE. Same statement holds for the contact angle. For machining tests, unfortunately the two SACE set-up used in this study do not allow to machine with surfactants. Because of the nature of surfactants, the surfactant molecules stay confined within the overflow system and does not reach the machining zone. Therefore, the effect of the surfactant on SACE machining is not well understood. The result obtained by [5] probably comes from a mix of surfactants and other agents which are difficult to replicate. However, surfactants can still have a slight influence on SACE. For this though, we need to have a processing cell without flow and as we will see in the next chapter the electrolyte flow is essential to obtain a good quality and should not be removed (chapter 4).

## 4.3 Electrolyte at Eutectic Point

Another possibility of electrolyte is a mix between multiple salts. During SACE machining, molten materials (glass, electrolyte salt) are formed between the tool-electrode and the work-piece. The idea of mixing multiple salts is to have a lower melting temperature thus increasing the machining capability. The typical temperature of the

machining tool-electrode is around 500-600 $^0$C [17]. However, this temperature decreases rapidly along with the distance from the tool-electrode. Perhaps we would get more molten materials with a lower melting temperature salt. [38] shows that with a eutectic mix, the melting temperature can decline to 174.5 $^0$C, which is lower than for pure KOH or NaOH (Figure 26).

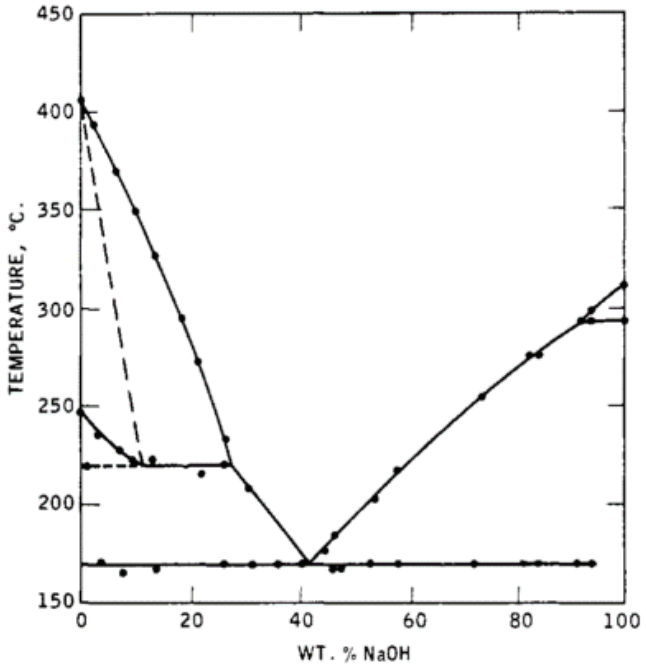


*Figure 26 : Solid liquid phase diagram in the KOH-NaOH equilibrium. This phase diagram come from the Harry W. Otto and Ralph P. Seward publication* [38]*, with the authorisation of the American Chemical Society.*

NaOH and KOH respectively have a melting temperature of 319.3 $^0$C and 409.5 $^0$C. The eutectic point of the NaOH-KOH mix is for a salt composed of 41% NaOH and 59% KOH. Figure 27 demonstrates that we can have the same electrical properties with eutectic electrolyte as well as with pure salt. Note the eutectic weight percentage in Figure 27 refer to the proportion of eutectic salt in the electrolyte. Regarding the conductivity, it acts the same way as pure salt (Figure 28). Data show in the last graphic are obtain by using an electrical conductivity meter and a heat plate. After a set of machining experiment, the machining did not change with the used of an eutectic salt.

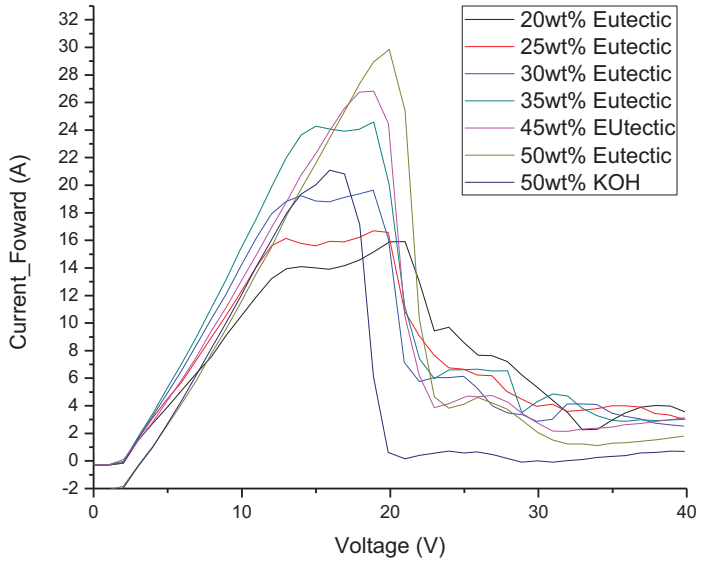


*Figure 27 : I-U curves in forward mode for different concentration of eutectic mix and 50wt% KOH.*

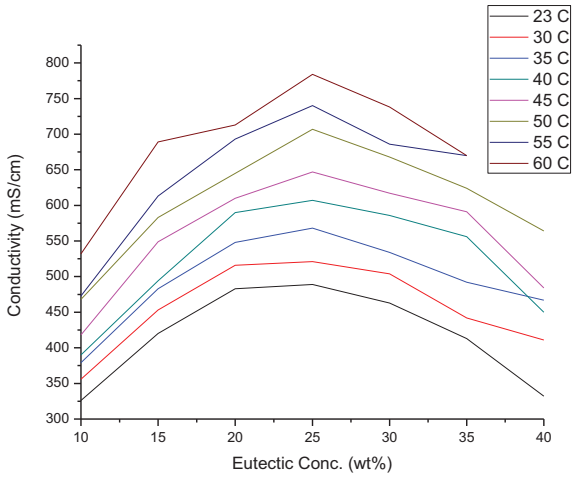


*Figure 28 : Evolution of the electrolyte conductivity in function of the eutectic concentration for different electrolyte temperature.*

## Conclusion

It is better to use a KOH based electrolyte instead of a NaOH base electrolyte. A KOH based electrolyte has superior properties for the SACE process. A KOH based electrolyte has better thermal and hydrodynamic properties than a NaOH based electrolyte. KOH in an aqueous form is less viscous, because of that KOH the microscopic and bulk flow are more efficient. Also, the machining speed and the machining quality with KOH is much better than with NaOH. Because of all that KOH should be prioritise over NaOH for future work. It seems the best electrolyte concentration is around 26wt% KOH in term of machining quality.

The use of surfactant and eutectic electrolyte do not seem to really improve machining performance. Also, the use of certain surfactant can bring some safety and environmental issue such as the Triton X-100. Also, the use of surfactant adds more complexity to the process. Because of that to improve the SACE process it is better to work on other avenue.

# Part II: Thermo-hydrodynamic Approach

# 5 Hydrodynamic Consideration

SACE process appears to be dependent on the thermodynamic and hydrodynamic behavior at the vicinity of the machining zone. This thermo-hydrodynamic determines the machining quality and speed. Therefore, general observation of the macroscopic flow in the processing cell made during tests are present to highlight the influence of the thermo-hydrodynamic in the SACE process. More specifically, this chapter investigates the influence of the bulk flow (section 0). Emphasis is put on visual observations of the SACE process and on educated guess with the technology. The bulk flow can be characterized by two parameters: the electrolyte level and the electrolyte circulation generated by the pumping system. The influence of these two macroscopic parameters on SACE are discussed.

## 5.1 Electrolyte Level

Because of the set-up limitations (section 3.1) we cannot simply adjust the electrolyte level. To change the electrolyte level with an overflow system, we need to adjust the relative height between the two concentric cylinders of the processing cell. Unfortunately, the processing cell is constructed from an acrylic monolithic bloc which cannot be adjusted.

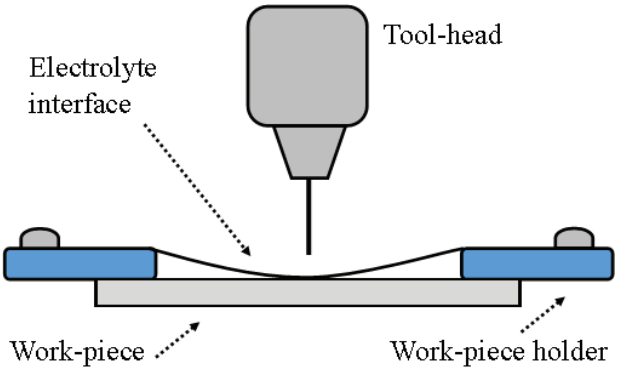


*Figure 29 : Schematic side view of the distribution of the electrolyte level over the work-piece with the effect of the work-piece holders.*

However, to observe the electrolyte level effects, we can use the contact angle between the electrolyte and the holding system. Other devices such as work-piece holders can influence the electrolyte level. The work-piece holding system is built of clamps which are over the work-piece corners and screwed in the acrylic processing cell. The electrolyte has a low contact angle with the work-piece holders (acrylic) so it tends to rise near the work-piece holder (Figure 29). Because of that, the machining efficiency and quality as a function of the electrolyte level can be investigated qualitatively. To test this, a series of 16 holes, spaced by 4mm was drilled in order to cover all the work-piece. The drilling was done in 30wt% NaOH with a 500µm tool-electrode diameter rotating at 500rpm under 37.5V DC. All machined holes were drilled on the same work-piece. The result is presented in Figure 30. The holes machined near the work-piece holder is lower in quality because of the current increase which is caused by the increase of the electrolyte level. The current density needs to reach a certain value to achieve the gas film building, this explains the increase of the current at the vicinity of the holding system. Therefore, a low electrolyte level is needed to have superior machining quality. Yet, a too low level could result in local drying at the machining zone. In fact, when the electrolyte pumping system is stopped, quickly arises local drying around the tool-electrode which prevents any machining to occur. A strict balance is needed to avoid this local drying specially because of the viscosity and the surface tension of the electrolyte. When local drying occurs, there is no way for the system to rewet the surface.

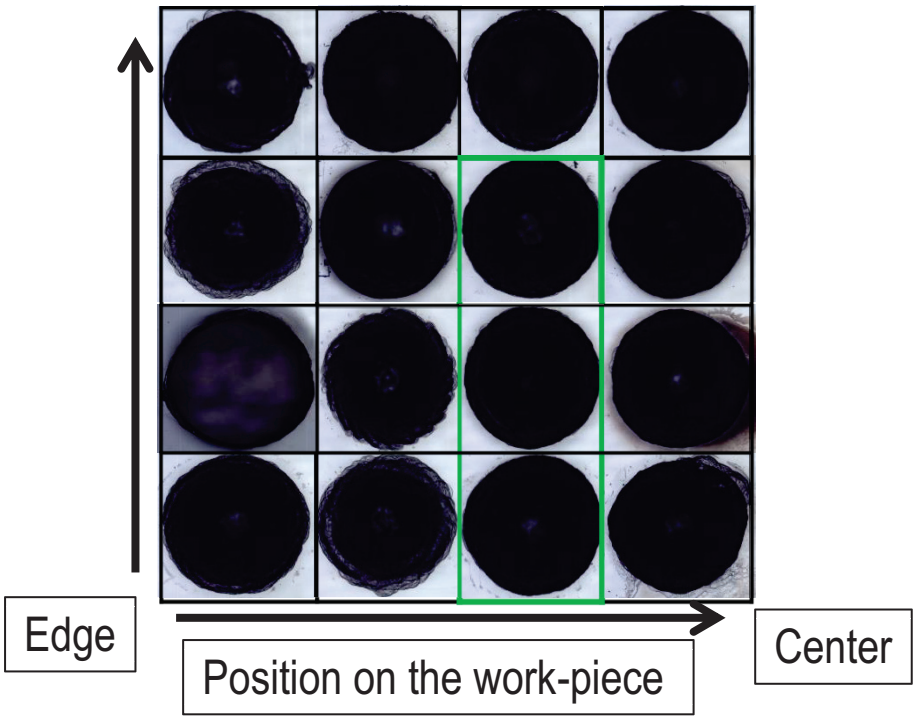


*Figure 30 : Machining quality evolution in function of the position on the work-piece. Two work-piece holders are situated near the upper and bottom left corner of the graph. Best hole drilling quality is identifying by a green rectangle.*

Visibly, it is better to stay with one electrolyte level and optimize the other parameters around it to maintain optimal machining speed and quality. Inconveniently, when we change the electrolyte level all other parameters need to be adjusted to the new configuration. When we change the electrolyte level the tool-electrode surface submerged in the electrolyte change, this is accompanied by a change in the current concentration. Therefore, the change in electrolyte level correspond to a change in hydrodynamic and thermodynamic properties around the tool-electrode. This is why the electrolyte level chosen is fixed to 1.5mm.

## 5.2 Electrolyte Flow (From the Overflow System)

The Electrolyte flow, as discussed in section 0, is the bulk electrolyte motion in the processing cell. This bulk electrolyte circulation inside the cell is mostly uniform. This uniformity is caused by the overflow system. To investigate the relation between the electrolyte flow rate and the machining quality, a series of experiments were made (

Table 8 and Figure 31). Note that the electrolyte level is not the same for all set of parameters (

Table 8). In Figure 31, one can discern that there is an optimum electrolyte flow. The quality of the machining reaches an optimum point and decreases afterwards. This probably comes from the thermal energy concentration at the machining zone. When the electrolyte flow is under a certain level the heat concentration is too important, which leads to a poor quality. If the electrolyte flow is too substantial, it will cause too much turbulence around the machining zone. Hence, a balance between the heat concentration and the flow is needed. Because of the hydrodynamic regime, when increasing the machining depth the electrolyte flow needs to be increased as well. When the hydrodynamic regime takes place a more important electrolyte flow is needed to provide fresh electrolyte at the machining zone (increase of the microscopic flow).

*Table 8 : Electrolyte flow in relation to the pump speed.*

| Pump Position | Electrolyte Level (mm) | Electrolyte Flow (ml/s) |
|---|---|---|
| **1** | 1.0 | 0.6 |
| **2** | 1.5 | 1.1 |
| **3** | 1.5 | 1.5 |
| **4** | 1.5 | 2.2 |
| **5** | 1.5 | 2.7 |
| **6** | 1.5 | 3.1 |

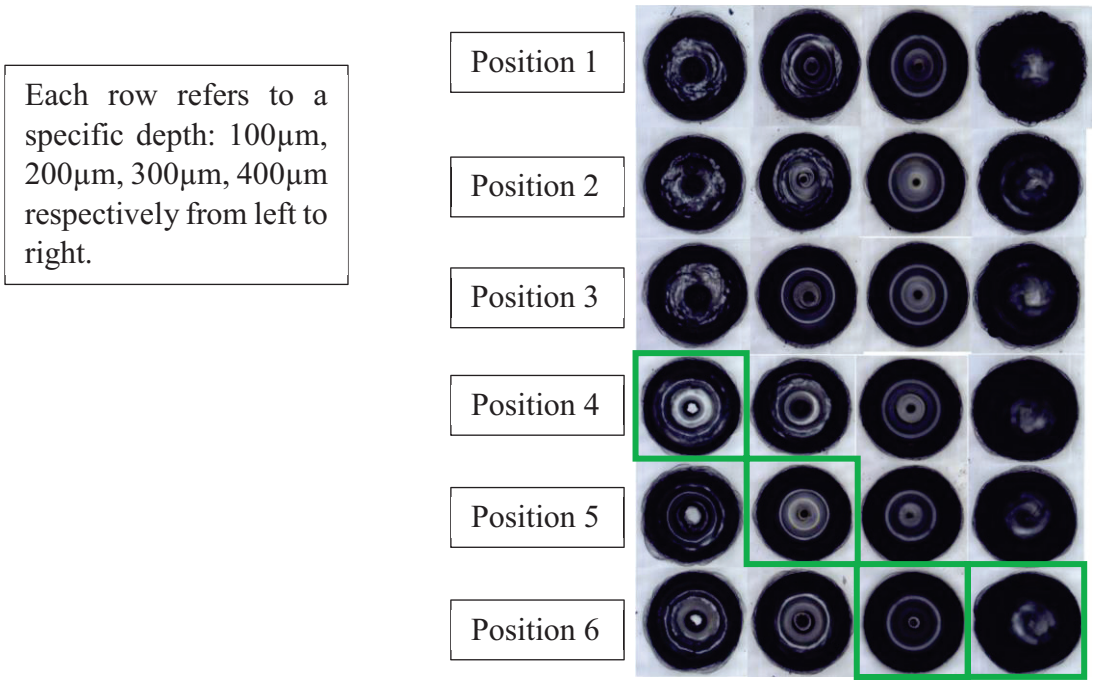


*Figure 31 : Evolution of the machining quality in function of the electrolyte flow with 30wt% NaOH electrolyte, 37.2V DC, 500rpm, 500µm tool Ø. Best hole drilling quality is identifying by green rectangles.*

### *5.2.1 Electrolyte Nozzle*

The Posalux SA machine in addition to the overflow system has an electrolyte nozzle (section 3.2). This nozzle allows to have a further degree of control on the bulk flow by providing a directional flow (Figure 32). The difference in pillars machining quality in function of the relative position of the electrolyte nozzle is shown in Figure 32. The red arrows represent the general electrolyte flow pattern. Note that the size of those arrows do not refer to a variation in the flow speed.

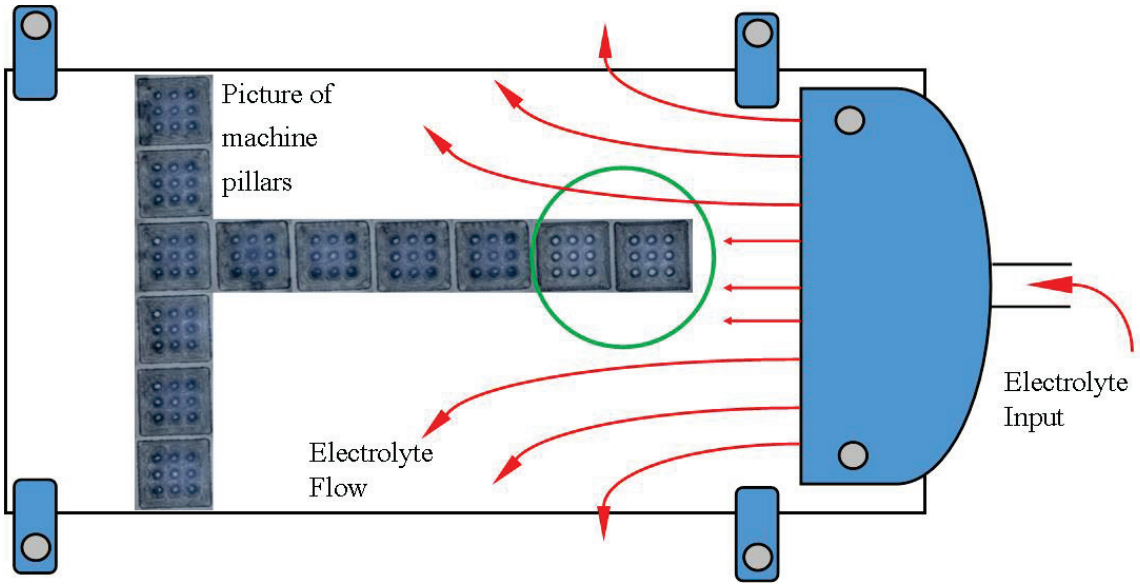


*Figure 32 : Multiple pillar machining with the evolution of the machining quality in function of the relative position from the electrolyte nozzle. Rough machining high-level=33V, low-level=17.5V, ontime=1.5ms, offtime=1.5ms; Polishing machining high-level=30V, low-level=14V, ontime=1.5ms, offtime=1.5ms. 4 step rough machining, polishing gap=40µm, tool=50 µm, 10 turns, speed=60mm/min*

The machining quality decreases with the increase of the distance from the electrolyte nozzle. In Figure 32, the machining quality increases with the electrolyte flow. This directional electrolyte flow though has a drawback. The machining lacks uniformity and depends on the relative position of the electrolyte nozzle. Figure 33 presents machined pillars with circularity defects depending on the electrolyte flow direction.

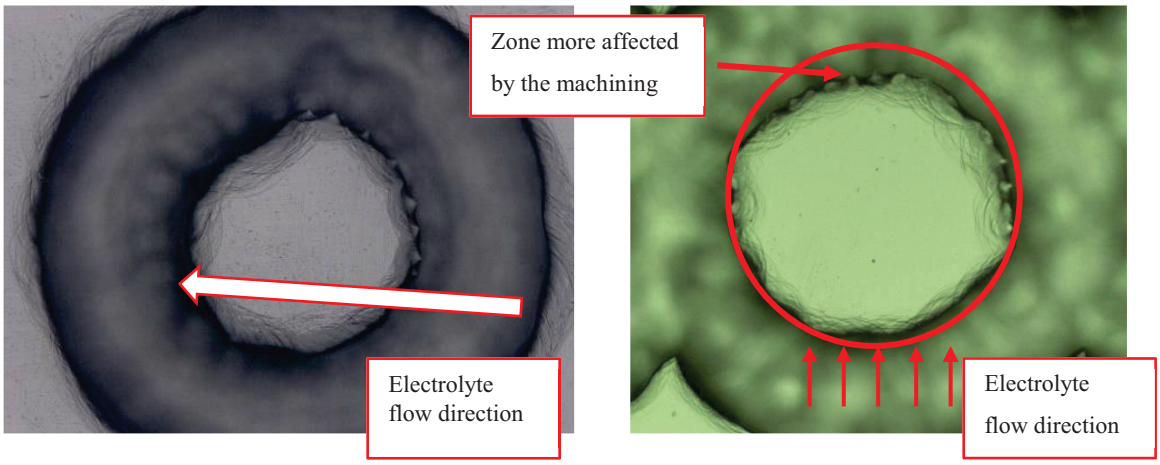


*Figure 33 : Circularity defect of machined pillar in function of the electrolyte flow direction. Machining parameters: high-level=33V, low-level=17.5V, ontime=1.5ms, offtime=1.5ms; 4 step rough machining, polishing gap=40µm, tool=50 µm, 10 turns, speed=60mm/min.*

The material removing rate is higher on the opposite side of the electrolyte flow. An explanation of this phenomenon can be provided by studying a cylindrical object in a forced flow. This well know problem in fluid mechanic is called Stokes flow. In our case the cylindrical object is the current machined pillar and the flow is turbulent because the Reynolds number is approximately equal to 150 (Equation 2). In Equation 2, ρ is the density of the electrolyte, μ is the dynamic viscosity of the electrolyte, v is the electrolyte flow speed and r the radius of the pillar. According to the KOH salt provider and the KOH handbook[3] at room temperature ρ≈ 1500Kg/m$^3$ and μ≈ 1.5cP for a concentration of 26wt%.

*Equation 2*

$$Reynolds\ Number_{2D\ circle} = R_e = \frac{\rho v L}{\mu} = \frac{\rho v (2r)}{\mu}$$

The effect of a cylinder in a directional flow with Re between 35 and 200 was reviewed in many studies such as [39]. At Re≈150 a phenomenon called vortex shedding occurs. There is a separation in the flow and the formation of sheer layers in front of the cylinder. The shear layer rolls up into a vortex behind the cylinder. In addition to that, when Re>49 a vortex grows larger than the other and forms an instability. When we study this phenomenon by simulation, it appears that the flow velocity in front of the cylinder is reduced. In our case, there is more electrolyte flushing behind the pillar than in front of the pillar on account of this. Because of that, the etching is slower in front of the pillar because of the lack of OH- radical.

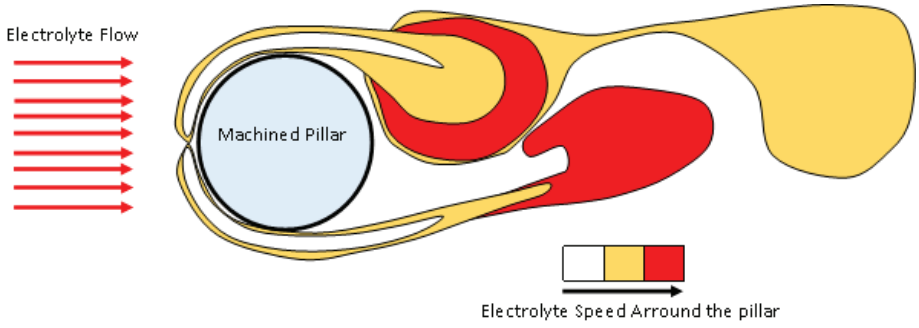


*Figure 34 : Schematic view of the electrolyte circulation around the machined pillar. We see low speed zone in front of the pillar and the turbulent mixing behind the pillar.*

[3] Occidental Chemical Corporation, Basic Chemicals Group, Occidental Tower, 5005 LBJ Freeway, Dallas, Texas, 75244

## 5.3 Conclusion

Within this chapter, we observed the effect of the bulk flow. The electrolyte flow is essential in obtaining a superior machining quality and avoid any local drying during machining. Also, the bulk flow need to be optimize to have an equilibrium between the hydrodynamic and the thermodynamic regime at the vicinity of the machining zone. Other observations made in this chapter are listed bellow:

- When the drilling becomes deeper we have to increase the bulk flow to keep the machining quality.
- Increasing of the bulk flow can increase the microscopic flow, specially during holes drilling.
- If we machined at higher input voltage, we have to increase the bulk flow to dissipate the additional heat from the machining zone and prevent HAZ.
- A better work-piece holding system has to be developed, to prevent any variation in the electrolyte level.

# 6 Tool-electrode Rotation

In this chapter, the influence of the microscopic flow (section 0) is investigated. Analysing previous works leads to the conclusion that a static tool-electrode does not provide sufficient machining quality and slows down the machining speed. A rotating tool-electrode creates a microscopic flow around itself by the action of the shear force. The microscopic flow increases proportionally to the rotation. By increasing the microscopic flow, it decreases the thermal energy at the machining zone. Figure 35 shows the effect of the tool-electrode rotation on two different sets of electrical input. As we can see if we increase the heat input at the machining zone we need more microscopic flow to obtain the same quality. Therefore, the heat control at the machining zone can be achieved by tuning the tool-electrode rotation speed.

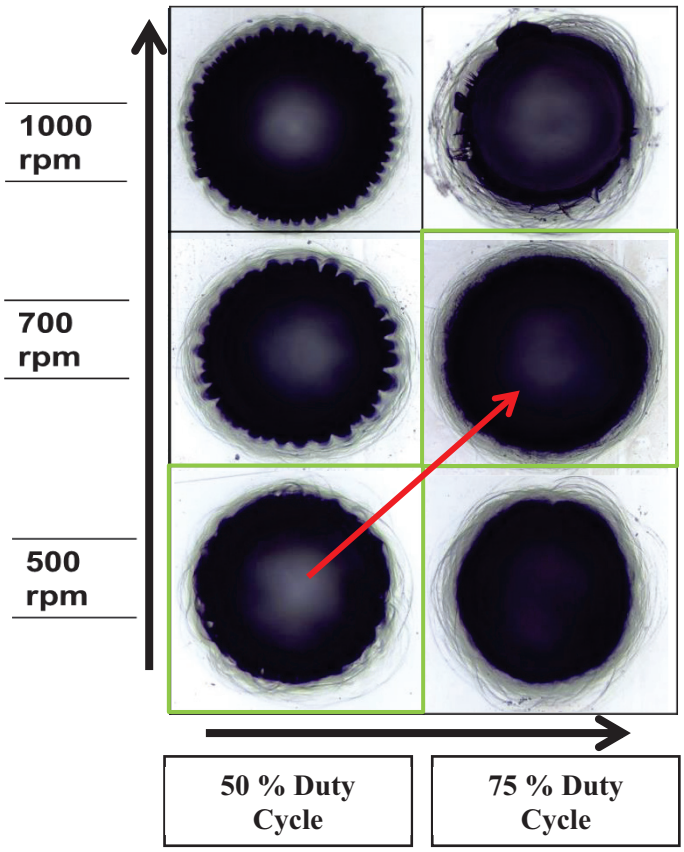


*Figure 35 : Evolution of the optimal duty cycle for different tool-electrode rotation speed. Tests made with 30wt% NaOH, Period=3ms, High-level=37.2V, Low-level=9.5V.*

From those results we can find a possible way to control the machining quality by varying the tool-electrode rotation. This variation needs to consider the thermal energy input. For example, if the machining parameters are set to: gravity feed drilling, 30wt% NaOH, 3ms electrical period, High-level 37.2V, Low-level 9.5V, 0.5mm tool-electrode diameter the tool-electrode rotation will reach its maximum machining quality at 450rpm and 550rpm (Figure 36). The value of 500rpm is not include probably because this value does not generate a proper electrolyte circulation. Therefore, the value of 450rpm and 550rpm may be generate Taylor vortex inside the drill hole.

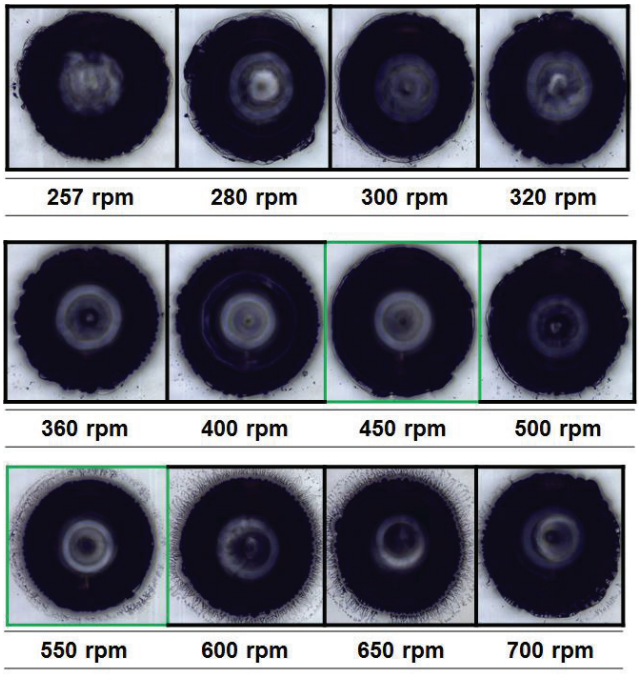


*Figure 36 : Evolution of the machining quality with the tool-electrode rotation speed; Gravity feed drilling, 30wt% NaOH, 3ms electrical period, High-level 37.2V, Low-level 9.5V, 0.5mm tool-electrode diameter.*

## 6.1 Conclusion

There is an optimum combination of bulk and microscopic flows for a specific set of parameters. This can be achieved by the variation of the tool-electrode rotation. This optimum combination seems to be dependent on the hydrodynamic and the heat dissipation around the machining zone.

# 7 Tool-electrode Geometry

Tool-electrode geometry as presented in (section 2.2.2) have a great impact on the machining quality and more significantly on the machining speed. The tool-geometry influence the microscopic flow the same way a rotating tool-electrode do. Note that a shaped tool-electrode needs to rotate to have an influence. Several geometries have been used by other groups in past decade (section 2.2.2). In [22] the authors show the effect of a modified tool-electrode tip. They reveal that a flat side tool-electrode increases the drilling speed. But to obtain the geometry of those tools the authors need specific and complex piece of equipment such as wire electro-discharge grinding (WEDG) [22]. Therefore, the idea of this section is to find and test a tool-electrode geometry which can increase the machining quality, decrease the machining speed and does not need complex equipment for its fabrication (i.e. no WEDG). Also, the geometry has to take in account the tool wear and mechanical resistance. The tool-electrode wear comes from the electro-erosion due to the concentration of the electrical field.

The tool-electrode geometry chosen for this study is a cylinder with a strait bevel angle on the tip (Figure 37 (a) and (b)). This type of geometry as not yet been investigated by previous studies. This tool-electrode geometry can be achieved by using a common diamond grinder on a stainless steel rod. The use of a diamond grinder allows a faster and cheaper tool-electrode fabrication process than the use of WEDG. The grinder used to provide minimum grinding scratch on the tool surface because of the fine grid of the diamond grinder (Figure 37(b)). This idea come from two observations. The first observation is with smaller tool-electrodes we have a higher machining speed, because of the heat and sparks concentration. The second observation is that the machining speed is dependent on the microscopic flow. Therefore, a tool-electrode with a bevel can play the role of a heat and spark concentrator and of a mixer.

(a)

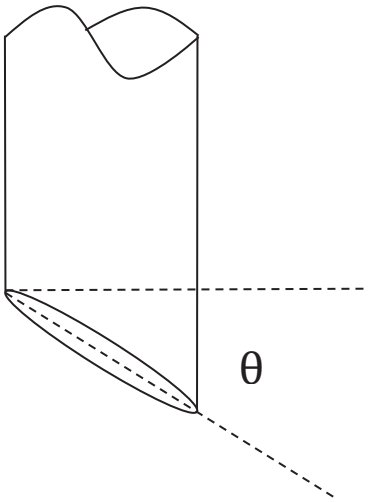


(b)

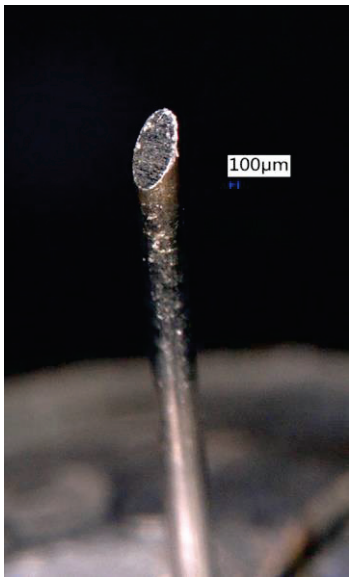


*Figure 37 : (a) schematic view of the tool-electrode geometry tested (b) picture example of a tool-electrode with a 60º bevel angle tip.*

To investigate this tool-electrode geometry a series of tests using four different angles θ have been done to see the influence of a modified tool tip on the machining speed. The four tool angles are 0º (flat tool), 15º, 45º, 60º. The error on the tool tip angle is about ±3º. Every tool used had a 500µm diameter and made from stainless steel (A151318) cylindrical rod. A greater angle than 60º is not possible to achieve with this machining technique in our laboratory.

To test the impact of those tool tips, a series of fifty holes of 300µm depth are drilled for each tool angle. The hole drilling is performed using a fixed input signal of 2.5ms period with low-level time of 0.1ms, high-level voltage of 34V and the low-level voltage of 17.5V. During the drilling the tool-electrode rotate at 500rpm.

## 7.1 Results and Discussion

In this subs-chapter results of the tool-electrode geometry study are presented and discussed. The influence of the tool bevel angle is presented using graphic representation of depth in function of the time. This plot is often used in SACE publication. Also the machining time for specific depths is presented.

### 7.1.1 *Drilling Time Evolution*

Figure 38 presented the drilling depth in function of the machining time for the 0º, 15º, 45º and 60º bevel angle. Each curves are the mean value over fifty drill holes. We clearly see that the 60º bevel angle is the best angle in term of machining speed. This is in total agreement with the hypothesis (in the introduction of this chapter).

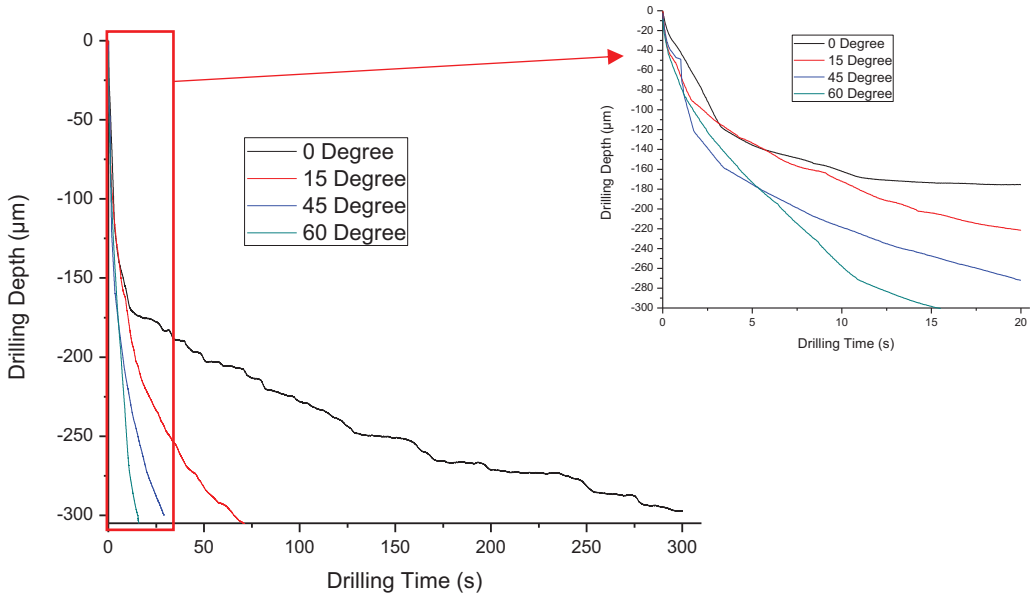


*Figure 38 : Depth in function of the time for 0º, 15º, 45º and 60º bevel angle with a focus on the transition region.*

The transition between the discharge and the hydrodynamic regime is around -150µm for every tool-electrode tip angle (Figure 38). In the discharge region the drilling is faster and driven by the number of discharges in the gas film. At -150µm the machining speed drops significantly because of the lack of fresh electrolyte inside the drilled hole. The drilled hole entrance is obstructed by the gas film. The -150µm transition depth was already observed by [7] and [23]. Therefore, the discharge regime seems to not been influenced by the bevel angle tip. Because of that an angle tip tool-electrode does not seem to concentrate more the electrical field than the flat tip tool-electrode. Another explanation of this phenomenon is in the discharge regime we are limited by heat propagation speed in glass. Thus, the evolution of the machining speed as a function of the angle tip is probably coming from the best electrolyte circulation around the tool-electrode with a tip.

To have a better overview of the machining time in function of the tool-electrode bevel see Table 9. Note that the values presented in the Table 9 are only valid for a tool-electrode with a 500µm diameter under the condition specified before.

*Table 9 : Drilling Time in function of the depth and the tool-electrode bevel angle.*

| Depth (µm) | Drilling Time (second) | | | |
|---|---|---|---|---|
| | 0º Angle | 15º Angle | 45º Angle | 60º Angle |
| **50** | 1.17±0.07 | 1±2 | 1.1±0.2 | 0.5±0.2 |
| **100** | 3±1 | 6±7 | 2.0±0.5 | 1.5±0.9 |
| **150** | 10±8 | 14±18 | 4±2 | 4±3 |
| **200** | 39±24 | 25±23 | 11±6 | 9±7 |
| **250** | 105±50 | 51±45 | 28±13 | 17±9 |
| **300** | 206±46 | 52±34 | 47±17 | 22±13 |

A wider bevel angle than 60º probably increase the drilling speed. But a wider angle than 60º is difficult to obtain with the fabrication technique used. Also, a non-uniform tool-electrode tip is probably more efficient because of the electrical field concentration (Figure 39(a)). A non-uniform tool-electrode tip is more difficult to obtain and need the use of more sophisticated equipment than a diamond grinder. Also, a non-uniform tool-electrode tip is more fragile especially with a small tool diameter and subject to tool wear. To test the efficiency of a concentrated electrical field, a series of holes have been drilled with a needle type tool-electrode (Figure 39(b)). The drilling speed is less fast with a needle tool-electrode; this is a strong indication that a non-uniform tool-electrode tip can be better in terms of drilling speed. The needle tool-electrode has not put in the general comparison because a needle type tool-electrode do not drill cylindrical holes, the ending hole is more or less like a cone (Figure 39(b)).

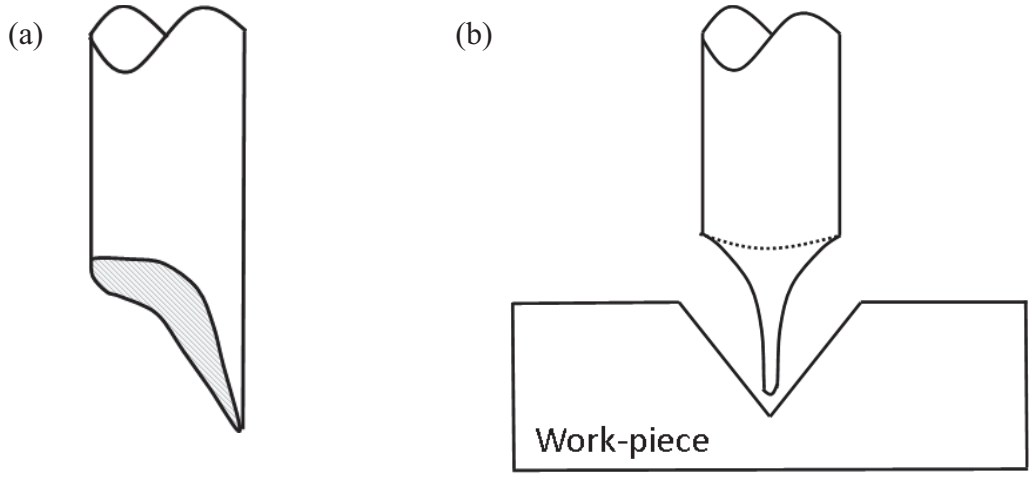


*Figure 39 : (a) schematic view of a non-uniform tool-electrode tip (b) hole drilling with a needle type tool-electrode.*

### *7.1.2 Holes Quality*

Quality does not seem to change significantly in function of the bevel angle with the exception of the flat tip tool-electrode (Figure 40). The drilling quality is worst with a flat tool-electrode tip. The type of defect present on the hole edge in the case of drilling with a 0º bevel angle is typical of defects cause by a gas film instability. This is surprising because of the higher drilling time the tool tip is more in contact with a specific point of the surface so more time to refine the surface. Those types of defects usually appear at high machining speed. The defect present at the hole entrance with the other tool-electrode look more or less like thread.

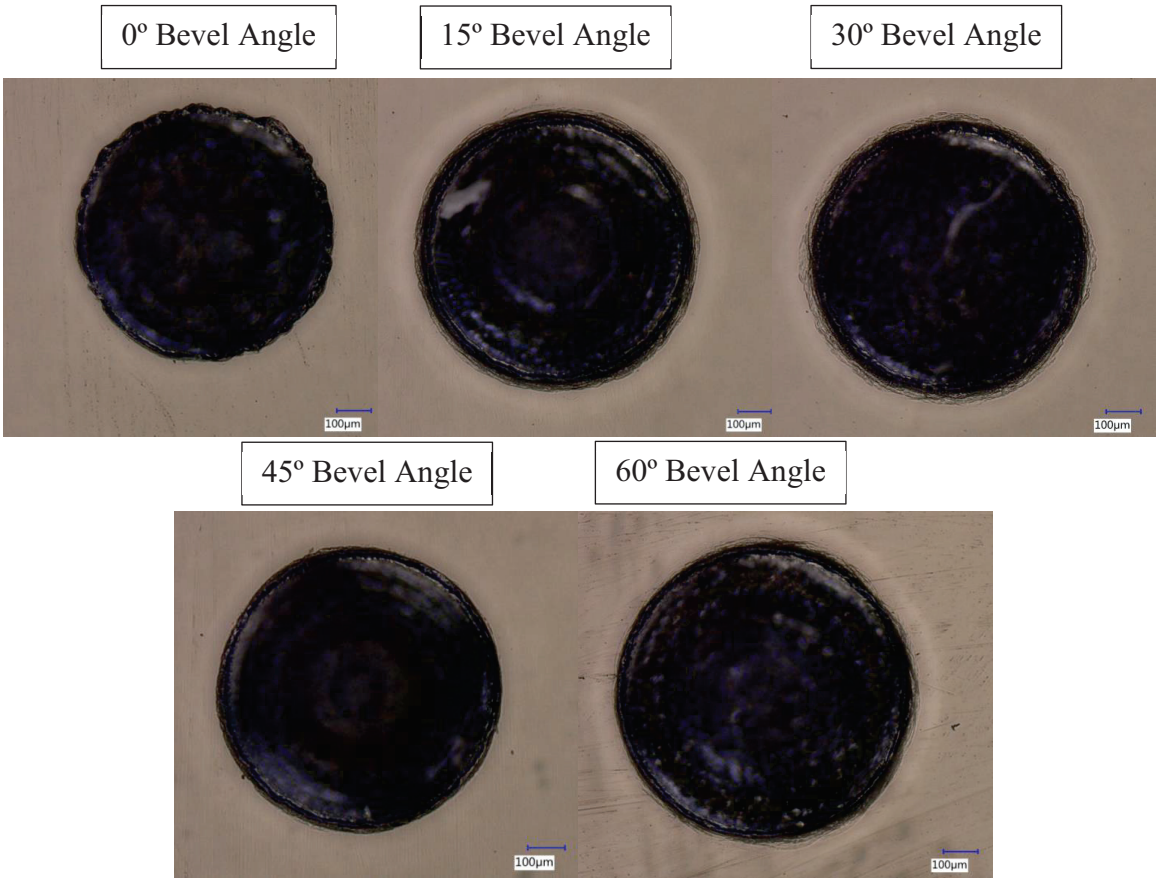


*Figure 40 : Example of the drill quality for different tool-electrode bevel angle tip.*

This type of pattern is probably caused by the form of the electrolyte circulation around the tool-electrode. It appears the microscopic flow is dependent on the tool-electrode type. The electrolyte enters in the drill hole and move circularly around the tool drag by the tool-electrode rotation, in the case of a tool-electrode tip angle superior to 0º. Also, if we take in account the hole entrance diameter (Figure 41) the volume inside the hole which can be filled by electrolyte increase of 60% between the 0º tool-electrode tip and the 60º tool-electrode tip for a 300µm hole depth. This was calculated using:

*Equation 3*

$$\% = \frac{Volume\ 60^{\circ} - Volume\ 0^{\circ}}{Volume\ 0^{\circ}} = \frac{\pi[r_{hole}^2 h - r_{tool}^2(h - r_{tool}tan\theta)] - \pi h(r_{hole}^2 - r_{tool}^2)}{\pi h(r_{hole}^2 - r_{tool}^2)}$$

Therefore, it seems the bevel angle has a positive impact on the electrolyte circulation during the drilling. By positive impact we mean a positive impact on the drilling speed. In terms of hole dimensions, the holes entrance increases with the bevel angle

(Figure 41). Holes entrance diameters presented in Figure 41 is an average over the series of fifty holes. The increase of hole entrances can be caused by two phenomena. Firstly, the increase of the electrolyte circulation in the hole can increase the overall machining and induce an increase of the hole dimension. There is more run-out with a high bevel angle tip, because of the non-uniform pressure applies to the tool-electrode tip in gravity feed mode drilling. A tool-electrode with a higher run-out tends to machine wider structure. An indication of the possible increase of the run-out with a high bevel angle tip is the evolution of the standard deviation of the bevel angle. The standard deviation is supposed to increase with the run-out it is what we observe.

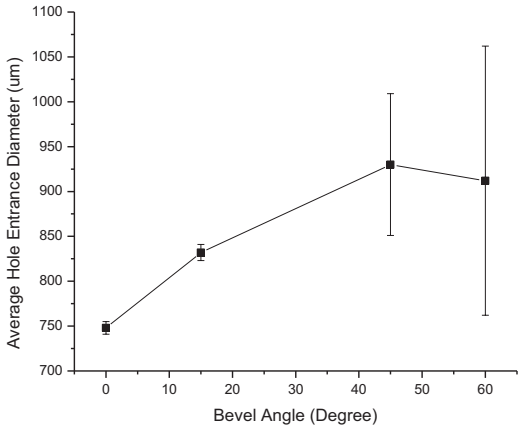


*Figure 41 : Average hole entrance diameter in function of the tool-electrode bevel angle.*

## 7.2 Conclusion

SACE glass drilling speed can significantly be improved by using a cylindrical tool-electrode with a bevel angle tip. This is truer at drilling depth higher than 200µm, i.e. beyond the discharge regime. The evolution of the tool-electrode angle on the drilling speed seems to come from the better circulation of the electrolyte in the drilling zone.

# 8 Electrical Input Signal Optimization

There are three possible ways to obtain a desired machining quality:

- *First possibility*: Optimization of the electrical signal to obtain the desired surface quality. After this optimization the work-piece is machined. This optimization can be at the detriment of the machining speed. The idea is to obtain the desired machining in just one single pass.
- *Second possibility*: Do a fast machining at high voltage and polish the created rough surface after that (chapter 0).
- *Third possibility*: A combination of the first and second strategy.

The focus of this chapter is put on the first possibility. As discussed in (section 2.2.4), the electrical input signal has a significant impact on the machining quality and the machining speed. This comes from the fact that the heat energy transferred to the machining zone is determined by the electrical input. Also, as we will be seen in section 8.1, the electrical input influence the gas film dynamics. The creation and collapsing of the gas film interacts with the microscopic flow around the tool-electrode and a random gas film dynamic can lead to a non-uniform machining quality. So, by this fact, the electrical input also has a hydrodynamic influence. For this study, in the continuity of the previous works, a pulsed voltage is used (section 2.2.4). To characterize a pulsed voltage, five main electrical input properties are used: signal form, high-level, low-level, electrical period, duty cycle. Figure 42(a) shows a schematic view of a pulsed voltage signal with all important properties. The period represents the time of a full cycle of the signal (the sum of the on-time and the off-time). Note that during the off-time the voltage is not necessarily equal to zero. Also, the low-level and the high-level refer to the voltage during the off-time and the on-time interval respectively. Finally, the duty cycle is given by Equation 4:

*Equation 4*

$$Duty\ Cycle = \frac{Ontime}{(Ontime + Offtime)} = \frac{Ontime}{Period}$$

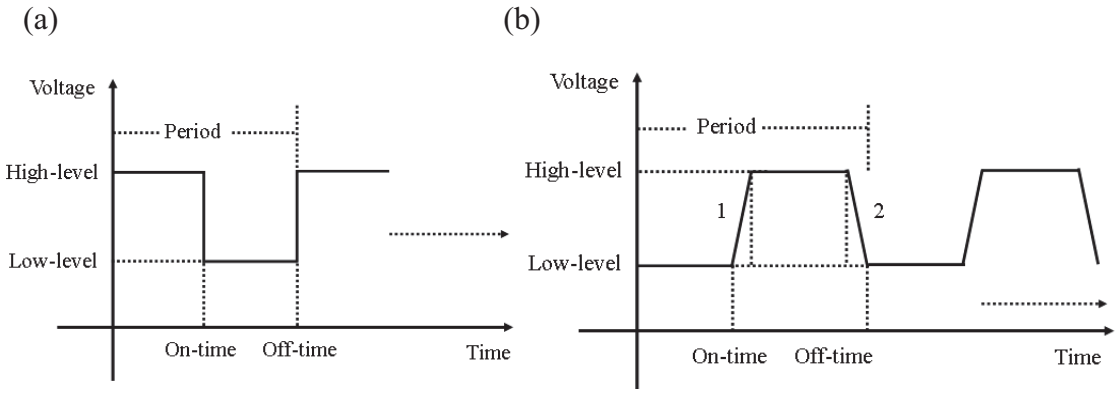


*Figure 42 : (a) schematic view of a pulse input signal. Therefore, the period refers to the time of a full cycle, the low-level refer to the voltage during the off-time interval, the high-level refer to the voltage during the on-time interval. (b) pulse voltage with rising edge and falling edge.*

Other pulsed signal properties, such as the rising edge and the falling edge (Figure 42(b)), were not investigated. Also, different signal shapes (sinusoidal, triangular, and square) can have different influence on SACE. To restrain the amount of work, the main focus of this study is put on the square signals. This type of signal was chosen because of its historical background in SACE technology development [22], [28], [29], [30], [40] and [41]. Because of the wide variety of possible parameters combinations and the time needed to achieve this variety of tests, it is difficult to have a solid and final picture of the electrical signal impact on the machining quality and the machining speed. In addition, the optimum combination of parameters is likely to vary with the surrounding environment (type of electrolyte, electrolyte levels, electrolyte flow, nature of the work-piece, tool-electrode runout and the machining strategy) and by extension with the machine structure geometry.

First of all, let's introduce some observations made in other studies. In [29] the authors present the influence of the period and the duty cycle on hole drilling. Without surprise, this study shows that the SACE material removal rate increase with the increase of the duty cycle and the period (the increase of the input energy increases the removing rate). The authors used three duty cycles (25%, 50% and 75%) and three periods (1s, 10ms, 0.1ms) for their tests. The machining quality has been studied by [29] and reveal that lower duty cycle and higher pulse frequency increase the machining quality. Another study [22] investigated the effect of the duty cycle on hole drilling. More specifically they showed the

influence of the pulse-off times during machining. Similar effects presented in [29] have been observed: when the pulse-off time increases the machining time increases and this results in a decrease of the hole entrance diameter. This study ([22]) used pulse-on time fixed at 2ms and six different pulse-off time (0.1, 0.5, 1, 1.3, 1.5 and 2ms). The authors also give an explanation for this phenomenon: the pulse-off time act as a cooling time during the machining. When a voltage is applied at the tool-electrode, the temperature increases and on the contrary when the voltage is turn-off the temperature decreases. With a less important average temperature, the removal rate and the HAZ length decrease. Therefore, the taper effect can be reduced by an increase of the pulse-off time. Moreover, SACE machining allows more operations than just drilling. [28] investigates the effect of pulse-off time on milling (microgroove machining). Again the same effect is observed during microgroove machining: the machining rate is reduced with the rise of the pulse-off time. Also, the groove width decreases with the rise of the pulse-off time.

Up to now, all studies presented used a low-level equal to 0V. The authors in [30] are the first, to our best knowledge, to introduce an offset during the pulse-off time (low-level voltage not equal to 0V). They claimed that with the use of a low-level equals to 0V, the gas film is less stable and the output current signal is more random. Therefore, based on their studies and explanations, the gas film stability can be improved by using a non-zero low-level voltage. The mean machining time and deviation can be improved by 60%. Also, by using a non-zero low-level voltage, an improvement on the machined geometry (less taper effect) is observed. Therefore, the use of a pulsed input signal with an offset is a compromise between the machining quality and the machining speed. Also, the use of a low-level equal to 0V increases the wear of the tool-electrode [42]. Because of that, in this present work, only pulsed voltages with an offset are used. There are some observations already made on the effect of a non-zero low-level. In [42] the authors used a constant offset voltage of 10V referring to the high-level. Different high-levels are used: 23V, 27V, 30V, 33V, 36V. In their study they note an optimum point in terms of machining quality. When the high-level voltage increases the surface roughness decreases until it reaches 30V and increases after that. This optimum point is valid only for 20wt% KOH, 0.5ms/0.5ms pulse on/off-times applied on a quartz work-piece. This optimum point comes can be

explained as follow: if the low-level is higher than the critical voltage, there are also sparks during the off-time; in this case, the off-time does not play the cooling effect desired.

The use of a pulsed voltage does not only act as a cooling effect but also stabilizes the gas film building and collapsing dynamics. Under a DC voltage, the gas film building and collapsing frequency is random (following a Poisson process [43]]). By using on-times below the average gas film life-time, one insures to have a constant gas film dynamic. This consistent dynamic can provide a more uniform machining because some machining defects are caused by non-uniform gas film or electrolyte circulation (section 2.2). Therefore, the effects of the pulse-off time and the low-level depend on the build-up and the life time of the gas film under specific conditions. If the low-level is far under the critical voltage, the gas film building time after the low-level will be higher.

In general, as we can conclude from previous studies, the use of a pulsed input signal corresponds to an increase of the machining time and the machining quality. Hence, the idea is to find a compromise between the machining speed and the machining quality. If the machining quality is poor, we will need more polishing to obtain the desired quality for the application (chapter 0).

On the contrary, if the low-level is higher than the critical voltage, the gas film is quicker to build. According to [44], in a 30wt% NaOH electrolyte, the average gas films life time is around 10-50ms and the average gas film formation is around 2.4-3.1ms depending on the applied voltage. The average gas film formation time decreases with the applied voltage and reaches a plateau at 28V. This is obvious because the increase of the voltage corresponds to an increase of the gas production at the tool-electrode surface. At the opposite, the average gas films life time increases with the input voltage. Obviously, the values presented before are valid only for 30wt% NaOH; those values depend on the critical voltage and the fluid dynamics of the electrolyte.

## Pulse voltage tests

Tests presented in this chapter were made with the Concordia University set-up (section 3.1). Those tests aim to validate the affirmation that a pulse input voltage affects the machining quality by changing the thermodynamic regime around the tool-electrode. Therefore, those tests are not being done under the strict consideration of the build time and life time of the gas film. This give an overview of the possibility an electrical input optimization can give in terms of SACE machine quality.

First of all, let us present a test which replicates the tests made by [42]. Figure 43 and Figure 44 show the evolution of hole drilling for two different electrolytes flushing rates in the processing cell. The circulation flow was set at 0.6ml/s for Figure 43 and at 1.5ml/s for Figure 44. Also, for those tests the low-level is set at 70% of the high-level. This proportion is more or less the same 10V offset voltage referring to the high-level of [42]. The high-level vary from 26V to 37V. In addition to that in Figure 43 and Figure 44, the holes have a depth of 0.5mm with a tool-electrode diameter of 250µm. The machining is made by 0.1mm depth step (section 3.3). For all tests the others machining parameters are: 30wt% NaOH electrolyte, tool rotation at 500rpm, period at 3ms and duty cycle at 50%.

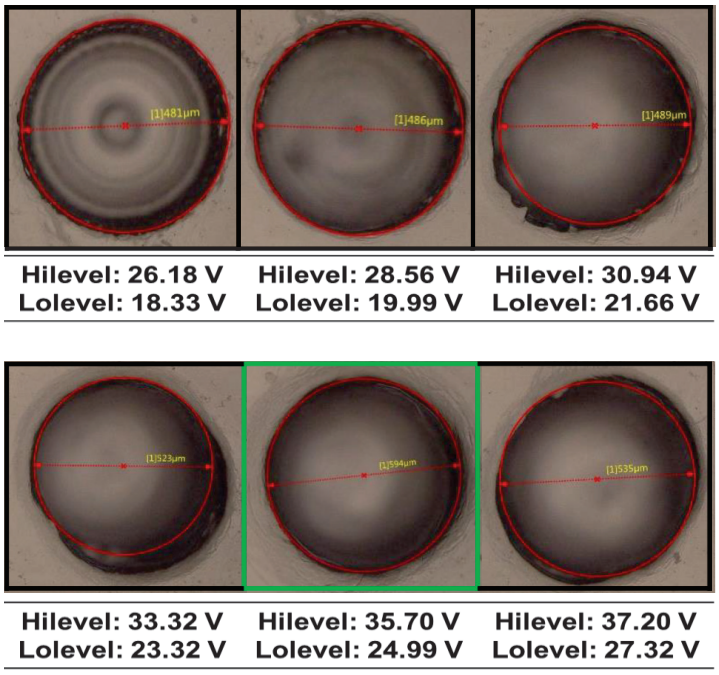


*Figure 43 : Electrolyte level 1.5mm and electrolyte circulation 0.6ml/s (30wt% NaOH, 250µm tool-electrode Ø, 500rpm, T=3ms, dc=50%)*

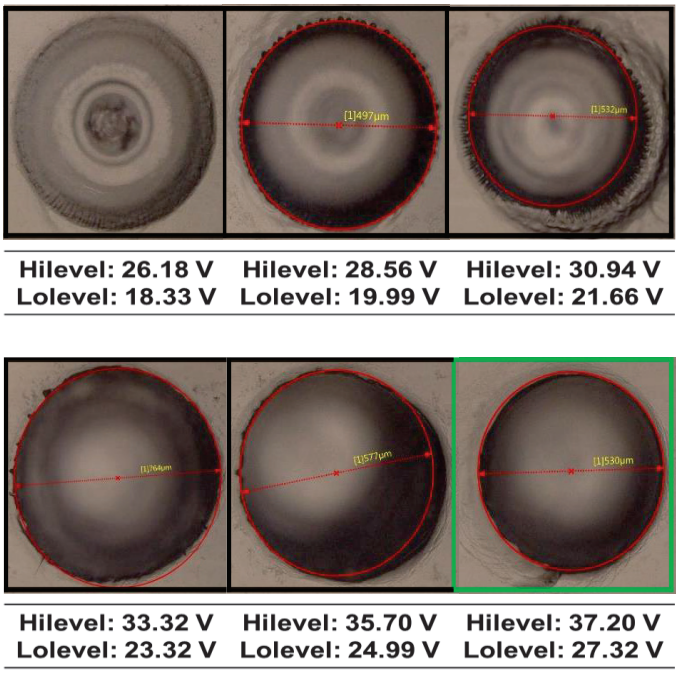


*Figure 44 : Electrolyte level 1.5mm and electrolyte circulation 1.5ml/s (30wt% NaOH, 250µm tool-electrode Ø, 500rpm, T=3ms, dc=50%)*

We clearly see that there is an optimum setting for which the machining quality is significantly improved. For an electrolyte circulation flow of 0.6ml/s in the processing cell, the optimum combination of parameters is 35.70V for the high-level and 24.99V for the low-level. Whereas for an electrolyte circulation of 1.5ml/s, the optimum combination of parameters is 37.20V for the high-level and 27.32V for the low-level. Therefore, we can see that the optimum combination of parameters depends strongly on the surrounding environment during the machining. Also, with a higher flushing rate in the processing cell, we can increase the overall voltage level. Because of those two observations, we can say that the optimum combinations of parameters depend on the heat distribution and the hydrodynamic around the tool-electrode.

To test the effect of the low-level, a series of holes of 0.5mm depth with a tool diameter 250µm were done. Drilling was also made by 0.1mm steps (Figure 45). Figure 45 show similar result as in the Figure 43 and Figure 44. Similar results have been found with the use of different duty cycle and similar period.

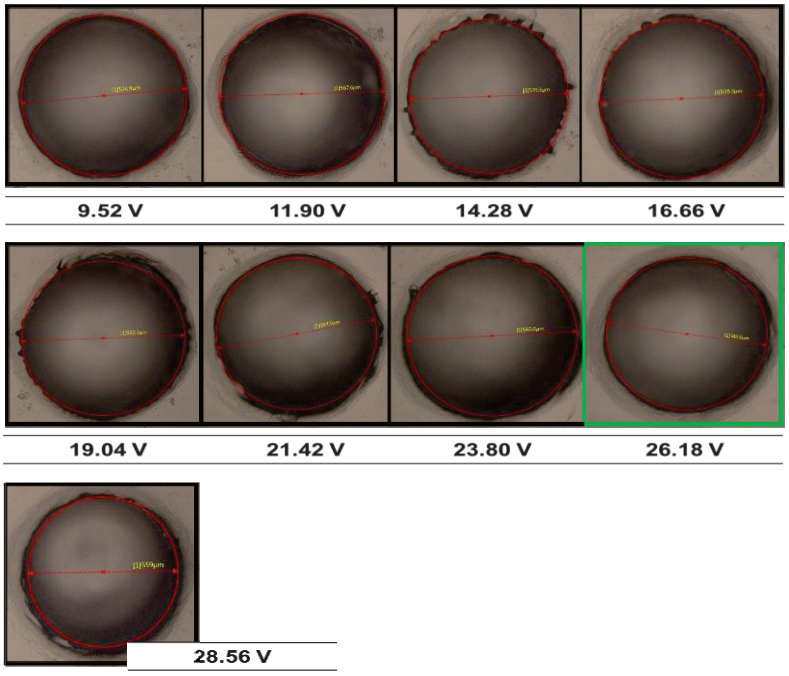


*Figure 45 : Influence of the low-level for a fix high-level of 37.2V (30wt% NaOH, 250µm tool-electrode Ø, 500rpm, T=3ms, dc=50%)*

## 8.1 I-t Signal

In this section, the amount of energy and the gas film dynamics of different electrical inputs are investigated via the I-t signal (section 3.4). More specifically the I-t signal gives information about the gas film dynamics and the spark regime. Also, it can give more specific value such as: the time needed to build a gas film, the time between each gas film collapsing and formation. One of the hypothesis to explain the better machining quality with the pulse voltage is the increase on the gas film stability under this type of electrical signal. According of previous work the theoretical gas film life time ($\Delta t_f$) is defined by:

*Equation 5*

$$\frac{\Delta t_f}{\Delta t_b} = \frac{1}{1 + [p_c/(1-p_c)]\widetilde{U}} ln\left[\frac{\widetilde{U}}{(1-p_c)(\widetilde{U}-1)}\right]$$

Where, $p_c$ is the percolation threshold from the stochastic model developed by Wüthrich [19], $\widetilde{U}$ is the normalised voltage and $1/\Delta t_b$ is the mean detachment frequency of bubbles. The normalised voltage is defined by:

*Equation 6*

$$\widetilde{U} = \frac{U - U_d}{U^{crit} - U_d}$$

Where, $U_d$ is the water hydrolysis voltage (about 2.2V), $U_{crit}$ is the critical voltage after which the sparks regime appear. Experimentally, $\Delta t_f$ and $\Delta t_b$ values have been reported by [44]. [44] proposes an algorithm based on wavelet analysis which measure the gas film life time and building time. With this algorithm, the authors find a gas film building time between 1-3ms and a gas film life time between 50-10ms. The signal acquisition was done via an Agilent current probe model N2774A—50MHz connected to a Newport XPS hardware/software system (Universal High-Performance Motion Controller/Driver) at 10kS/s sampling rate on a 0.04s window.

This algorithm was tested but no significant result has been found with this technique. In fact, the 10kS/s sampling rate is low compared to the duration of the physical process involved. To test this algorithm, we used a sampling rate of 1.25MS/s on a 0.04s

window. The algorithm based on the wavelet analysis as a denoising tool with the discrete Meyer wavelet with a current signal of 1.25MS/s cannot differentiate the spark discharges and the gas film building signals. We found a gas film building time around 0.1ms by simple visual observation of the current signal, with a similar counter electrode diameter. If the values obtained by [44] are valid, we should not see spark discharges for a electrical period of 3ms (no gas film building) this is inconsistent with the experiments. Therefore, the value obtained in [44] overestimates the average building time and life time of the gas film. The authors suggest that the highest current peaks are the gas film building, because of the sampling rate used, it is likely that a lot of information was lost.

To investigate the I-t signal, we used the set-up detailed in section 3.4. For those tests, two electrolytes have been used: 20wt% NaOH and 26wt% KOH. Since the algorithm described previously is not directly adaptable to the SACE process, the gas film dynamics was manually analyzed. Also, using a Matlab program, the mean output current is observed. To stay in the context of this study, the emphasis is put on pulsed voltage. Note that [44] only shows results for DC input voltage.

### *8.1.1 Results and Discussions*

In

Table 10, we can see the average current for two different DC input voltages. The average current gives information about the gas film stability and the number of gas film formation and collapsing under a specific voltage. If the average current increases, it means there is more gas film formation and collapsing (the current which passing between the two electrodes is higher during the gas film formation than during the sparks regime). As we can see from (

Table 10), the average current is roughly the same for a specific input voltage regardless of the electrolyte type.

*Table 10 : Mean out-current for two different electrolytes for three different input DC voltage.*

| Electrolyte | Input Voltage (V) | Average Out-Current (A) |
|---|---|---|
| **20wt% NaOH** | 26 | 0,40 |
| **20wt% NaOH** | 30 | 0,21 |
| **20wt% NaOH** | 34 | 0,19 |
| **26wt% KOH** | 26 | 0,44 |
| **26wt% KOH** | 30 | 0,16 |
| **26wt% KOH** | 34 | 0,18 |

The results presented in

Table 10 mean that the gas film stability is similar between the two electrolytes. However, the viscosity of those two electrolytes is different (Table 3). Because the average out-current is almost the same between the two electrolytes for a specific input voltage, it seems that the gas film formation and stability is not dependant on the electrolyte viscosity. We can see this visually in Figure 46. Also, we observe a diminution of the average current with the increase of the input voltage. This means that increasing the input current increases the gas film average life time.

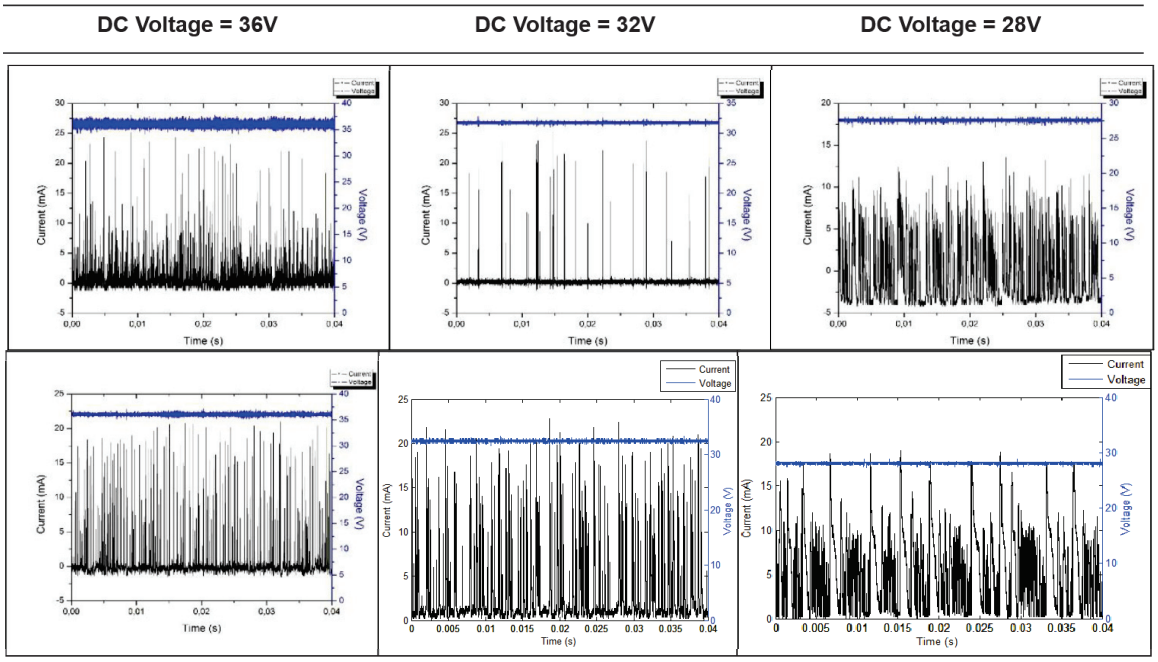


*Figure 46 : Example of I-t signal under different condition. The upper row refer to 26wt% KOH and the lower row refer to results using 20wt% NaOH.*

For pulsed input voltage, one has to take into account the influence of the low-level. In fact, the variation in the input voltage forces a collapsing and a re-build of the gas film. This dynamic does not depend on the low-level even if the low-level is above the critical voltage (for 20wt% NaOH the critical voltage is approximatively 21V and for 26wt% KOH it is 18V). Figure 47 present a typical I-t signal for a pulsed input voltage. The current was smoothed to see more clearly the gas film building. We clearly see there is no spark discharges during the off-time. In this region, the current signal is typical of water hydrolysis. At the beginning of the on-time, we observe a large current emission; this is the gas film building.

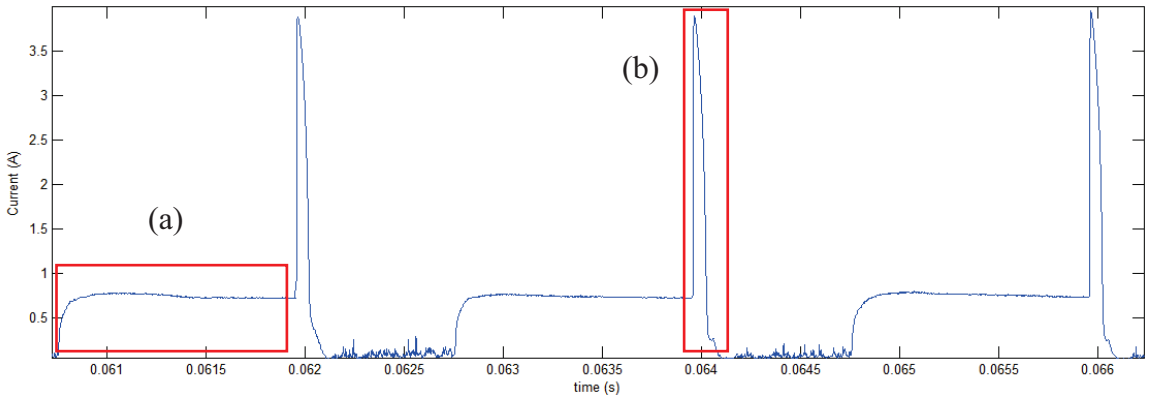


*Figure 47 : 26wt% KOH, period=2ms, high-level=38V, low-level=7V, duty cycle=40% (a) hydrolysis of water (b) gas film building.*

Therefore, based on I-t measurements, it is possible to find the gas film building time. For the parameters used in Figure 47, the average values of the gas film building time over fifty gas film building are presented in Figure 48 as a function of the duty cycle. The decrease with increasing duty cycle probably comes from the corresponding variation in the local temperature around the tool-electrode. We clearly see the gas film building time observed is far from the previous value obtain with a lower sampling rate.

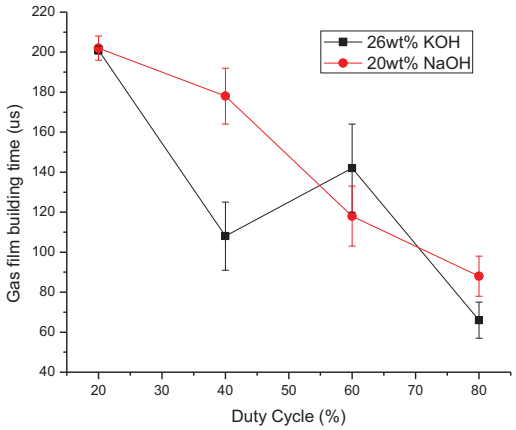


*Figure 48 : Influence of the duty cycle on the gas film building time for: high-level=38V, low-level=7V, period=2ms*

The influence of the low-level and the period on the gas film building time was also examined (Figure 49). In general, the gas film building time seems fairly independent of the period. But the gas film building time decreases with the increase of the low-level. This is attributed to the fact that with a higher low-level, higher is the hydrolysis current; less time this needed after the off-time to finish the gas film building.

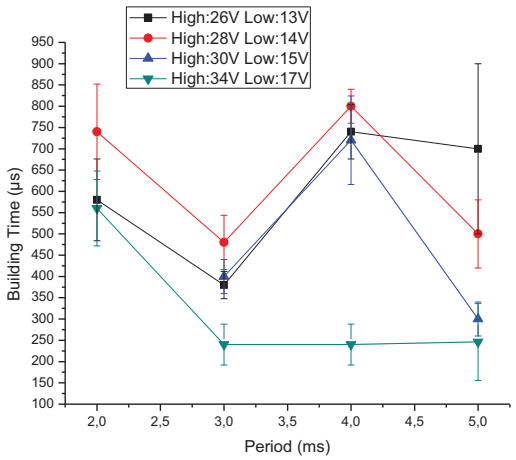


*Figure 49 : Influence of the period on the building time for 26wt% KOH with a duty cycle=60%*

Even if the low-level is set to 0V, the gas film formation-time stays below 1ms (Figure 50). Note that in Figure 50, a smaller counter electrode was used (Ø= 3cm). The

duration of the gas film formation depends strongly on the distance between the tool-electrode and the counter electrode.

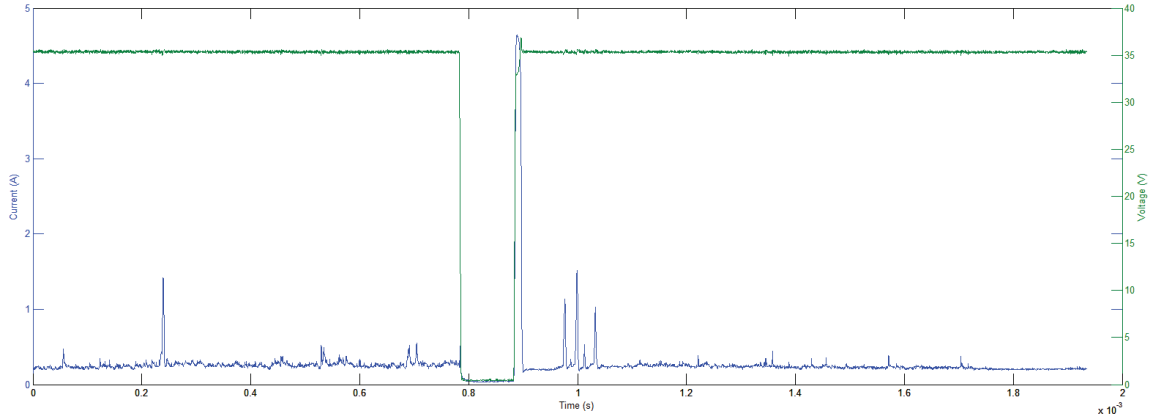


*Figure 50 : I-t characteristics for 26wt% KOH, period=9ms, high-level=35V, low-level=0V, duty cyle=98%. This graphic is a zoom on the region of interest.*

## 8.2 Conclusion

We confirm the result of previous studies made on the use of pulsed voltage in SACE machining ([30], [22], [29], [28], [42] and [43]). The pulsed off-time can act as a cooling time and the use of a pulsed voltage can manage the amount of thermal energy at the machining zone. Another conclusion of those tests is that there an optimum combination of electrical parameters that provide good machining quality. This optimum combination depends strongly on the environment during the machining: type of electrolyte, electrolyte levels, electrolyte flow, nature of the work-piece, tool-electrode runout. Even the geometry of the structure to machine has an influence on the optimum combination of electrical parameters. Therefore, it is complicated to confirm a specific combination, especially if the optimum combination generates a really slow machining.

Regarding the I-t signal analysis. It appears that with a pulse voltage we can have control over the formation and the collapsing of the gas film. This fine control on the gas film dynamics is probably one of the reason why we can have a better machining quality with a pulsed voltage. Also, the low-level do not need to be under the critical voltage to influence the gas film dynamics. There is another phenomenon observable in the I-t signal but not discuss in this chapter: instabilities during the spark regime (Figure 51). Such

instability looks like a superposition of hydrolysis and spark regime; the nature of those would need further investigations.

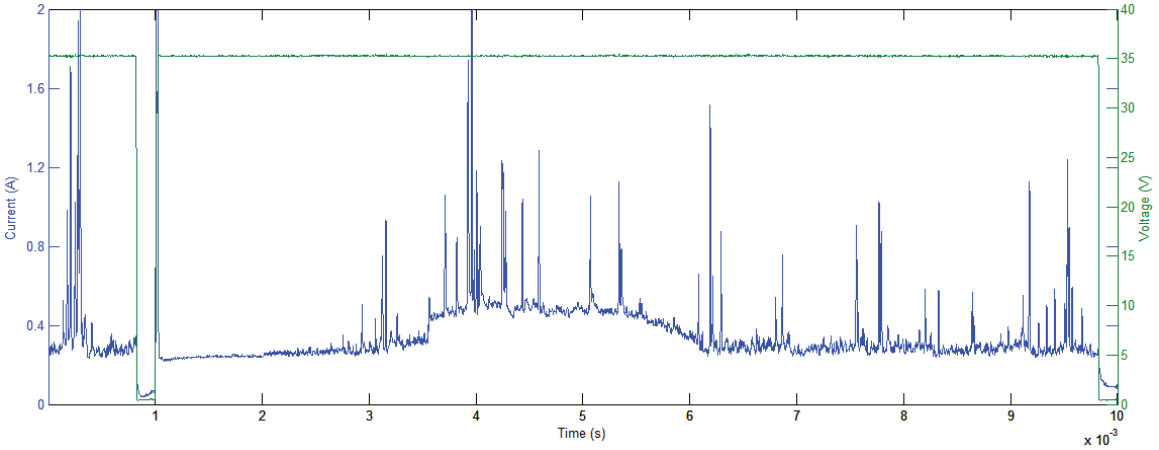


*Figure 51 : I-t curve for 26wt% KOH, high-level=35V, low-level=0V, period=9ms, duty cycle=98%; typical instability present in the I-t signal. This graphic is a zoom on the region of interest.*

# 9 Machining Strategy Improvement

As presented in the previous chapter, it is impossible to avoid all jagged zone or HAZ with the optimization of the electrical input parameters alone. Also, having directly a good machining quality at lower voltage can increase exponentially the machining time. To avoid this increase of machining time and maintain the machining quality, a better machining strategy has to be developed. In this chapter, a method using two different machining steps which allows a faster machining without compromise on the machining quality is presented.

To obtain smooth surfaces a polishing method was developed. The aim is to avoid the need of removing the work-piece from the SACE machine or develop a completely independent technique. Because of that, the post processing has to be done in the processing cell directly after the machining to smooth the edge and clear the surfaces. This avoids alignment problems and additional processing times. Therefore, a method using the tool-electrode as a polishing tool was prioritized.

The strategy is to machine quickly the work-piece at high voltage and high speed (rough machining) and after that reduce the input voltage and repass near the previously machined zone in order to polish the surface. Figure 52 present a schematic view of this method to machine a pillar. In term of the thermos-hydrodynamic approach the idea is to machine roughly at high input energy regardless of the microscopic flow and the HAZ after that, a perfectly control thermal energy input and microscopic flow is used to reduce the HAZ. This strategy allows to machine faster without compromise on the quality. Some parameters can influence the quality of the polishing: the electrical input, the depth of the machined structure, the tool-electrode traveling speed, the number of polishing pass, the polishing depth and the polishing gap. The goal is to find an optimum combination of parameters to obtain the best machined edge quality. Obviously, those polishing parameters are dependent on the quality after the rough machining. Because of that, there is an optimum combination for every specific situation. The goal of this section is to find a pattern for the polishing parameters.

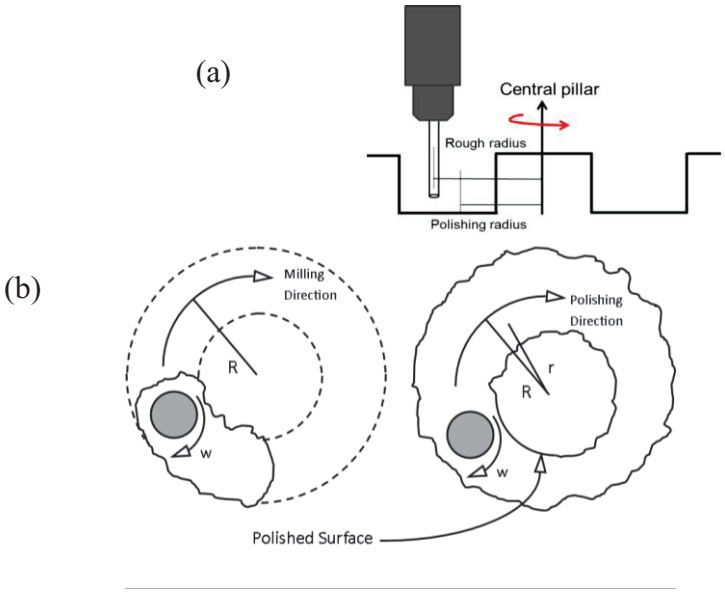


*Figure 52 : Schematic view of the polishing strategy for a pillar machining; (a) profile view (b) top view on the left the rough machining and on the left the polishing.*

## 9.1 Polishing Methodology

Those tests have been performed at Posalux SA (section 3.2) to avoid the influence of the run-out on the pillar circularity. The pillar circularity is one of the indication of a good machining and polishing process. First of all, let us define the parameters which influence the polishing: the polishing gap, the polishing depth, the number of turns. The polishing gap is the difference between the rough machining radius and the polishing radius (polishing gap=R-r). To have more effect on the HAZ, the polishing gap must be smaller than the rough machining radius (more thermal energy on the surface). The goal is to remove a little more material to have smoother surface (suppression of jagged pics). Because we choose to run the polishing at lower voltage we need to reduce the gap between the tool-electrode and the rough surface. The other parameter is the polishing depth which is the tool-electrode depth during the polishing. The polishing depth is kept constant during the polishing. As we will see in the next section the polishing depth does not influence the polishing. Finally, the number of turns (or the number of pass) is the number of circular motion around the pillar during the polishing.

To test this strategy, a series of pillars have been machined (Figure 52). A donut groove shape is machined in the work-piece and the central pillar is polished. Four different pillar heights have been tested: 100µm, 200µm, 300µm and 400µm. Those tests have been made with two different tool-electrodes, one with a 100µm diameter and another with a 200µm diameter. Both tool-electrodes have a bevel of 45º at the tip. Tool-electrode rotational speed was 500rpm. The rough machining is made by several milling cuts of 25µm depth at the time at 200mm/min. For example, to machine a depth of 400µm it is made in 16 circular milling pass. The electrolyte use is a 20wt% NaOH.

The rough machining electrical input chosen is: high-level 38V, low-level 10V, 10ms on-time and 0.1ms off-time. For the polishing the electrical input electrical chosen is: high-level 33V, low-level 27.5V, 1.5ms on-time and 1.5ms off-time. The polishing depth is maintained at 100µm below the workpiece initial surface during all the polishing process. This depth was chosen over another because the goal is to refine the machining edge to remove the HAZ and jagged contour. A tool-electrode positioned at the bottom of the machined channel during the polishing will polish slowly and at the contrary a tool-electrode place near to the edge can create more HAZ. Figure 53(b) shows the general quality of a pillar after the rough machining for two different tool diameter and four different depths. We defined the HAZ length as the maximum variation between a perfectly spherical pillar and the machined pillar (Figure 53 a). Typically, the HAZ is around 100±30µm for a tool-electrode of 100µm diameter and around 75±30µm for a tool-electrode of 200µm diameter. Obviously, those values will change with the electrical input parameters. The difference in the HAZ length is caused by the difference in the machining speed and the heat concentration between the two tool-electrode diameters. The tool-electrode with a 200µm diameter machines more slowly. So with a specific machining speed the 200µm tool-electrode will pass more time around the pillar to achieve a specific depth. This situation allows the process to refine the machined edges. The polishing cannot fully remove all the HAZ but can significantly reduce the HAZ length.

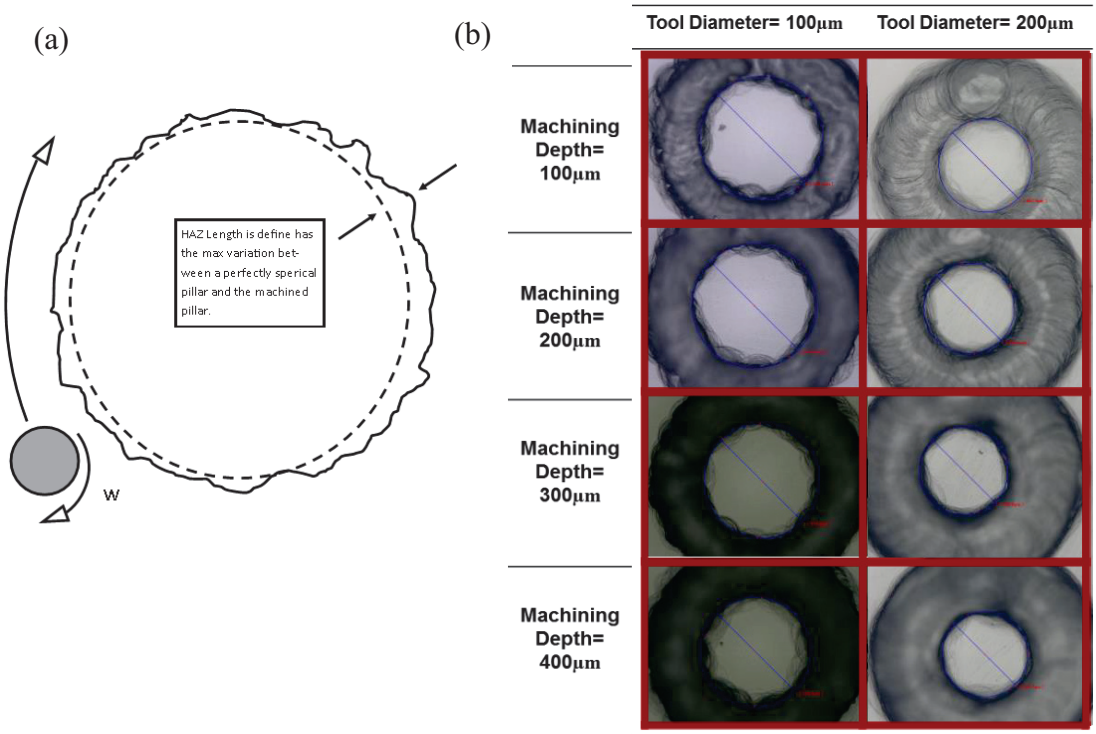


*Figure 53 : Machined pillars after the rough machining, with High-level=38V, Low-level=10V, 10ms on-tims, 0.1ms off-time and a tool rotating speed of 500rpm. We clearly see the HAZ and the Jagged zone.*

## 9.2 Influence Machining Speed

There are the different polishing parameters used for this section:

- Polishing speeds: 20mm/min, 40mm/min and 80mm/min
- Number of polishing turns around the machined pillar: 5, 15 and 20
- Polishing gaps: 60 and 80µm

The polishing gap is the difference between the rough machining radius and the polishing radius R and r respectively in Figure 52. Those parameters have been chosen because after some preliminary tests it appeared that the optimum parameters combination is often in this range. Figure 54 shows an example of results obtained. We clearly see the optimum parameters combination around 15 polishing turns at 20mm/min for a 100µm rough machined depth with r=R-80 and 100µm tool-electrode diameter. As mentioned before, and clearly observable in Figure 54, there is an optimum value where if we decrease

the amount of turn or/and the speed the polishing quality is less good and if we increase the amount of turn or/and the speed the polishing quality also decrease.

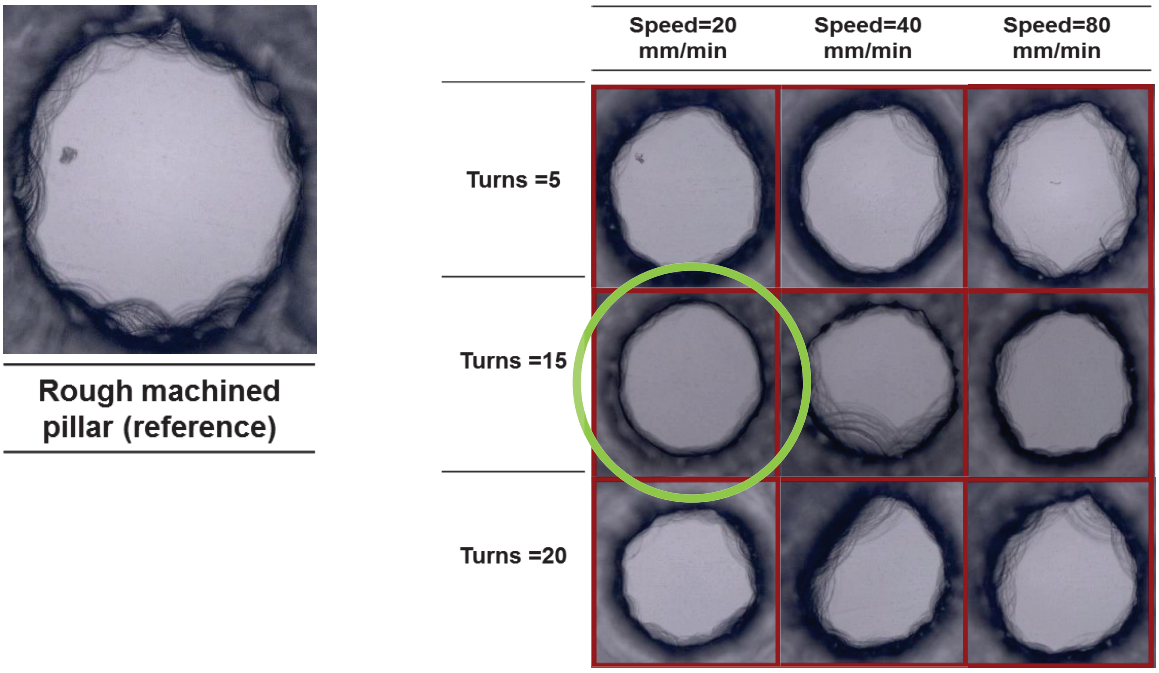


*Figure 54 : Examples of test results for a machining depth of 100µm with r=R-80µm and 100µm tool Ø.*

Table 11 groups all optimum parameters combination for different machining depth and polishing radius. Also, the machining time for a pillar under the different parameter are presented including the rough machining. If we compare those machining times with the machining time of a direct machining for a 150µm depth pillar: 314 seconds. The machining speed of a direct machining is around 0.01mm/s. The optimum parameters combination is the same for a machining depth of 100µm and 200µm. This is probably coming from the same relative electrolyte flushing in the polishing zone for those two pillars heights. An explanation of those result is presented in the next section.

*Table 11 : Optimum parameters combination for different machining depth and polishing radius.*

| 100µm tool Ø | | | | |
|---|---|---|---|---|
| **Polishing radius** | **Depth (µm)** | **Speed (mm/min)** | **Turns** | **Machining Time (s)** |
| **r=R-60** | 100 | 40 | 20 | 84 |
| | 200 | 40 | 20 | 84 |
| | 300 | 40 | 15 | 63 |
| | 400 | 20 | 20 | 167 |
| **r=R-80** | 100 | 20 | 15 | 120 |
| | 200 | 20 | 15 | 120 |
| | 300 | 20 | 20 | 159 |
| | 400 | 40 | 15 | 60 |
| **200µm tool Ø** | | | | |
| **r=R-60** | 100 | 20 | 5 | 42 |
| | 200 | 20 | 5 | 42 |
| | 300 | 80 | 20 | 42 |
| | 400 | 40 | 5 | 22 |
| **r=R-80** | 100 | 40 | 15 | 60 |
| | 200 | 40 | 15 | 60 |
| | 300 | 40 | 15 | 60 |
| | 400 | 10 | 2 | 33 |

## 9.3 Heat Flux During Polishing

In this section we will give an explanation for the polishing optimization results using input energy calculation and I-t signal analysis. We will see that there is a correlation between the heat transfer from the tool-electrode to the machining zone and the optimum combination of parameters. Remember that there is a strong correlation between the energy input and the machining quality (chapter 5.2). Also, chapter 1 proved that the heat dependency is related to the electrolyte flushing and motion at the machining zone. In this analysis we neglected the influence of the $OH^-$ ions production and the chemical etching. Recall that the machining speed and the machining quality are related to the heat exchange between the tool-electrode and the machining zone but also to the OH- ions creation at the tool-electrode surface.

First of all, let us introduce where this observation come from. Figure 55 show the beginning of a hole drilling. The machining was stopped just before the tool-electrode enters in the work-piece. It is clear that the drilling start at the edge of the cylindrical tool-electrode where the heat and the $OH^-$ ions production are the highest. Therefore, the machined zone starts at the tool-electrode edge and propagate in every direction from the edge.

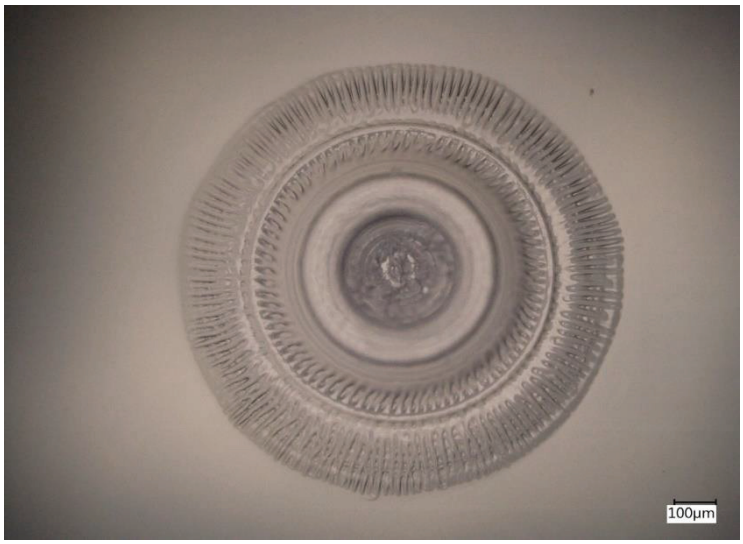


*Figure 55 : Beginning of a hole drilling using a 500µm tool-electrode diameter. The deeper machining circle in the middle has the same diameter than the tool-electrode.*

This fact was investigated and modeled numerically by Jana Abou Ziki [32]. In [32] they develop a model based on the heat diffusion equation where a circular source heats up a semi-infinite work-piece. They solved the equations numerically using ANSYS software and found the machining temperature from it. This study took into account only the beginning of the hole drilling when the microscopic flow is not that relevant.

Using this idea, the polishing strategy is investigated in term of heat transfer from the tool-electrode to the machined surface. The polishing was tested with different tool-electrode travelling speeds and different number of turns around the pillar. A decreasing of the polishing radius resulted in a decreasing of the polishing time to obtain an optimum machining quality. For example, the polishing time for a rough machining depth of 100µm is decreased by about 50% with a difference of polishing gap of 20µm. But for a 200µm tool-electrode diameter this last affirmation is not valid. This comes from the difference in current distribution in function of the tool-electrode diameter. The polishing time can be calculated by this equation:

*Equation 7*

$$Polishing\ time = Turns * Speed * (2\pi r)$$

According to observations of the pillar diameter after the rough machining, the difference between the pillar diameter and the tool-electrode travelling diameter minus the

tool-electrode radius does not change between the tool-electrode of 100µm Ø and the tool of 200µm Ø. In addition to that, during polishing, the tool-electrode is maintained at 100µm below the workpiece initial surface. (Figure 56). Therefore, the effective heat energy transfer from the tool-electrode to a specific point of the work-piece does not change with the tool-electrode diameter. The difference in optimum polishing parameters from a tool-electrode diameter to another can be explained by the difference in energy distribution between the two tool-electrodes and not from the difference in the gap.

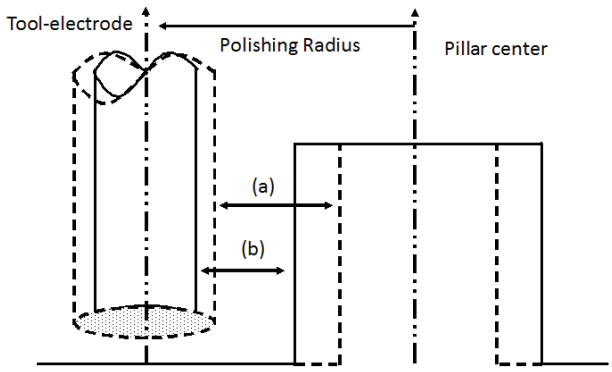


*Figure 56 : Schematic view of the pillar diameter difference for two different tool-electrode diameter. The plane line refer to the machining with the small tool-electrode and the dotted line to the bigger tool-electrode. The increase of the tool-electrode diameter decrease the pillar diameter therefore, the distance (a) and (b) are the same*

The quantity of electrical energy provided to the system is given by the Equation 8 (as mentioned in chapter 0 only 2-6% of this energy is provided to the work-piece).

*Equation 8*

$$W_{tot} \propto \Delta V \cdot I \cdot t$$

For the studied case, because a pulsed voltage is used, Equation 8 becomes Equation 9 for polishing:

*Equation 9*

$$W_{tot} \propto \frac{2\pi r(Turns \cdot Speed)}{(t_{Hilevel} + t_{Lolevel})}(\Delta V_{Hilevel} \cdot I_{Hilevel} \cdot t_{Hilevel} + \Delta V_{Lolevel} \cdot I_{Lolevel} \cdot t_{Lolevel})$$

Because the input voltage is the same for every tests, the electrical variable in the equation is constant and Equation 9 can be simplified to:

*Equation 10*

$$W_{tot} \propto Turns \cdot Speed$$

Thus the total energy divide by the machining time and pillar circumference gives an approximation of the quantity of energy given to a specific location of the machined work-piece during the polishing. It appears that this quantity is constant for every set of optimum polishing parameters combinations. Those quantities are around $1.1x10^{-8}$ W/(s*rad) for a polishing radius of r=R-60µm and $2.8x10^{-9}$ W/(s*rad) for a polishing radius of r=R-80µm. Those values do not depend on the polishing depth or the tool-electrode radius. Therefore, to obtain a good surface polishing the important parameter to observe is the energy quantity input by unit of time and distance. This energy input in the system is proportional to the number of turns and the travelling speed. So, there is a correlation between the optimum parameters combination and a specific energy input. Obviously, if we change the polishing input voltage the optimum parameters combination will change, because of the variation of input energy and in the same way if we change the machined pattern will also change the optimum parameters combination.

On the other hand, as presented before, the polishing capability is also related to the electrolyte motion around the machining zone. This can explain the observed differences between the pillars of different heights. Another example of this affirmation is that the pillar shape dependencies with the electrolyte flow. As presented in (section 3.2) the set-up of Posalux SA is equipped with an electrolyte nozzle. The pillar shape is depending on the relative position between the electrolyte nozzle and the machined pillar (Figure 33).

## 9.4 Conclusion

The afterward polishing can improve significantly the machining quality without increasing the machining time. To have a good machining with only one pass the machining speed has to be 0.01mm/s. Therefore, with this strategy we can increase the machining speed by about 75%. This machining strategy can be a solution to the recurring dilemma which we have to choose between the machining quality and the machining time. As presented in the chapter 9.2 the polishing influence is linked to the quantity of input energy at the machining zone.

# 10 Conclusion of Thermo-Hydrodynamic Part

In this part we clearly see the great influence of the thermo-hydrodynamic in the SACE process. The combinations of bulk flow, microscopic flow and thermal energy input have a significant influence on the machining speed and on the machining quality. It appears that a too high electrolyte flushing will lead to a slow machining and at the contrary a too low electrolyte flushing will lead to a poor quality. This fact can be explained this way: the electrolyte flushing determines the heat and ion distribution at the machining zone. The ions distributions have not been discussed all over this part but remember that the SACE process is not just a pure thermal process, it is also a chemical based process. This component of the process is hidden in the discussion. If we remove a part of the thermal energy via the flushing, we also remove a part of the $OH^-$ ions created at the vicinity of the tool-electrode and we also remove reaction sub-products. Those sub-products can slow down the process. The intimate link between the chemical species distribution, the heat distribution and the electrolyte flow still needs to be found (Figure 57).

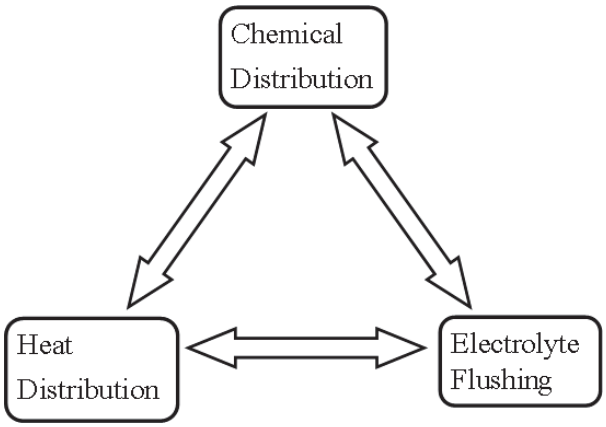


*Figure 57 : link between the Chemical species distribution, the heat distribution and the electrolyte flow*

However, some observations made in this part can lead to a better understanding of the SACE process and a model which can predict the outcome of machining. Those observations are:

- Increasing of the bulk flow can increase the microscopic flow, specially during drilling.
- there is an optimum combination of electrical parameter which provide good machining quality. This optimum combination depends strongly on the environment during the machining: type of electrolyte, electrolyte level, electrolyte flow, nature of the work-piece, tool-electrode runout. Even the geometry of the structure to machine has an influence on optimum combination of electrical parameter.
- If we machined at higher input voltage, we have to increase the bulk flow to dissipate the additional heat from the machining zone and prevent HAZ.
- The use of a pulsed voltage leads to a control over the formation and the collapsing of the gas film. This fine control on the gas film dynamics is probably one of the reason why we can have a better machining quality with a pulsed voltage.
- Tool-electrode rotation increases the microscopic flow.
- A shaped tool-electrode increases the drilling speed by increasing the microscopic flow.
- The machining speed and machining quality can be improving by the use of a machining strategy incorporating a polishing.

# PART III: Spectroscopic Approach

# 11 Spectroscopic Analysis

SACE technology such as presented before (section 1.1) and discussed all over this document is based on the formation of electrochemical discharges in alkaline electrolytes. The cathode surface is much smaller than the anode in order to allow the formation of a gas film and the generation of electrical discharges. Machining is due to the local thermally-assisted chemical etching of the glass work-piece induce by the electrical discharges. This chapter focus on the analysis of those discharges (plasma discharge). In SACE literature this phenomenon is often call cathodic contact glow discharge electrolysis but as we can tell this designation is not totally valid. If we observe the current-voltage plot for a system, such the SACE (Figure 58) we can more likely understand the type of discharge occurring [45], the current-voltage plot is typical of spark discharges plasma. If we increase the voltage at the beginning, we observed the ohmic region characterized by the water hydrolysis followed by an unstable region where random electrical discharges occur (Spark discharge). This unstable region is the operating region of the SACE process (Figure 58(a)). This unstable region is followed by a stable region where the flow of bubbles from the tool-electrode surface ceased and smooth dark sheath of vapour occurs (Figure 58(b)) [45].

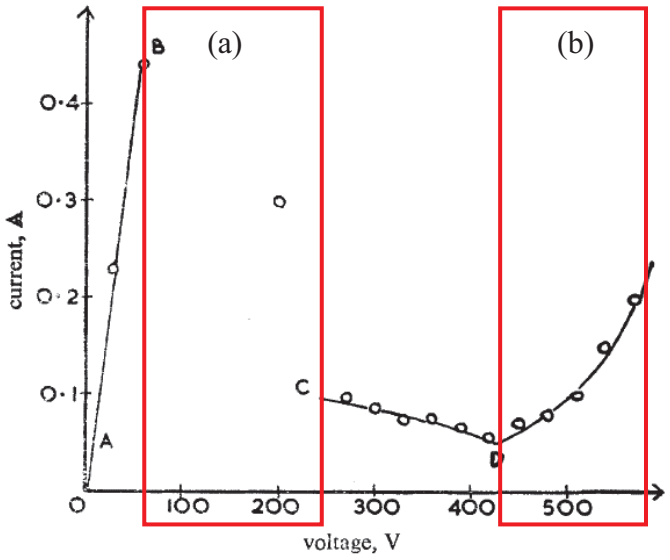


*Figure 58 : Characteristic current-voltage plot. Data obtain for a 0.05M $Na_2HPO_4$ electrolyte with a platinum tool-electrode in anodic polarization. Not down the voltage range is wider than for the SACE. (a) operating region of the SACE process characterize by unstable discharge (b) contact glow-discharge operating range. use with the authorization of Journal Journal of Electroanalytic Chemistry* [45].

Therefore, the actual designation of the plasma emission during the SACE process is not accurate. The type of plasma discharge occurring in SACE is called spark discharges or filament discharges. Those discharges generate light emission form the de-excitation process of chemical species present in the gas film. Despite all publications about SACE machining and its great potential, the underlying plasma physics driving the process remains not fully understood and discussed (for this technology). A better understanding of the plasma physics being SACE can lead to totally new approach and comprehension of the process.

Thereby, in collaboration with Dr. Luc Stafford from the Université de Montréal, Département de physique, the light emission of spark discharges during SACE machining was investigated. Dr. Stafford provided the spectrometer and expertise to analyze the spark discharges. More specifically in the present work, optical emission spectroscopy (OES) is used to observe the plasma-generated species during the SACE process. It appears the light emission of the plasma come mainly from the metallic ions species present in the gas film: Na I and K I. The Boltzmann plots constructed from Na-I and K-I lines showed linear trends, suggesting a thermal equilibrium between these excited

states. The excitation temperature $T_{exc}$ extracted from those plots remained fairly constant (0.35 to 0.55eV) with variations of the duty cycle and/or the lower-level voltage. Similar values were obtained for all pulse durations and for both electrolyte solutions. Emission from OH(305nm)→OH(320nm) system was also analyzed using the Specair software. The rotational temperature deduced from such plots varied from 1000K to 1500K depending on the range of experimental conditions.

## 11.1 Current understanding of spark discharges in liquid

Let us introduce previous studies made on this fields. Plasma production in a liquid become a key element for application such as water peroxide production [46], electrical-discharges sterilization of water, surface treatment or nano and micro particles production [47]. Studies use different type of liquid, conductive or not. In our system a conductive liquid is used (electrolyte). Hickling and Ingram [48] are one of the first to rediscover the so called contact glow discharge electrolysis, known in fact since 1844. They physically analyse the phenomenon and highlighted some important aspects of it. According to their work in such systems most of the chemical reactions occur in the liquid phase and do not depend on the gas nature around the electrode. Also, they note the cathodic polarization (SACE) is less stable than the anodic polarization. This can be explaining by the fact in cathodic polarization most of the heat is removed through the tool-electrode and do not take part in the gas film stabilisation. Graham and Stalker [47] provide an overview of the actual understanding of the plasma in liquid physic in system similar to the SACE. Plasma in a liquid and vapor system if often at non-equilibrium (i.e. that the electronic temperature is far from the ionic temperature). Also, the plasma in such system evolves in a relatively high pressure, compared to a pure gas environment (discharge tube). For a cathodic polarization the plasma process which operates the electron emission from an active electrode throw a gas film is call thermionic emission. A study made by Allagui [49] show some characteristics of cathodic contact glow discharge electrolysis in a system similar to SACE processing cell. He gives information about the discharge characteristics. The

spatial dimension of the discharges is about ten micrometers with a cross-section of 0.01 to 1.35 $mm^2$, evaluated from high speed imaging.

Regarding the plasma composition, as presented by [49] and [50], the plasma in a liquid solution differs from standard gas plasma because major portion of the radiation is due to species present in the electrolyte (alkaline metal species present in the solution). The authors qualify this type of emission by *nonequilibrium system*. They used an electrolytic cell as presented in section 3.4 with a platinum tool-electrode submerged in a 5 mol/L KOH electrolyte. Also, they pointed out that the nature of the plasma emission comes mostly from K I, $H_\alpha$, $H_\beta$, $H_\gamma$ and $OH^-$ band. In [51] the H emission at 656.3nm and 486.1nm, O emission at 777.1nm and the $OH^-$ band emission around 600nm (second diffraction order of the spectrometer) is also observed. In addition to that, [51] investigated the intensity of the emission spectra. Under a DC voltage the emission is higher when the tool-electrode is smaller and when the solution concentration is higher. As the cell terminal voltage is increased, the intensity of the emission peaks increases and at the same time the background of the emission spectrum increases significantly. On the other hand, the line intensity evolution with the cell terminal voltage do not follow the same trend for each lines. Maksimov [50] also investigate the basic physical, physicochemical and chemical processes in plasma-solution systems. Maksimov used electrolyte based on NaCl, KCl and $BaCl_2$ salts. They suggest that the gas temperature is around 1500-1600K for plasma under cathode effect. This was measured by using the intensity distribution in the unresolved rotational structure of molecular nitrogen and $OH^-$ radical bands.

## 11.2 Experimental Set-up

The OES spectrometer used for this study is a PI ACTON SP2300 form Princeton Instruments. This spectrometer collects the light via an optical fiber. Because of the relatively low emission intensity of the SACE process for spectroscopic analysis, the set-up needed to be scaled down. The light intensity captured by the spectrometer depends on the distance between the optical fiber and the tool-electrode tip. The processing cell was replaced by a quartz beaker to avoid wavelength absorption by the container and allow

smaller distance between the optical fiber and the tool-electrode tip (Figure 59(a)). To align the optical fiber and the tool-electrode both are put on separate micrometer stages. This allows to maximize the light intensity collection. To help the alignment between the tool-electrode tip and the spectrometer optical fiber, a red laser diode was used. The tool-electrode used for those tests is a 250µm stainless steel rod. This tool-electrode diameter was prioritized over larger tool-electrode diameters because the density of light emission from a small tool-electrode is higher than for a larger tool-electrode. For every test 2mm of the tool-electrode was dipped into to the electrolyte.

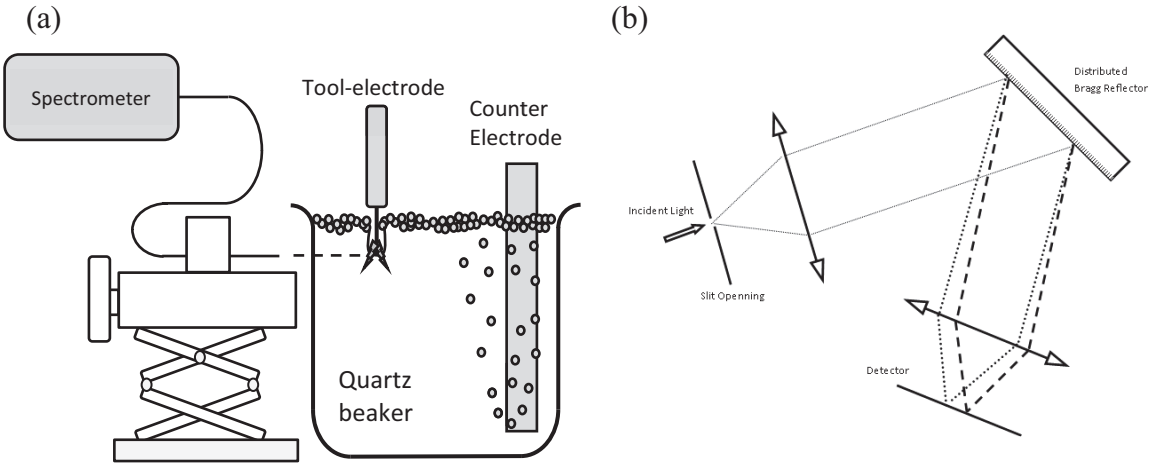


*Figure 59 : (a) Schematic view of the set up use for spectroscopic test (b) Schematic view of the spectrometer internal. The production of gas which can blind the optical fiber is represented.*

Regarding the input parameter: two main electrolytes were used: 20wt% NaOH and 26wt% KOH. The plasma was sustained in an electrolyte at room-temperature by applying pulsed voltage on the cathode. Measurements were carried out with pulse durations of 1, 2 and 5ms with duty cycles between 20 and 80%. In all cases, the high-level was fixed at 38V, while the lower lever was set at either 7, 19 or 30V. This constant value of high-level is imposed by the constraint to have enough light emission to allow its detection by the spectrometer. Typical current and voltage as a function of the time measurements are presented in Figure 60(a) and (b). That information taken via an oscilloscope are related to the light emission in further section. In all cases, a spark-mode is observed with typical filament patterns. Regardless the low-level, most of the sparks discharges occur during the high-time. In Figure 60(a), the larger current peak, just at the beginning of the high-level

refer to the gas film formation. In Figure 60(a) during the low-level there are no sparks because the low-level is under the critical voltage, resulting in simple hydrolysis. Even if the low-level is higher than the critical voltage (Figure 60(b)), there is no significant discharges during the low-level. This is because the variation in the voltage affects the gas film dynamics (chapter 8.1). Because of the voltage variation the gas film completely collapse. In Figure 60(b), during the high-level phase, some gas film formations and destructions can be observed.

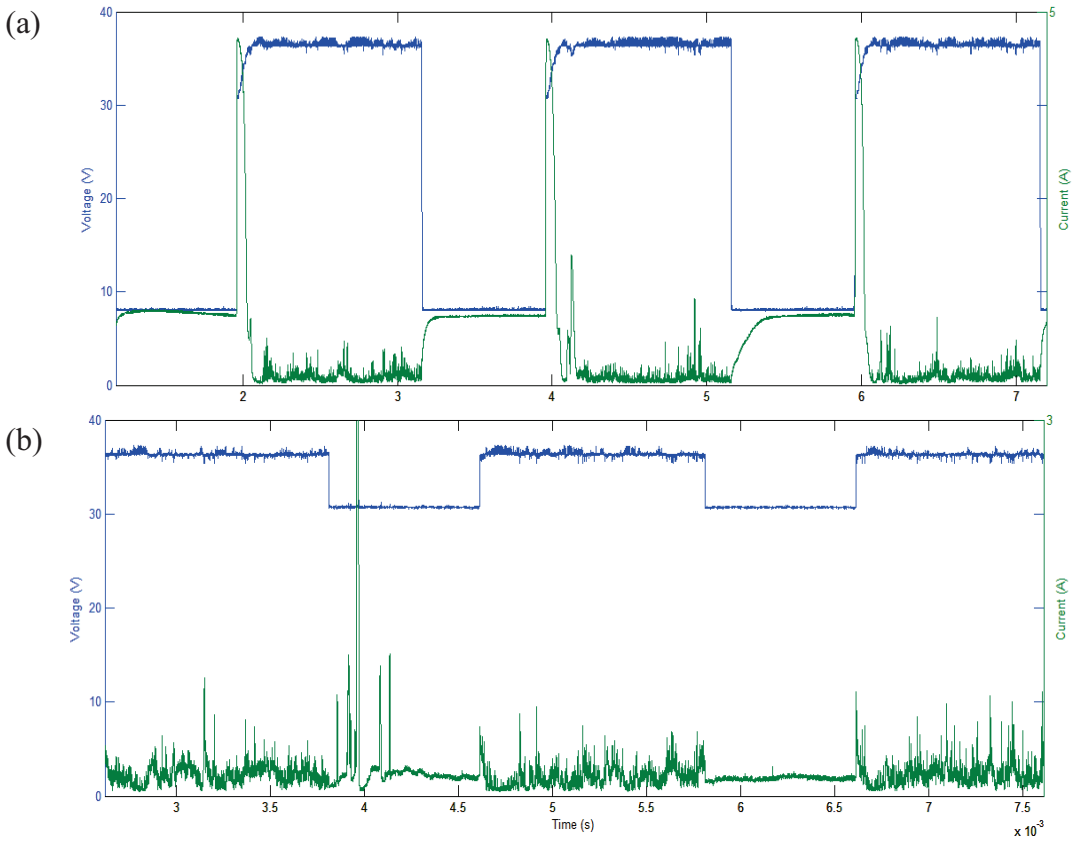


*Figure 60 : Typical current signal in 26wt% KOH for: (a) 2ms period, 38V high-level, 7V low-level and 60% duty cycle (b) 2ms period, 38V high-level, 30V low-level and 60% duty cycle.*

More information about the spectrometer setting. Because of the spark discharges intrinsic nature it is not possible to synchronise the plasma emission and the spectrometer. The gas film dynamics and the spark discharges are too fast and random to synchronise with the spectrometer. Hence, all the monitored intensities in this studies are time-averaged OES values. The spectrometer is equipped with a 300 mm focal length monochromator and

a 1200 lines/mm grating blazed in the visible range. Emission intensities were recorded using a Pixis 256E charged-coupled device camera. The light emission is focused via a slit opening and separated by a diffraction grating (Figure 59(b)). The slit opening was set on 20 μm, with a spectral resolution (full width at half maximum) of about 0.2 nm at 811 nm. To have comparable data, those spectrometer values were kept unchanged for all measurements. The scanning wavelength range is 300 to 900nm. Lastly, the only variable between each test is the integration time: 1 second, 30 seconds and 200 seconds. The exposure time needed to be adjusted due to the wide range of emission intensities (some lines needed more acquisition time than others). The exposure time was adjusted during the data processing to have comparable data. Also, the production of gas at the electrodes surface tend to blurry the electrolyte and avoid the light collection. Because of that we have to wait between each data acquisition to clear the electrolyte.

## 11.3 Results and Discussions

### *11.3.1 Global analysis of emission spectra*

Typical emission spectra of 20wt% NaOH and 26wt% KOH electrolytes are presented in Figure 61(a) NaOH and (b) KOH. For comparisons purpose the intensity was normalized to one (note the logarithm axis). As discussed previously, emissions spectra give information about the composition of the spark discharges. As expected from previous work ([49] and [50]) OES revealed lines from either Na-I {330.3, 588.9, 589.6, 818.3, and 819.5nm} or K-I {404.8, 691.1, 693.8, 766.5, and 769.9nm}. In additional to that, emission from H I, O I, and OH (A-X) were also found.

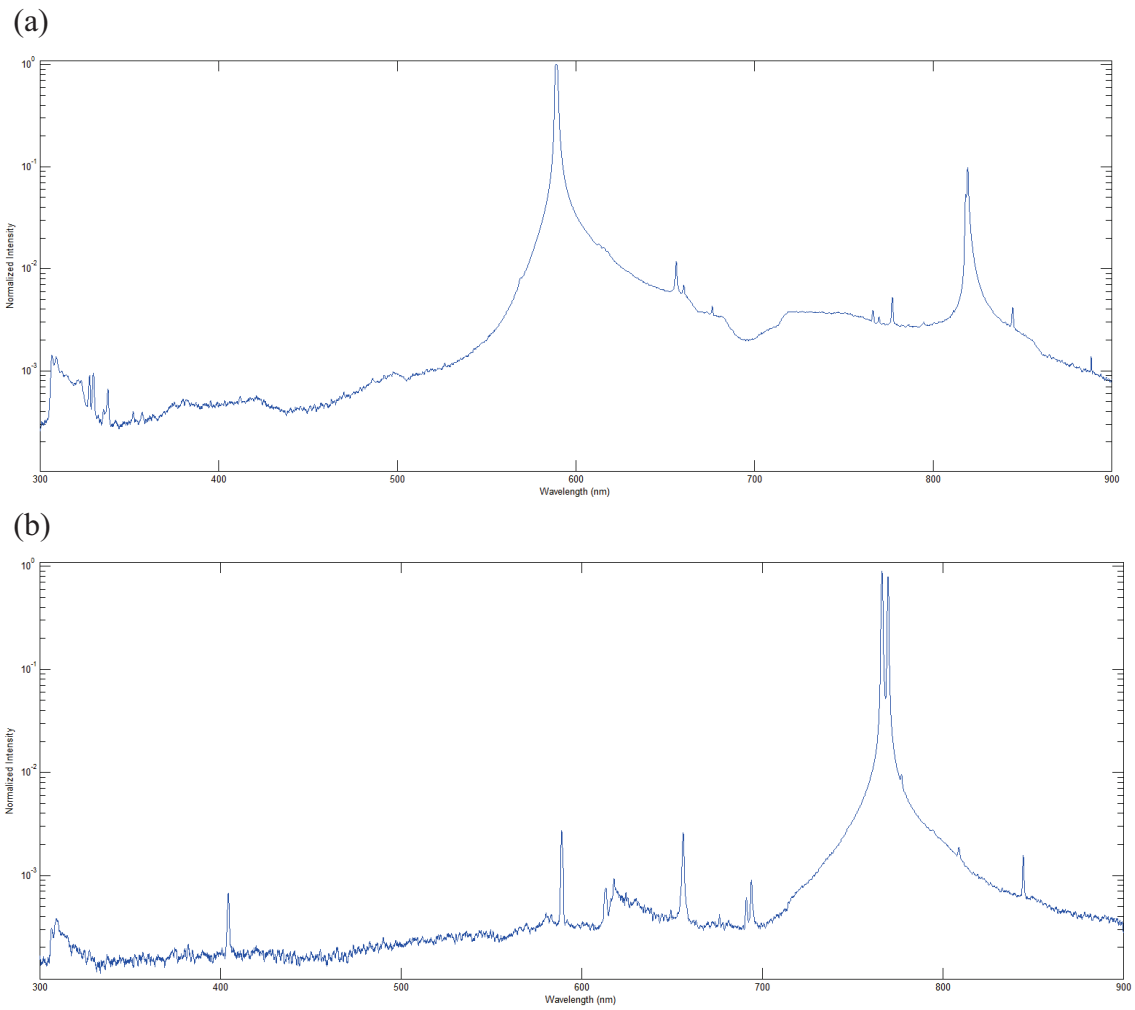


*Figure 61 : Typical emission spectrum from SACE machining at 38V DC, exposure time at 90seconds; (a) with 20wt% NaOH and (b) with 26wt% KOH; the spectrometer integration time was set to 5 seconds for both*

Table 12 present the spectral lines visible during SACE machining for a NaOH based electrolyte and a KOH based electrolyte. Table 12 also gives physical constant used for the determination of the plasma excitation temperature by the Boltzmann plot in a further section (section 11.3.4). The Na I and K I ions come from the electrolyte itself but the O I and $H_\alpha$ are produces by reactions at the tool-electrode surface. In the case of OH band there is a quantity proportional to the electrolyte concentration naturally present in the electrolyte but also a quantity produced at the tool-electrode surface.

*Table 12 : Visible spectral lines during SACE machining with NaOH based electrolyte and KOH based electrolyte. Those position are taken from the spectrum 38V DC. $A_{ij}$ correspond to the Einstein coefficient, $g_i$ the degeneracy of the upper level and the excitation energy.*

| Emission Raie (nm) | Ions or molecule | $A_{ij}$ ($10^6$ $s^{-1}$) | $g_j$ | $\varepsilon_{ij}$ (eV) |
|---|---|---|---|---|
| **NaOH Based Electrolyte** | | | | |
| **303-325** | OH | - | - | - |
| **330.2** | Na I | 5.5 | 6 | 3.75 |
| **407.5** | - | - | - | - |
| **589.3** | Na I | 61.2 | 4 | 2.104 |
| **589.8** | Na I | 61.4 | 2 | 2.102 |
| **656.5** | $H_\alpha$ | - | - | - |
| **777.3** | O I | - | - | - |
| **818.3** | Na I | 42.9 | 4 | 3.616 |
| **819.6** | Na I | 51.4 | 6 | 3.616 |
| **844.8** | O I | - | - | - |
| KOH Based Electrolyte | | | | |
| **303-325** | OH | - | - | - |
| **404.4** | K I | 1.07 | 2 | 3.06 |
| **656.5** | $H_\alpha$ | - | - | - |
| **691.0** | K I | 2.72 | 2 | 3.404 |
| **693.0** | K I | 3.9 | 2 | 3.404 |
| **777.3** | O I | - | - | - |
| **766.5** | K I | 38 | 4 | 1.62 |
| **769.9** | K I | 37.5 | 2 | 1.61 |
| **844.8** | O I | - | - | - |

### *11.3.2 Detailed analysis of Na and K lines*

If we compare the Na I and K I mains spectral emission from the plasma discharges to standard low pressure discharge tubes a shift of the wavelength position is observed (Figure 62(a) and (b)). Note the spectral lines position from the low-pressure discharge tube was taken with the same spectrometer and set-up. Thereafter, the wavelength position of discharge tubes and the SACE plasma:

- Na main lines: discharge tube {588.995 and 589.968nm} and spark discharges {589.3 and 589.8nm}.
- K main lines: discharge tube {766.745 and 770.186nm} and spark discharges {766.5 and 770.9nm}.

Therefore, a wavelength shifts of 0.21 ± 0.07nm is observed for Na I main lines and a shift of 0.25 ± 0.10nm is observed for K I main lines. Those shifts are constant for all electrical conditions. This shift can be explained by the Stark shift. Such shifts are generally not observed in plasmas sustained in a pure gas environment (discharge tube). Over the range of experimental conditions examined, this suggests the presence of very string electric fields very close to the electrode region.

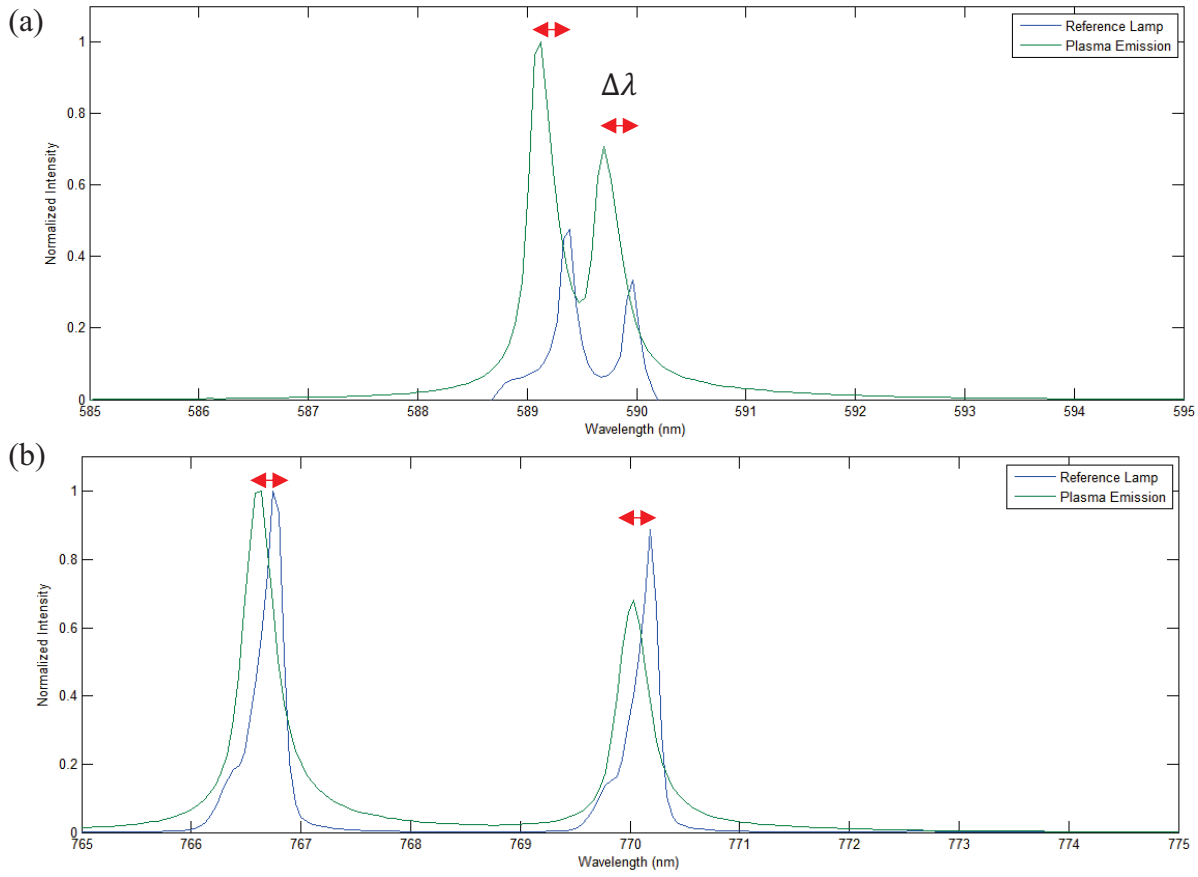


*Figure 62 : OES comparison between the low-pressure lamp and the plasma emission of the two main line (a) for sodium emission and (b) for potassium emission. The Δλ represent the shift in wavelength.*

### *11.3.3 Correlation between emission and current analysis*

Emission lines intensity are affected by the current density. If we drop the voltage the light intensity drops also. But, after some tests, the light emission does not seem to be directly affected by other electrical parameter such as the duty cycle, the period or the low-level. However, if we compare the light emission to the average current we found a trend. The light emission as a function of the average current follows an exponentially decreasing trend (Figure 63(a)-(d)). The average current for this section is taken from experimental data using the set-up presented in section 3.4. The average current can be calculated in three different ways:

- *Total Average Current*: is the average current taken over all the electrical period (ΣCurrent/period). This average current, as the three other averages, is evaluated from multiple period to have a better statistics.
- *High Average Current*: The high average current is the average current only during the high-time. Therefore, the low-level part of the period is not considered.
- *Low Average Current*: The low average current is the average current only during the low-time. Therefore, the high-level part of the period is not considered.

After some observations the most significant correlation observed is between the light intensity and the high average current (Figure 63(a) - (d)). Also, there is no correlation between the light emission and the low average current. This is expected as light emission occurs mostly during the high-level (Figure 60). Figure 63(a) - (d) shows the integrated line emission as a function of the average high-level current for two emission lines of Na I (a)-(b) 20wt% NaOH and K I (c)-(d) 26wt% KOH. Note, those emission lines were chosen randomly over the spectrum and similar trend is observed with the other lines.

Therefore, we have an inverse exponential trend with respect to the average high current. Consequently, higher the current is during the high-level less spark discharges are present. This was observed from the analysis of the i-t signal but seems to be confirmed by the spectroscopic analysis.

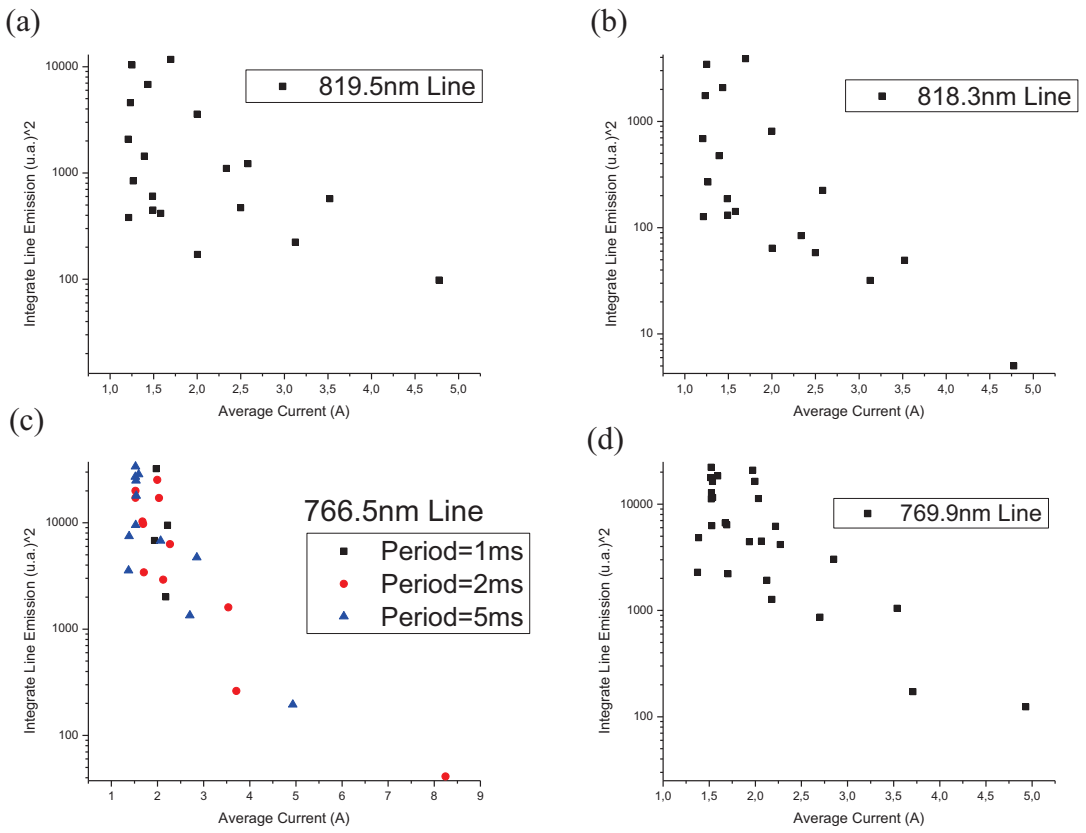


*Figure 63 : Integrate line emission intensities as a function of the average high-level current for a specific emission line(a)-(b) 20wt% NaOH (c)-(d) 26wt% KOH, note down those emission line was chosen randomly over the spectrum and similar trend is observed with other lines.*

This trend can be explained by the gas film formation time during the on-time. When the high-level is applied in the first milliseconds, the gas film is created. As presented in **Erreur ! Source du renvoi introuvable.**, signals with a lower low-level have higher current density and thus combine with a lower light emission. In fact, a signal with a lower low-level leads to a longer gas film formation time during on-time such that the quantity of gas required to cover the tool-electrode is higher. Therefore, the increase of the average current with a lower low-level is not due to the increase in the number of spark discharges. As mentioned above, similar trend with the average current were observed for the other emission intensities (other than Na and K). This is illustrated in (Figure 64) for OH in either NaOH or KOH solutions. However, by taking the ratio of Na/OH and K/OH emission intensities, the values become constant, (Figure 65) independent of the average current. This indicates that most of the Na, K and OH vapors result from the gas film formation

(OH radicals and metallic Na or K have similar vapor formation dynamics) and not so much from the discharge ↔ tool-electrode interactions.

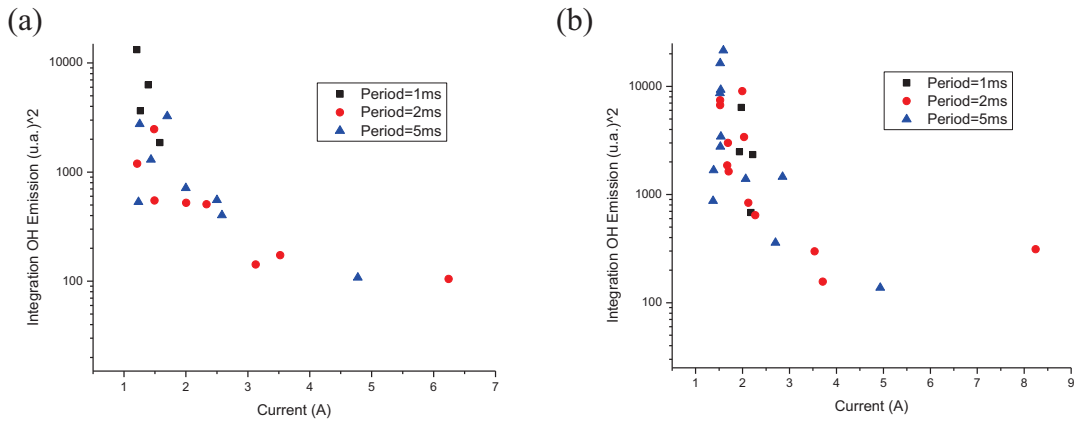


*Figure 64 : OH emission Band intensity as a function of the high-level average current (discharge current) for (a) 20wt% NaOH (b) 26wt% KOH.*

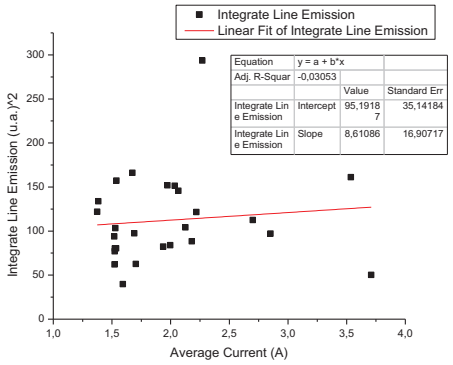


*Figure 65 : K line 7666.5nm / OH emission Band intensity as a function of the high-level average current (discharge current).*

### *11.3.4 Boltzmann Plot and Excitation temperature analysis*

The heat energy transferred to the machining zone, as showed before, is linked to the machining speed and the machined surface quality. Plasma temperatures (several temperatures in non-equilibrium plasmas) can provide information about the heat quantity provided to the electrolyte and the work-piece during SACE. After a spark discharge, the heat generated by the plasma diffuses in the gas film and in the electrolyte around the tool-electrode. The authors in [50], by using a similar system, found spark temperatures around

1500-1600K. Two different ways to obtain temperatures are used in this study: the Boltzmann plot using Na and K lines and the $OH^-$ band fitting. This section focus on the Boltzmann plot.

Assuming that the pressure inside the spark discharge is high enough to ensure significant interactions between Na excited states for NaOH-based discharges and K excited states for KOH-based discharges, the population of these states is expected to follow a Boltzmann distribution characterized by an excitation temperature $T_e$. In such system, a Boltzmann plot can be constructed using the following equation [53]:

*Equation 11*

$$f(E_{nm}) \propto e^{-E_{nm}/K_B T_e} \rightarrow ln\left(\frac{I_{nm}\lambda_{nm}}{gf}\right) = -\frac{E_{nm}}{k_B T_e}$$

With the following balanced system under thermodynamic equilibrium:

*Equation 12*

$$X + A_p + (E_{nm}) \leftrightarrow X + A_q$$
$$deexcitation \leftrightarrow excitation$$

Where $I_{nm}$ is the Na or K line intensity, $\lambda_{nm}$ is the wavelength, g is the statistic weight of the lower level (**Erreur ! Source du renvoi introuvable.**), f is the oscillator strength, $E_{nm}$ is the energy of the upper level and finally $k_B$ is the Boltzmann constant. The temperature is in electronvolts. Figure 66 shows a typical Boltzmann plot obtained from SACE plasma emission. More specifically in 26wt% KOH electrolyte.

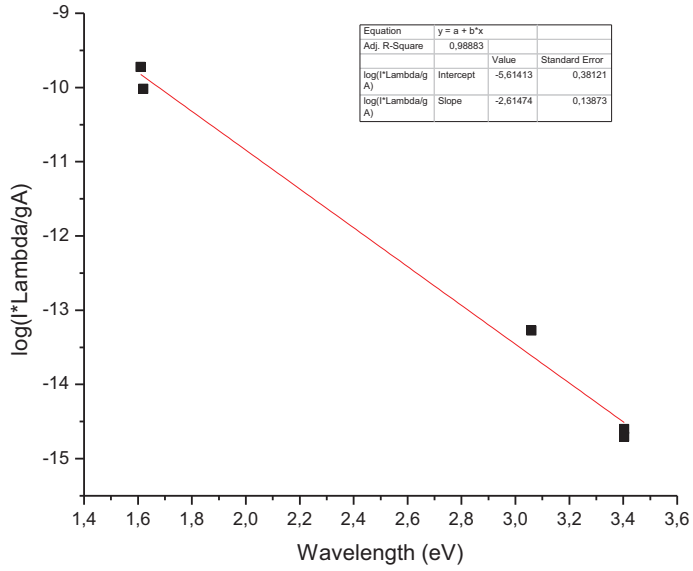


*Figure 66 : Boltzmann plot for 26wt% KOH with: 5ms period, 38V high-level, 7V low-level, 80% duty cycle.*

Boltzmann plots were constructed using Na-I and K-I lines for all parameters tested. A linear trend was observed on semi-log plots for every parameter conforming Boltzmann distribution for these excited states. The excitation temperature found are for Na I: 5400 ± 1200 K and for K I: 4500 ± 850 K. No correlation between the excitation temperature and the electrical input could be observed. This suggests that the spark properties leading the corresponding excitation temperatures are independent of the operating conditions. This feature is consistent with the similar shifts for Na I and K I lines ascribed to comparable electric field across the spark region very close to the electrode surface. If we compare those temperatures with the tool-electrode temperature (around 600ºC), the excitation temperature measured seems to be realistic: the machining temperature is obviously lower than the spark temperature.

### *11.3.5 OH rovibrational structure and rotational temperature*

As shown in Figure 61, optical emission spectra mostly contained emission lines ascribed to spontaneous radiative de-excitation reactions of K, Na, H and O atoms. A much wider emission could also be seen between 305 and 325nm. This wide band can be ascribed

to the rovibrational structure of OH (A-X transitions). This emission was fitted using the software Specair with the rotational temperature as the only adjustable parameter (Figure 67 (a) and (b)). Because of the relatively low emission of the OH band in the NaOH-based electrolyte, only the KOH-based electrolyte was analyzed. Over the range of experimental conditions investigated, the rotational temperature was between 1000-1500K. These values are comparable to those obtained by Maksimov [50]. They are none the less lower than the excitation temperatures deduced from the Boltzmann plots, this confirms the out-of-equilibrium nature of spark discharges produced in electrolyte liquids.

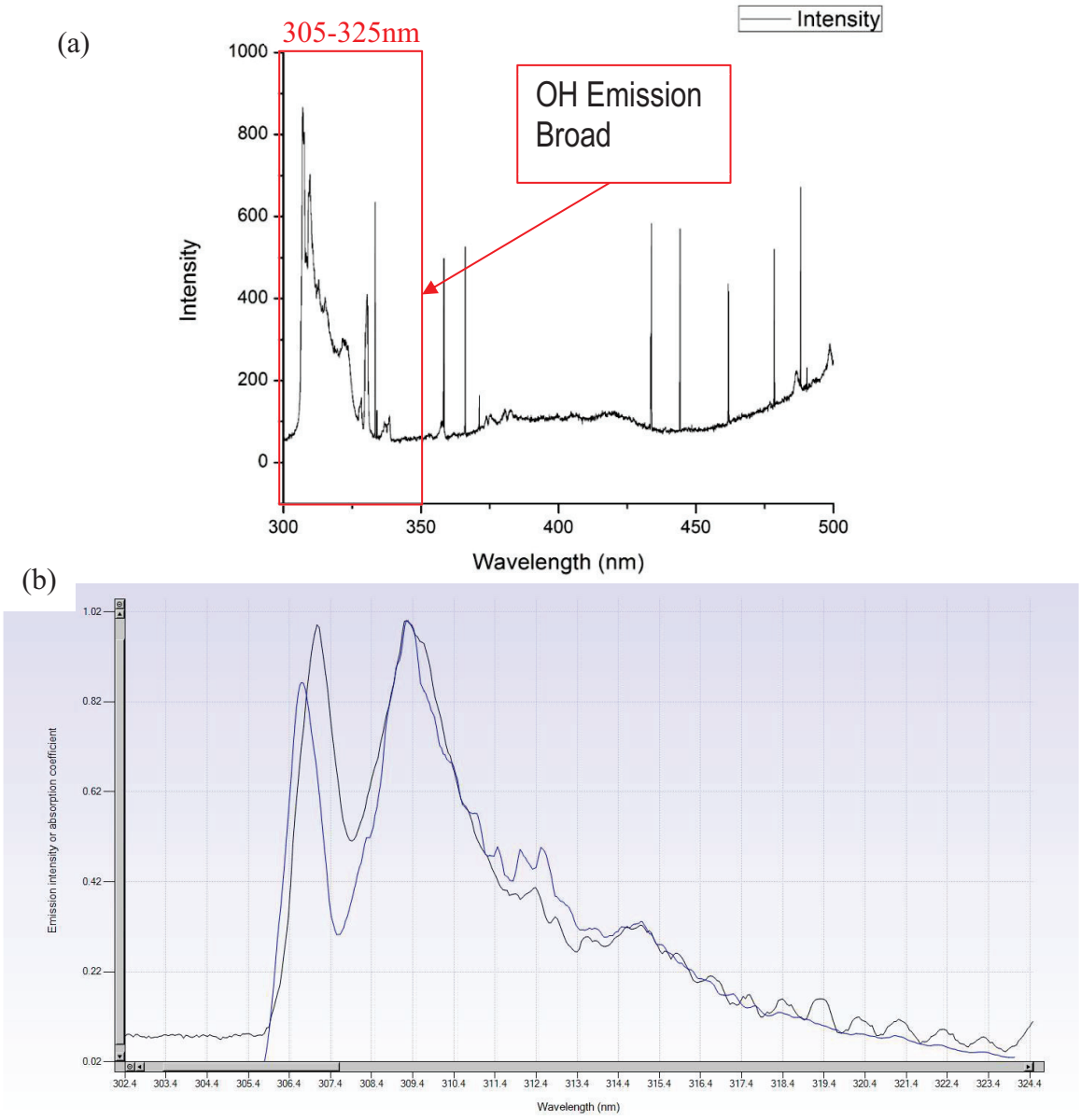


*Figure 67 : Typical OH emission spectrum (38V DC, 20wt% NaOH, Exposure time 90 seconds)*

# 12 SACE Applications

This section reports some tests made to prove the viability of SACE process in an industrial environment. It is important to test the SACE capability in an industrial environment to show the full potential of this micromachining technology. Those tests are based on the current industrial need for Micro-Electro Mechanical Systems (MEMS), microfluidics, electronic and opto-electronic applications. Key applications targeted are: glass-to-glass bonding and the Gorilla-glass machining.

## 12.1 Glass-to-glass Bonding

Material bonding is a key technology for material integration in Micro-Electro-Mechanical Systems (MEMS), optoelectronics and microfluidics devices [54], [55]. Bonding establish a hermetic protection against external influences and provide mechanical toughness to the device. Bonding is as well needed in the fabrication of multi-layer devices [54]. One of the three key base materials in microfluidic and MEMS device is the glass [56], the other two are polymers and silicon. Glass has several advantages for those applications such as chemically inertness, well-known surface chemistry, biocompatibility, excellent mechanical properties and thermal resistance for applications where plastic base material cannot provide enough thermal resistance or transparency for the application.

Glass-to-glass bonding can be a challenge in the fabrication of microfluidic devices. In glass based devices the machining can induce HAZ, bulge, or deposit debris on the surface [57], [58]. Those defects can avoid glass-to-glass bonding. If the device is fabricated by microelectronic derived technics there is no problem, but if we use more flexible technics, such as laser engraving, glass-to-glass bonding is not so obvious because of the creation of the bulge and material deposition during the process. In [59] the authors propose a list of requirements for an efficient glass-to-glass bonding. Firstly, the bonding has to preserve the transparency of the glass. In fact, the glass is often chosen because of its transparency at visible wavelengths for optical applications. Secondly, the bonding must

be non-toxic to be able to be used in biomedical applications. Finally, the bonding has to be sufficient to seal the device without obstructing or changing the depth of the microfluidic channel.

For SACE there is no report or data about the possibility of glass-to-glass bonding after machining. Compared to other microfabrication technic used in MEMS fabrication, SACE is a process made in a relatively unclean environment. Generally, the glass-to-glass bonding require well controlled environment control to be achieved. However, to keep the simplicity of the SACE the glass-to-glass bonding has to be achieved without substantial post processing. For this section a direct bonding of two glasses square wafers after SACE machining was achieved. The device machined before the bounding was a microfluidic Y-mixer. The direct bonding was achieved in collaboration with an industrial partner: Micronit, Netherlands.

### *12.1.1 Bonding technique*

Many bonding techniques have been developed in past years for different types of applications [59]. The most common-bonding approaches are: adhesive bonding, anodic bonding and fusion bonding. Other non-traditional technique at room temperature have been developed, but those are less versatile and not desirable for a device that has to be used at high pressure or in a commercial perspective. The adhesive bonding and the anodic bonding require the addition of an intermediate layer between the two glass layers that is not desirable for our process and application [59]. Because of that, the method chosen in this work is fusion bonding.

Fusion bonding is based on the intermolecular interaction between the two glass layers at high temperature (around 580 C$^{o}$ [59]) and pressed together at around one hundred newton. When this high pressure and high temperature is applied the Si-OH of both contact surfaces link to form Si-Si bonds. Because of that, this technique depends strongly on a perfect contact between the two glass layers. Typically, a RMS roughness of 0.5 nm is needed. Because of this requirement, a perfect surface without bulges or HAZ is needed.

### *12.1.2 Methodology*

To machine the Y-mixer, we use the Posalux SA machine (section 3.2). The Y-mixer has two inlets connected by two channels of 2cm length connected with an angle of 45º to a mixing channel of 3cm length ended by an outlet. All channel is 400µm width (W) and 200µm depth. The work-piece is a 4 inch borofloat 33-Schott wafer of 0.7cm thickness. The bonding is made between this wafer and a 0.1cm thickness borofloat glass layer. Y-mixer channels are machined in sodium hydroxide 20wt% electrolyte with a pulsed voltage: high-level= 37.50V, low-level= 22.50V, period= 3ms, duty cycle= 50%. The tool-electrode used for this test is a tungsten carbide cylinder of 175µm cylinder whose we apply a 500rpm rotation. The inlet and the outlets of the Y-mixer was machined with the same parameter. This is a rough machining, the machining quality is not good, if the direct bonding under those parameters the direct bonding can be achieved under any parameters. The fusion bonding was performed by Micronit microfluidics, Netherlands, at high-annealing temperature and basic cleaning processes prior to the bonding, to remove any organic contamination. The exact parameters of the bonding cannot be presented in this document because of the industrial secrecy policies of Micronit microfluidics**.**

### *12.1.3 Design of Y-mixer*

First, the bounded Y-mixer was tested and characterized to make sure the device operate properly. The dimensions of the Y-mixer was chosen to obtain a full mixing at the end of it. The mixing profile in a Y-mixer with a rectangular profile with unidimensional variable is defined by the Equation 13. This equation comes from the resolution of the diffusion equation. The diffusion is assumed to only occur in the cross-section.

*Equation 13*

$$C(\tilde{x},\tilde{t}) = 1/2 + \sum_{n=0}^{\infty} \frac{\sqrt{2}(-1)^n}{\pi(2n+1)} e^{-\tilde{t}/\tau_n} \vartheta_n(\tilde{x})$$

Where,

$$\tau_n = \frac{W^2}{D\pi^2(2n+1)^2} \; ; \; \vartheta_n(\tilde{x}) = \sqrt{2}cos\big(\pi\tilde{x}(2n+1)\big)$$

C refers to the concentration x the cross-section direction, t the time, W the channel width and D the diffusion coefficient. Equation 14 represents the percentage of mixing using the mean concentration and it standard deviation:

*Equation 14*

$$f[\%] \approx 1 - \frac{\sigma}{\langle C \rangle}$$

By combining Equation 13 and Equation 14, we obtain an expression of the mixing percentage as a function of the parameter of the channel:

*Equation 15*

$$f[\%] \approx 1 - \frac{2\sqrt{2}}{\pi} exp\left(-{}^{t}/_{\tau_0}\right) \rightarrow 0.95 \approx 1 - \frac{2\sqrt{2}}{\pi} exp\left(-{}^{t_{95\%}}/_{\tau_0}\right)$$

Now we can find an expression for the time to obtain a 95% mixing:

*Equation 16*

$$t_{95\%} = \tau_0 ln\left(\frac{40\sqrt{2}}{\pi}\right)$$

Where,

$$\tau_0 = {}^{W^2}/_{\pi^2 D}$$

And finally with Equation 16 we have a simplified expression for the mixing length:

*Equation 17*

$$L_{95\%} = \langle v_{flow} \rangle t_{95\%}$$

### *12.1.4 Connections to macro-world*

Standard tube connectors are glued with epoxy on the inlets and the outlet of the mixer. Inlets was connected to two micropumps (NE-500 Syringe pump – New Era Pump Systems inc) which was filled with DI water and coloured food dyes.

### *12.1.5 Results*

As we can see in Figure 68 the mixing occur in the Y-mixer with a 100% mixing at the end.

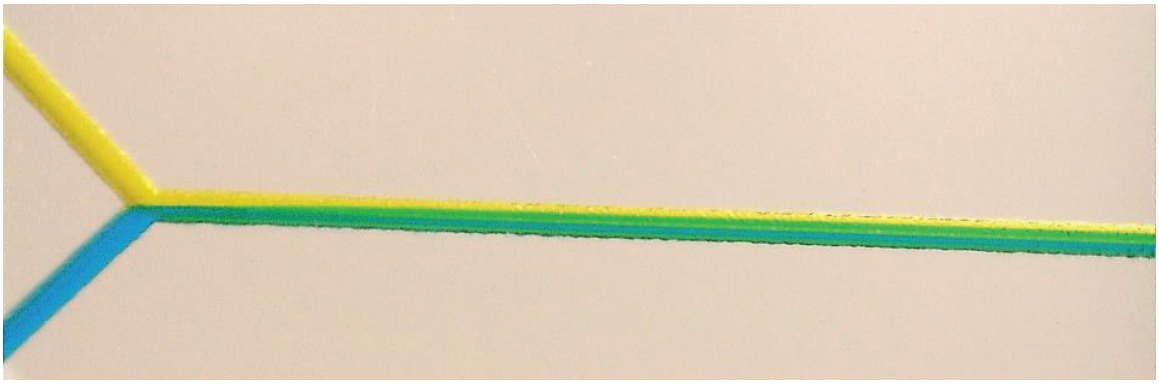

*Figure 68 : Coloured food dyes in the Y-mixer after fusion direct bonding.*

The bonding is characterized for uniformity across the total bonded surface. The bonding strength is first tested with the razor blade insertion test [60], [61]. In this test a razor blade is insert in the device at the interface between the two glass layers of the device. It is know that the length of insertion of the razor blade and the propagation of cracks is proportional to the bonding strength. It appears that is impossible to insert a razor blade between the two glass layers. The razor blade bend and/or chip before any separation on any side occur at the bonded interface. This is typical of a perfect fusion bonding, because after a fusion bonding the interface should disappear. To prove this affirmation, two tests have been done. Figure 69 shows a diamond-saw cross-sections cute of the Y-mixer taken by an electronic microscope (SEM). To obtain this picture the glass sample was polished after mounting it in an epoxy holder. We clearly see the lack of interfaces.

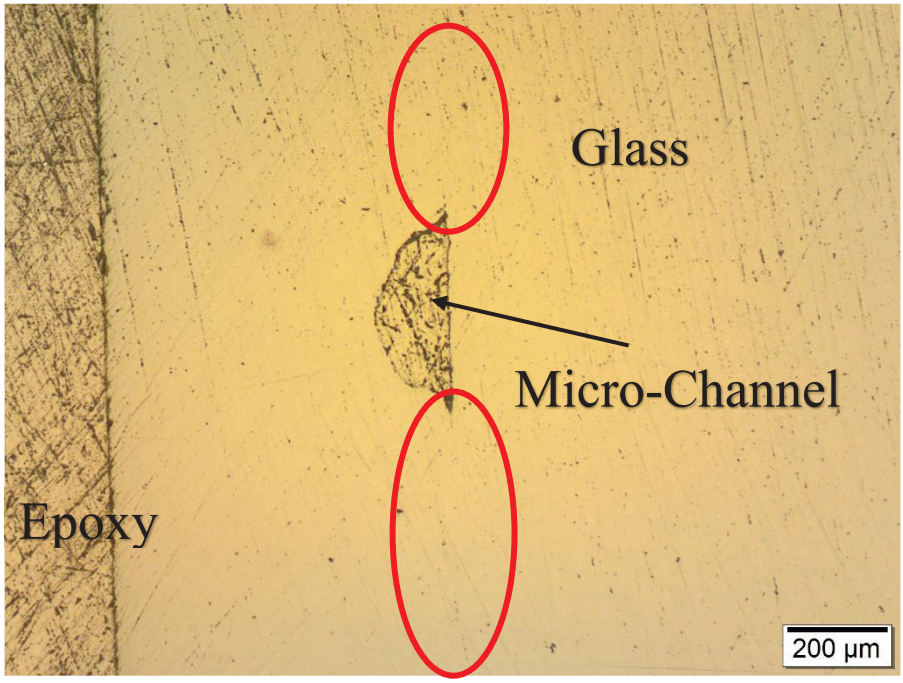


*Figure 69 : Cross-section of the Y-mixer after fusion direct bonding. We clearly see the lack of interface in the bonding region (location of the bonding interface in red oval).*

The non-presence of bonding defects such as delamination, voids and cracks has been analyzed by an acoustic method, called Sonoscan from Sonolab [62]. This method uses ultrasound (above 20 KHz) to map an interface between two materials. Ultrasound is an elastic disturbance that propagates in liquid or solid and bounce on interfaces. As one can see in Figure 70 the Sonoscan has not been able to find an interface in our Y-mixer. This is proved the quality of the bonding between the two glass layers.

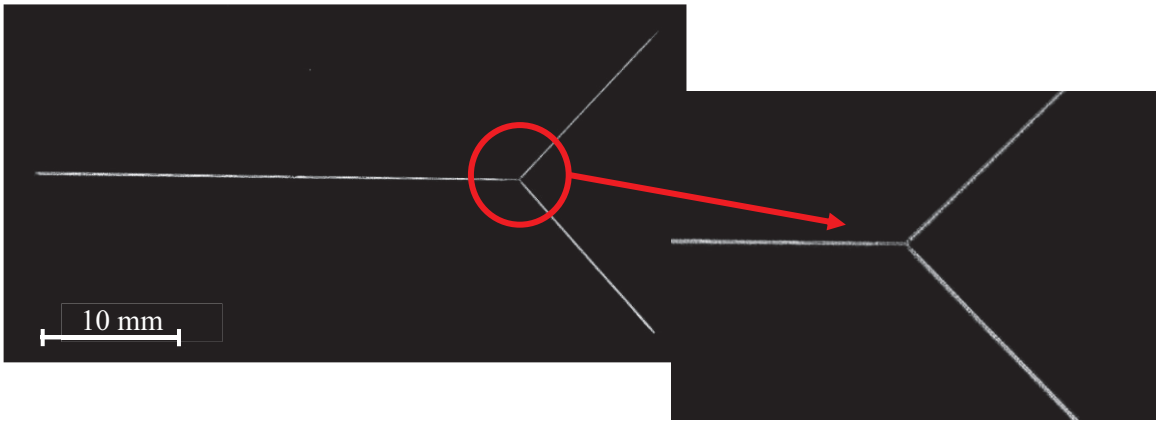


*Figure 70 : Sonoscan image of the Y-mixer after the fusion direct bonding. The black part of the image refer to the bulge. The white part refer to the void inside the channel.*

## 12.2 Gorilla-glass

New glass based materials have been recently developed to respond to the needs of the high-technology industry for applications such as cellphone front glasses. Gorilla-glass is one of this new glass-based material. Gorilla-glass is a flexible glass where residual mechanical stress is removed from it[4]. However, glass use in cellphone industry are quench to avoid scratching by the future user, because of that the machining of those glass is not easy (brittle material). Up to now, for example the speaker slot is machine before the quenching which is not optimal (possible thermal distortion of the surface then quenching). SACE can over pass this problem because it can be used after the quenching: minimum force is applied on the work-piece during the machining and the machining itself does not induce stress in the work-piece. Also, the machining of glass by laser ablation, for example, can frequently cause debris deposition to the glass surface or surface cracking [63]. This comes from the nature of the ablation mechanism. During laser ablation the thermal energy accumulation cause material ejection from the work-piece. This is not the case with SACE. SACE is a chemical etching and not a physical milling based technic. The quality of the machining is not affected by stress or defect in the work-piece material. To show the flexibility of the SACE machining a simple rectangular cute with circular edge was a machined at Posalux SA to show the unique capability of the SACE to machining independently of the type and the internal stress of glass. Figure 71 shows the rectangular cute with circular edge machined in a Gorilla-glass work-piece of 1 mm thickness. This cute was done using the high rough machining followed by a polishing with a 50µm tool diameter with a 45º bevel at the tip. The rough machining was done at 20mm/min tool traveling speed with: high-level= 30V, low-level= 15V, period= 5ms, duty cycle= 60%. The polishing is done with two passes at 20mm/min tool traveling speed with: high-level= 28V, low-level= 14V, period= 5ms, duty cycle= 60%. The polishing gap has been maintained at 10µm. This shows the fact SACE can machine properly any glass based material.

[4] http://www.corninggorillaglass.com/en/technology/how-its-made

*Figure 71 : Image of the Gorilla-glass rectangular cute with circular edge.*

# 13 Conclusion

The electrochemical discharge phenomenon involved in SACE process is complex and needs considerations of multiple parameters. The main objectives of this study were to untangle all those considerations and give some solutions path to a future full control over the process. A full control over the SACE process will allow a better machining speed, a constant quality and a full predictability of the outcome. Because up to now the only way to obtain a specific machined structure is to do empirical tests, which is a costly not a sustainable approach for a future industrial application of the process. Therefore, in this study we highlight some important aspect and parameters of the process. Also, we investigate three different approaches to optimize the process, this investigation gives a solution path for the future industrial application of the SACE process.

## 13.1 Highlights

The key achievements and contributions of this work are enumerated as follows:

I. Electrolyte based on KOH is better in terms of drilling quality and speed. The machining speed can be improved eight times by using 50wt% KOH over 30wt% NaOH. Also, KOH generate less defects and the type of defect generated are less significant. Lastly, the general geometry of holes drilled with KOH is more uniform (less flared). Because of all those facts the uses KOH must be prioritized over NaOH.

II. The electrolyte flow in the processing cell is essential to obtain a good machining and avoid any local dry out during machining. Also, a good microscopic flow provides faster machining. The increase of the bulk flow increases the microscopic flow (more electrolyte flushing at the machining zone). The electrolyte flow also manages the heat distribution at the machining zone. Therefore, an optimum electrolyte flow for a specific electrical input combination exist (for a specific heat and ions source).

III. A better work-piece holding system has to be developed, to prevent any variation in the electrolyte level.

IV. The drilling speed can significantly be improved by using a cylindrical tool-electrode with a bevel angle tip (better microscopic flow). The machining speed can be improved by about 800% for a 300μm hole deep by using a 60º tip angle tool-electrode over a flat tool-electrode tip. Also, the use of a bevel angle tip increases the machining quality.

V. Pulsed voltage give full control over the gas film dynamics. The switch from the high-level to the low-level generate a gas film collapsing event if the low-level is over the critical voltage. The effect of a pulse voltage can be analyzed using the mean current over time.

VI. There exists an optimum combination of electrical parameters which provides good machining quality and machining speed. This optimum combination depends strongly on the environment during the machining: type of electrolyte, electrolyte levels, electrolyte flow, the nature of the work-piece, tool-electrode runout and the machining strategy.

VII. A new machining strategy was developed using polishing. This method allows faster machining and better machining quality. This technic also gives an easier outcome determination.

VIII. The polishing quality and by ricochet the machining quality is proportional to the quantity of energy give to a specific place on the work-piece.

IX. The nature and the composition of the spark discharges involve in SACE was found: Na-I {330.3, 588.9, 589.6, 818.3, and 819.5nm} or K-I {404.8, 691.1, 693.8, 766.5, and 769.9 nm}, also emission from H I, O I, and OH band (A-X) were also found. While the emission intensities of Na, K and OH decreased with increasing current, the ratios of metallic-to-OH remained fairly constant. This indicates that most of the Na, K and OH vapors result from the gas film formation and not so much from the discharge ↔ tool-electrode interactions.

X. The excitation temperature of spark discharges was found using the Boltzmann plot method (5400±1200K for NaOH-based solution and 4500±850K for KOH-based solution). These values were higher than those deduced from the analysis of the

rovibrational structure of OH (1000-1500K), confirming the out-of-equilibrium nature of spark discharges produced in electrolyte solutions.

XI. The SACE process allows direct glass-to-glass fusion bonding, a key element for microfluidic and others future applications of the process.

XII. Gorilla-glass can be machine with the SACE, which is promising for the electronic industry.

## 13.2 Outlook

In this final section, we will discuss the future work required for the industrial use of SACE based on the actual understanding of the process after this study. Firstly, some considerations to improve the processing cell, based on educated guess. Secondly, a possible way to improve the SACE process via the thermo-hydrodynamic approach is presented. After this study, it became clear that the way to improve SACE in the industrial application perspective is by the thermo-hydrodynamic approach. If we can collect more data about the heat transfer and the electrolyte motion around the tool-electrode during the machining and develop a model the SACE process will become predictable and faster. The collection of data about the thermo-hydrodynamics can be done under the machine learning principal which is a viable new approach to improve industrial processes and easily applicable to the SACE. It appears the chemical improvement of the process is limited and adding wetting agent or a mixture of the electrolyte has no significant impact on the process. Of course the use of an electrolyte over another and different concentrations have an impact on the process but those improvements cannot solve all challenges of the technology. In the same matter, the spectroscopic approach is not viable for industrial approach. It is true the spectroscopic analyze of the process gives valuable information and lead to more comprehension but that information does not increase the machining quality of the speed of the process. It is more theoretical than practical.

### *13.2.1 Processing Cell*

To prevent the effect of multiple electrolyte levels over the work-piece a better type of holding system has to be designed. A holding system where the cell, the holding system and the work-piece are on the same level to prevent any perturbation of the electrolyte

level. This is particularly true when a machined device needs all the work-piece surface to be achieved. Remember a multi-level processing cell gives different machining quality over the work-piece surface for a specific combination of parameters. Therefore, the design of the processing cell needs to be improved to allow a better reproducibility.

Also, we had observed an accumulation of black material on the tool-electrode during machining. This black material probably comes from contamination from the processing cell or/and from the degradation of the counter-electrode. This contamination is probably attracted to the tool tip of the strong electrical fields occurred at the tool tip. This black material contamination tends to increase the size of the tool and increase in the same timer the machining time. Materials such metal, weak plastic and rubber need to be banned from the SACE machine construction.

### *13.2.2 Thermo-Hydrodynamic model*

This outlook gives a possible solution track for the heat flux influence presented in chapter 9.3. Based on the observation made about the optimum energy needed to have a good polishing, a model based on the transient heat conduction equation can be developed to explain the experimental results. In this section, a system of equation and a model is presented. This system of equations can be solved numerically by the finite difference method. Therefore, this section is more a possible way to predict the SACE machining output than an explanation. This model can be improved to understand better the physics of SACE process. The model is fully developed until it becomes necessary to use numerical calculators. Another algorithm can be developed based on the use of cross-correlation with template signals that look like the gas film formation signal. Preliminary work shows a good potential for this method but more refinement is needed. Two different ways of developing the calculations are used. Those calculation techniques are based on work made for the Laser machining. The first model is based on [64] and the second one is based on [65]. Those models have been chosen over others because of the more general aspect of the method. Another technique uses more specific assumptions which can hardly transfer on the SACE process. Other models used to explain the Laser machining or the arc welding can also be a good start: [66], [67], [68], [69], [70], [71]. Anyhow, those models basically turn around the same considerations: the resolution of the transient heat conduction

equation by Green's function or by separation of variables in summation. This can led to a better understanding and a better repeatability of the SACE process. It is necessary to have a model to predict the output of a SACE machining because of the target commercial market for this technology.

During the polishing (chapter 0) the tool-electrode (heat source) move on the work-piece surface with a back and forwards motion. Because of that the heat near the polished surface increase periodically over the time. To simplify the model, a linear motion path is assumed and not a circular motion. The linear motion corresponds to the polishing of a micro-channel other than a pillar. The tool-electrode is modeled by a cylinder with a specific height ($h$) and a specific radius ($r_0$). The radius corresponds to the radius of the tool-electrode. The tool-electrode is supposed to have a uniform heat over it surfaces (Figure 72). The thermal properties of the system are considered constant. The thermal properties of the electrolyte can be used because during the polishing tool-electrode is not directly in contact with the glass work-piece. Before present the model, let's introduce two important variables, the heat source position over time and the spatial heat source distribution. Also, this model is, for simplification, a pure heat exchange model; obviously, as seen in chapter 1, the SACE is not a pure heat exchange problem; it involves fluid mechanics and chemical kinetics, but a study of the heat distribution can be a good start.

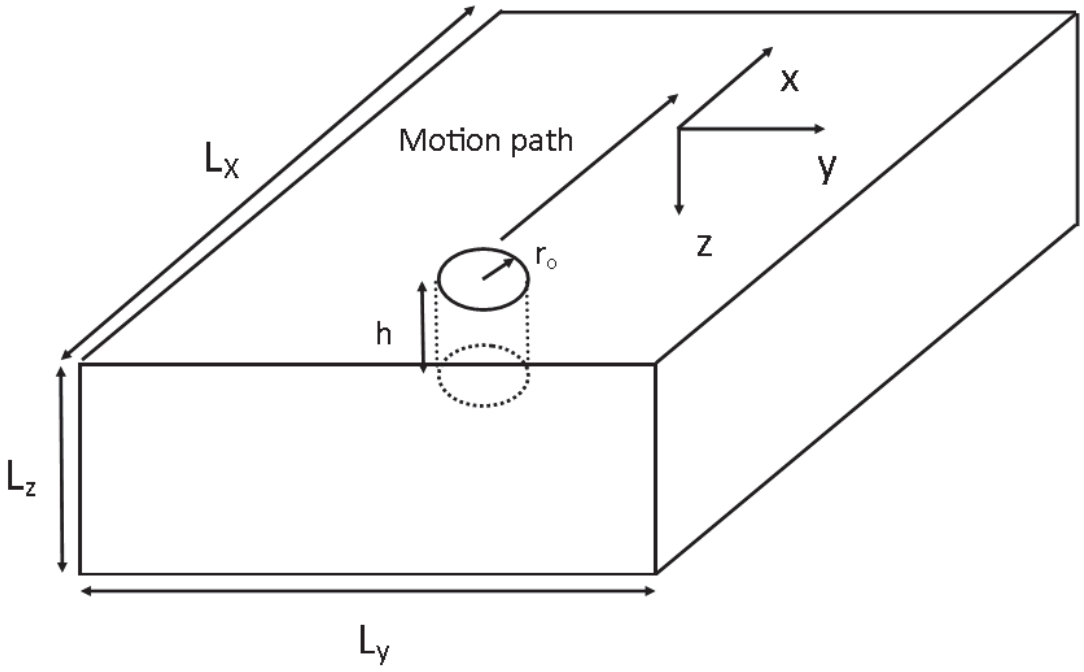


*Figure 72 : Schematic view of the polishing model.*

### *13.2.3 Heat Source Position*

The heat source position over the time need to satisfy the following pattern (Figure 73):

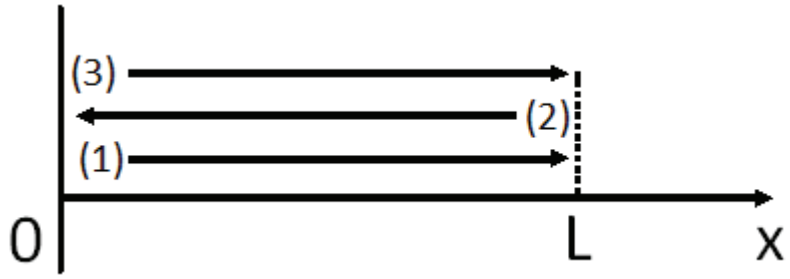


*Figure 73 : Heat source motion pattern.*

Where L is the length of the channel. This motion can be defined by the following equation (Equation 18) with *v* the speed of the tool-electrode and *t* the time. Thus we have an expression which the position of the heat source center over time:

*Equation 18*

$$x_c(t) = L\left|sin\left(\frac{2\pi vt}{L}\right)\right|$$

### *13.2.4 Spatial Heat Source Distribution*

The distribution of a cylindrical heat source can be made by using the rectangular function:

*Equation 19*

$$rect\ fct = \Pi(t/\tau) = H(t + \tau/2) + H(t - \tau/2) \ \rightarrow \ fct = \Pi((t - b)/a)$$

Where, Π is the Heaviside function. Figure 74 shows the representation of the rectangular function. The center of this spatial heat source distribution is defined by Equation 18.

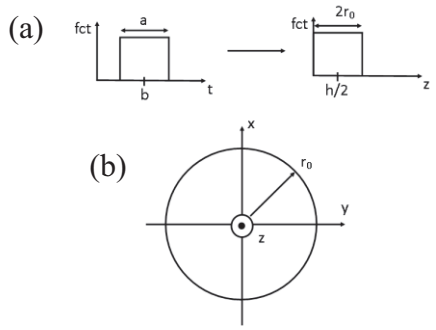


*Figure 74 : Schematic view of the spatial heat source distribution (a) rectangular function (b) section of the Cartesian distribution of the heat source distribution.*

Based on this, the heat distribution can be defined:

*Equation 20*

$$q'''(x, y, z, t) = P\ \Pi\left(\frac{\sqrt{x^2 + y^2}}{2r_0}\right)\Pi\left(\frac{2z - h}{2h}\right)$$

where, P is the intensity of the heat source. The intensity of the heat source depends on the electrical potential and current between the tool-electrode and the counter electrode. If a DC voltage signal is applied to the tool-electrode, the intensity of the heat source is proportional to the electrical potential multiply by the current:

*Equation 21*

$$P \propto \Delta V \cdot I$$

If a pulse voltage signal is apply to the tool-electrode the Equation 22 become:

*Equation 22*

$$P = P_{Lo} + (P_{Hi} - P_{Lo})\Pi\left(\frac{t}{t_{Hi}}\right)\sum_{\eta=0}^{\infty}\delta\big(t - \eta(t_{Hi} + t_{Lo})\big)$$

Where, δ is the Dirac function, $P_{Lo}$ is the intensity of the low-level and $P_{Hi}$ is the intensity of the high-level. This function allows to vary mathematically the intensity over time with a specific duty cycle, period, low-level and high-level. In reality most of the heat is created at the edge of the tool-electrode tip, where the concentration of sparks is the highest. But, here we assume that the heat distribution generated is uniform due to the gas film. Further analysis can include a more complex spatial heat distribution.

### *13.2.5 First Method*

This model is based on the work made by [64]. With the position of the heat source over the time and the heat source spatial distribution in the hands, this model is an attempt to solve the transient heat conduction equation (Equation 23) for the system (Figure 72):

*Equation 23*

$$\frac{\partial^2 T}{\partial x^2} + \frac{\partial^2 T}{\partial y^2} + \frac{\partial^2 T}{\partial z^2} + \frac{q'''(x,y,z,t)}{K_T} + \frac{1}{\alpha}\frac{\partial T}{\partial t} = 0$$

The volume heat source term is $q'''(x,y,z,t)$ depending on the time for its position and intensity. The tool-electrode move in the integration domain and because of using pulsed voltage the intensity vary. The temperature can be normalized to simplify the analysis, by the subtraction of the surrounding temperature (Equation 24):

*Equation 24*

$$\theta(x,y,z,t) = T(x,y,z,t) - T_0$$

Therefore, Equation 23 with the substitution in (Equation 24) becomes:

*Equation 25*

$$\frac{\partial^2 \theta}{\partial x^2} + \frac{\partial^2 \theta}{\partial y^2} + \frac{\partial^2 \theta}{\partial z^2} + \frac{q'''(x,y,z,t)}{K_T} = \frac{1}{\alpha}\frac{\partial \theta}{\partial t}$$

One of the most important part in the resolution of a partial differential equation is the establishment of the initial condition and the boundary conditions. As at t=0 the machining begins, the temperature is uniform everywhere ($\theta(x,y,z,t=0) = 0$). Because

the integration domain is a very large parallelepiped if follows: at $L_y/2\,, L_x/2 \gg r_0$ and $L_z \gg h$ the temperature is supposed to be constant at the beginning. This is refered to Dirichlet conditions at face $x = \pm L_x/2$, $y = \pm L_y/2$ and $z = L_z$. Those conditions can be assumed because of the heat concentration in a small area and because of the large heat absorption of the integration domain. This is not far from the reality because of the width of the processing cell. For the top surface $z = 0$ we assume a convection boundary with the ambient environment. With those non-homogenous boundary conditions the equation can be solved by separation of variables expressed as series expansion of eigenfunctions. The temperature is therefore expressed in a combination of four different equations:

*Equation 26*

$$\theta(x, y, z, t) = \sum_i \sum_j \sum_k \Theta_{ijk}(t)\, X_i(x) Y_j(y) Z_k(z)$$

The eigenfunctions and eigenvalues of $X_i(x), Y_j(y)$ and $Z_k(z)$ can be imposed and expressed as:

*Equation 27*

$$X_i(x) = cos(\alpha_i x);\ \alpha_i = \frac{2i+1}{2L_x}\pi, i = 0,1, \dots, n$$

*Equation 28*

$$Y_j(y) = cos(\beta_j y);\ \beta_j = \frac{2j+1}{2L_y}\pi, j = 0,1, \dots, n$$

*Equation 29*

$$Z_k(z) = cos(\gamma_k z) + \frac{H}{K_T \gamma_k} sin(\gamma_k z);\ \ \tan(\gamma_k L_z) = -\frac{K_T \gamma_k}{H}$$

Here, $K_T$ and H are respectively the thermal conductivity of the electrolyte and the convection coefficient at the top surface. In addition to that $\alpha_i$, $\beta_j$ and $\gamma_k$ are the separation variables. The last equation (Equation 29) comes from the convective boundary condition on the top surface of the integration domain. Therefore, the heat source equation can be expressed by the separation of variables:

*Equation 30*

$$q''' = \sum_i \sum_j \sum_k \phi_{ijk}(t)\, X_i(x) Y_j(y) Z_k(z)$$

To solve Equation 25 with the assumption of separation of variables, we can use the orthogonality property of the eigenfunctions. The idea is to find an expression for $\phi_{ijk}(t)$ which is the unknown variable in the equation.

*Equation 31*

$$\int_0^{L_x} \int_{-L_y/2}^{L_y/2} \int_0^{L_z} q''' X_i(x) Y_j(y) Z_k(z) dx dy dz$$
$$= \phi_{ijk}(t) \int_0^{L_x} {X_i}^2(x) dx \int_{-L_y/2}^{L_y/2} {Y_j}^2(y) dy \int_0^{L_z} {Z_k}^2(z) dz$$

This equation can be solved analytically. The right part of this equation is solved as presented by [64]:

*Equation 32*

$$\int_0^{L_x} {X_i}^2(x) dx = \int_0^{L_x} cos^2(\alpha_i x) dx = L_x/2$$
$$\int_{-L_y/2}^{L_y/2} {Y_j}^2(y) dy = \int_{-L_y/2}^{L_y/2} cos^2(\beta_i y) dy = L_y/2$$

Which leads to Equation 33:

*Equation 33*

$$\int_0^{L_x} \int_{-L_y/2}^{L_y/2} \int_0^{L_z} q''' X_i(x) Y_j(y) Z_k(z) dx dy dz$$
$$= \frac{L_x L_y}{4} \phi_{ijk}(t) \int_0^{L_z} \left[ cos(\gamma_k z) + \frac{H}{K_T \gamma_k} sin(\gamma_k z) \right]^2 dz$$

And with the solving of the integration on the z component:

*Equation 34*

$$\int_0^{L_x}\int_{-L_y/2}^{L_y/2}\int_0^{L_z} q'''X_i(x)Y_j(y)Z_k(z)dxdydz = \frac{L_xL_y}{4}\phi_{ijk}(t)\left\{\frac{L_z}{2}\left[1+\frac{H^2}{K_T^2\gamma_k^2}\right]+\frac{\sin(2\gamma_kL_z)}{4\gamma_k}\left[1-\frac{H^2}{K_T^2\gamma_k^2}\right]+\frac{H}{K_T\gamma_k^2}sin^2(\gamma_kL_z)\right\}$$

Now we solve the right part of Equation 31. The integration on the z variable is not linked with the other two spatial variables (x,y). Also, the z position of the heat source does not change over the time as on the x position. So, this integral can be solved separately (Equation 35). It is not the case for (x,y) because of the nature of the heat distribution.

*Equation 35*

$$\int_o^{L_z} \Pi\left(\frac{2z-h}{2h}\right)\left(cos(\gamma_kz)+\frac{H}{K_T\gamma_k}sin(\gamma_kz)\right)dz = \frac{1}{\gamma_k}\left[sin(\gamma_kz)+\frac{H}{K_T\gamma_k}cos(\gamma_kz)\right]_0^h = \frac{1}{\gamma_k}\left[in(\gamma_kh)+\frac{H}{K_T\gamma_k}\left(1-cos(\gamma_kh)\right)\right]$$

The integration interval on x and y has to be changed to take into account the moving position of the heat source. The integration interval depends on the position of the heat source relative to the initial position: the x variable interval changes according $[L_x;0]\rightarrow[x_c+r_0;x_c-r_0]$ and for y variable according: $\left[L_y/2\,;-L_y/2\right]\rightarrow\left[\sqrt{r_0^2-(x-x_c)^2};\,-\sqrt{r_0^2-(x-x_c)^2}\right]$. Where, $x_c(t)$ is the heat source position ($x_c(t)$) and $r_0$ gives the volume of the heat source. The heat source position as been defined previously by Equation 18. Therefore, the double integral over x and y is solved:

*Equation 36*

$$\int_{x_c-r_0}^{x_c+r_0}\int_{-\sqrt{r_0^2-(x-x_c)^2}}^{\sqrt{r_0^2-(x-x_c)^2}} P*\Pi\left(\frac{\sqrt{x^2+y^2}}{2r_0}\right)cos(\alpha_ix)cos\left(\beta_jy\right)dxdy$$

Which leads to a function dependent of the heat source position:

*Equation 37*

$$fct(x_c) = \frac{4r_0}{\beta_j}\left\{ sin\left(\beta_j\sqrt{r_0^2 - x_c^2}\right) + \frac{\beta_j x_c^2}{\sqrt{r_0^2 - x_c^2}}\cos\left(\beta_j\sqrt{r_0^2 - x_c^2}\right) - \frac{(r_0^2 + 3x_c^2)sin\left(\beta_j\sqrt{r_0^2 - x_c^2}\right)}{3}\left[\alpha_i^2 + \frac{\beta_j^2 x_c^2}{r_0^2 - x_c^2}\right] - \frac{(r_0^2 + 3x_c^2)\beta_j r_0^2\cos\left(\beta_j\sqrt{r_0^2 - x_c^2}\right)}{6(r_0^2 - x_c^2)^{3/2}}\right\}$$

This last equation has been solved using an analytical solver software (Wolfram Alpha). By the combination of Equation 18, Equation 31, Equation 34 and Equation 37 we have an expression for $\phi_{ijk}(t)$. This expression can be implement in the transient heat conduction equation and solve the time dependant part:

$$\frac{1}{\alpha_T}\frac{d}{dt}\Theta_{ijk}(t) = -\left(\alpha_i^2 + \beta_j^2 + \gamma_k^2\right)\Theta_{ijk}(t) + \frac{\phi_{ijk}(t)}{K_T}$$

This can be solved by substituting the expression of $\phi_{ijk}(t)$ and using the Laplace transform. As we can see, this equation, because of the nature of $\phi_{ijk}(t)$, is difficult to solve analytically and requires numerical integration. This last step is out of the scope of this work but can lead to a better control over the polishing process. Up to now all SACE machining need a certain number of optimization. By optimization we mean a series of tests to obtain the desired machining and quality. The length of this series of tests can be reduced by having a proper model of the machining and the polishing.

### *13.2.6 Second Method*

This method, as presented before, is based on the work of [65]. The same integration and heat source distribution used in the previous model is considered for this solving technic. For this model we assume a mathematical statement in which the coordinate move with the heat source. Therefore, we have a quasi-steady-state three dimensional problem where the time component can be removed:

*Equation 38*

$$\nabla^2 T + \frac{v}{\alpha}\frac{\partial T}{\partial x} + \frac{q(x,y,z)}{K_T} = 0$$

With the following boundary condition,

*Equation 39*

$$T(x,y,z) = T_0 \; at \; x = \pm\infty; \; y = \pm\infty; \; z = \pm\infty$$

This is the same assumption of the previous model. The main idea of this method is to use the Green's function to find an expression of the temperature. The Green's function is:

*Equation 40*

$$T(x,y,z) = T_0 + \iiint_{-\infty}^{\infty} q(\zeta,\varepsilon,\eta)\, G(x,y,z;\zeta,\varepsilon,\eta) d\eta d\varepsilon d\zeta$$

With the following expression for the Green's function:

*Equation 41*

$$G(x,y,z;\zeta,\varepsilon,\eta) = \frac{1}{4\pi K_T} \frac{exp\left\{v\left[(x-\zeta) - \sqrt{(x-\zeta)^2 + (y-\varepsilon)^2 + (z-\eta)^2}\right]\right\}}{\sqrt{(x-\zeta)^2 + (y-\varepsilon)^2 + (z-\eta)^2}}$$

By substitution in Equation 38 the expression of the Green's function (Equation 41) we obtain:

*Equation 42*

$$\nabla^2 G + \frac{v}{\alpha}\frac{\partial G}{\partial x} + \frac{\delta(x-\zeta)\delta(y-\varepsilon)\delta(z-\eta)}{K_T} = 0$$

Therefore, the equation to be solved has an expression for the temperature defined as:

*Equation 43*

$$T(x,y,z) = T_0 + \frac{P}{4\pi K_T} \iiint_{-\infty}^{\infty} \Pi\left(\frac{\sqrt{\zeta^2+\varepsilon^2}}{2r_0}\right) \Pi\left(\frac{2\eta - h}{2h}\right) \frac{exp\left\{v\left[(x-\zeta) - \sqrt{(x-\zeta)^2 + (y-\varepsilon)^2 + (z-\eta)^2}\right]\right\}}{\sqrt{(x-\zeta)^2 + (y-\varepsilon)^2 + (z-\eta)^2}} d\eta d\varepsilon d\zeta$$

With the substitution of the integration interval to take into account the motion of the heat source:

*Equation 44*

$$T(x,y,z) = T_0 + \frac{P}{4\pi K_T}\int_{-r_0}^{r_0}\int_{-\sqrt{r_0^2-\zeta^2}}^{\sqrt{r_0^2-\zeta^2}}\int_{0}^{h}\frac{exp\left\{v\left[(x-\zeta)-\sqrt{(x-\zeta)^2+(y-\varepsilon)^2+(z-\eta)^2}\right]\right\}}{\sqrt{(x-\zeta)^2+(y-\varepsilon)^2+(z-\eta)^2}}d\eta d\varepsilon d\zeta$$

This last equation cannot be solved analytically.

# Bibliography


[1] W. . Peng and Y. . Liao, “Study of electrochemical discharge machining technology for slicing non-conductive brittle materials,” *J. Mater. Process. Technol.*, vol. 149, no. 1–3, pp. 363–369, Jun. 2004.

[2] E. S. Lee, D. Howard, E. Liang, S. D. Collins, and R. L. Smith, “Removable tubing interconnects for glass-based micro-fluidic systems made using ECDM,” *J. Micromechanics Microengineering*, vol. 14, no. 4, pp. 535–541, Apr. 2004.

[3] K. Furutani and H. Maeda, “Machining a glass rod with a lathe-type electro-chemical discharge machine,” *J. Micromechanics Microengineering*, vol. 18, no. 6, p. 065006, Jun. 2008.

[4] J. D. Abou Ziki, T. Fatanat Didar, and R. Wüthrich, “Micro-texturing channel surfaces on glass with spark assisted chemical engraving,” *Int. J. Mach. Tools Manuf.*, vol. 57, pp. 66–72, Jun. 2012.

[5] R. Wüthrich and L. a. Hof, “The gas film in spark assisted chemical engraving (SACE)—A key element for micro-machining applications,” *Int. J. Mach. Tools Manuf.*, vol. 46, no. 7–8, pp. 828–835, Jun. 2006.

[6] “Spark Assisted Chemical Engraving - A Stochastic Modelling Approach,” no. May, 2003.

[7] M. Jalali, P. Maillard, and R. Wüthrich, “Toward a better understanding of glass gravity-feed micro-hole drilling with electrochemical discharges,” *J. Micromechanics Microengineering*, vol. 19, no. 4, p. 045001, Apr. 2009.

[8] C.-P. Cheng, K.-L. Wu, C.-C. Mai, C.-K. Yang, Y.-S. Hsu, and B.-H. Yan, “Study of gas film quality in electrochemical discharge machining,” *Int. J. Mach. Tools Manuf.*, vol. 50, no. 8, pp. 689–697, Aug. 2010.

[9] R. Wüthrich and V. Fascio, “Machining of non-conducting materials using electrochemical discharge phenomenon—an overview,” *Int. J. Mach. Tools Manuf.*, vol. 45, no. 9, pp. 1095–1108, Jul. 2005.

[10] A. Kulkarni, R. Sharan, and G. K. Lal, “Measurement of Temperature Transients in the Electrochemical Discharge Machining Process,” *Temp. Its Meas. Control Sci. Ind. vol.7*, vol. 7, no. 1, pp. 1069–1074, 2003.

[11] T. F. Didar, A. Dolatabadi, and R. Wüthrich, “Characterization and modeling of 2D-glass micro-machining by spark-assisted chemical engraving (SACE) with constant velocity,” *J. Micromechanics Microengineering*, vol. 18, no. 6, p. 065016, Jun. 2008.

[12] X. D. Cao, B. H. Kim, and C. N. Chu, “Micro-structuring of glass with features less than 100μm by electrochemical discharge machining,” *Precis. Eng.*, vol. 33,

no. 4, pp. 459–465, Oct. 2009.

[13] S. K. Jui, A. B. Kamaraj, and M. M. Sundaram, “High aspect ratio micromachining of glass by electrochemical discharge machining (ECDM),” *J. Manuf. Process.*, vol. 15, no. 4, pp. 460–466, Oct. 2013.

[14] Y. P. Singh, V. K. Jain, P. Kumar, and D. C. Agrawal, “Machining piezoelectric (PZT) ceramics using an electrochemical spark machining (ECSM) process,” *J. Mater. Process. Technol.*, vol. 58, no. 1, pp. 24–31, 1996.

[15] B. R. Sarkar, B. Doloi, and B. Bhattacharyya, “Parametric analysis on electrochemical discharge machining of silicon nitride ceramics,” *Int. J. Adv. Manuf. Technol.*, vol. 28, no. 9–10, pp. 873–881, 2006.

[16] Y. S. Laio, L. C. Wu, and W. Y. Peng, “A Study to Improve Drilling Quality of Electrochemical Discharge Machining (ECDM) Process,” *Procedia CIRP*, vol. 6, pp. 609–614, Jan. 2013.

[17] J. D. A. Ziki and R. Wüthrich, “Tool wear and tool thermal expansion during micro-machining by spark assisted chemical engraving,” pp. 481–486, 2012.

[18] C.-K. Yang, C.-P. Cheng, C.-C. Mai, a. Cheng Wang, J.-C. Hung, and B.-H. Yan, “Effect of surface roughness of tool electrode materials in ECDM performance,” *Int. J. Mach. Tools Manuf.*, vol. 50, no. 12, pp. 1088–1096, Dec. 2010.

[19] W??thrich, V. Fascio, and H. Bleuler, “A stochastic model for electrode effects,” *Electrochim. Acta*, vol. 49, no. 22–23 SPEC. ISS., pp. 4005–4010, 2004.

[20] B. Bhattacharyya, B. N. Doloi, and S. K. Sorkhel, “Experimental investigations into electrochemical discharge machining (ECDM) of non-conductive ceramic materials,” *J. Mater. Process. Technol.*, vol. 95, no. 1–3, pp. 145–154, 1999.

[21] C.-K. Yang, K.-L. Wu, J.-C. Hung, S.-M. Lee, J.-C. Lin, and B.-H. Yan, “Enhancement of ECDM efficiency and accuracy by spherical tool electrode,” *Int. J. Mach. Tools Manuf.*, vol. 51, no. 6, pp. 528–535, Jun. 2011.

[22] Z.-P. Zheng, H.-C. Su, F.-Y. Huang, and B.-H. Yan, “The tool geometrical shape and pulse-off time of pulse voltage effects in a Pyrex glass electrochemical discharge microdrilling process,” *J. Micromechanics Microengineering*, vol. 17, no. 2, pp. 265–272, Feb. 2007.

[23] R. Wüthrich, B. Despont, P. Maillard, and H. Bleuler, “Improving the material removal rate in spark-assisted chemical engraving (SACE) gravity-feed micro-hole drilling by tool vibration,” *J. Micromechanics Microengineering*, vol. 16, no. 11, pp. N28–N31, Nov. 2006.

[24] V. K. Jain and S. Adhikary, “On the mechanism of material removal in electrochemical spark machining of quartz under different polarity conditions,” *J. Mater. Process. Technol.*, vol. 200, pp. 460–470, 2008.

[25] A. Manna and V. Narang, “A study on micro machining of e-glass-fibre-epoxy

composite by ECSM process," *Int. J. Adv. Manuf. Technol.*, vol. 61, no. 9–12, pp. 1191–1197, 2012.

[26] C. S. Jawalkar, A. K. Sharma, P. Kumar, and D. C. Variable, "Micromachining with ECDM : Research Potentials and Experimental Investigations," pp. 90–95, 2012.

[27] R. Wüthrich, U. Spaelter, and H. Bleuler, "The current signal in spark-assisted chemical engraving (SACE): what does it tell us?," *J. Micromechanics Microengineering*, vol. 16, no. 4, pp. 779–785, Apr. 2006.

[28] Z.-P. Zheng, W.-H. Cheng, F.-Y. Huang, and B.-H. Yan, "3D microstructuring of Pyrex glass using the electrochemical discharge machining process," *J. Micromechanics Microengineering*, vol. 17, no. 5, pp. 960–966, May 2007.

[29] D.-J. Kim, Y. Ahn, S.-H. Lee, and Y.-K. Kim, "Voltage pulse frequency and duty ratio effects in an electrochemical discharge microdrilling process of Pyrex glass," *Int. J. Mach. Tools Manuf.*, vol. 46, no. 10, pp. 1064–1067, Aug. 2006.

[30] Z.-P. Zheng, J.-K. Lin, F.-Y. Huang, and B.-H. Yan, "Improving the machining efficiency in electrochemical discharge machining (ECDM) microhole drilling by offset pulse voltage," *J. Micromechanics Microengineering*, vol. 18, no. 2, p. 025014, Feb. 2008.

[31] R. Wüthrich, U. Spaelter, Y. Wu, and H. Bleuler, "A systematic characterization method for gravity-feed micro-hole drilling in glass with spark assisted chemical engraving (SACE)," *J. Micromechanics Microengineering*, vol. 16, no. 9, pp. 1891–1896, Sep. 2006.

[32] Daher Jana Abou Ziki, "Spark Assisted Chemical Engraving: A Novel Approach for Quantifying the Machining Zone Parameters Using Drilling Forces," *Thesis Dep. Mech. Ind. Eng.*, 2014.

[33] R. Wuthrich, V. Fascio, D. Viquerat, and H. Langen, "In situ measurement and micromachining of glass," *MHS'99. Proc. 1999 Int. Symp. Micromechatronics Hum. Sci. (Cat. No.99TH8478)*, pp. 185–191, 1999.

[34] P. C. Ho, D. A. Palmer, R. H. Wood, A. Sciences, V. Di, O. Ridge, P. O. Box, and N. Si, "Conductivity Measurements of Dilute Aqueous LiOH , NaOH , and KOH Solutions to High Temperatures and Pressures Using a Flow-Through Cell," pp. 12084–12089, 2008.

[35] R. Gilliam, J. Graydon, D. Kirk, and S. Thorpe, "A review of specific conductivities of potassium hydroxide solutions for various concentrations and temperatures," *Int. J. Hydrogen Energy*, vol. 32, no. 3, pp. 359–364, Mar. 2007.

[36] D. M. See and R. E. White, "Temperature and Concentration Dependence of the Specific Conductivity of Concentrated Solutions of Potassium Hydroxide," *J. Chem. Eng. Data*, vol. 42, no. 6, pp. 1266–1268, 1997.

[37] R. Singh, “Solubilization of Organic Dyes in Surfactant Micelles,” 2012.

[38] L. Raymond, P. Chem, M. Solns, N. Phys, H. W. Otto, and R. P. Seward, “Phase Equilibria in the Potassium Hydroxide-Sodium Hydroxide System,” pp. 170–171, 1963.

[39] R. Bj, “Numerical Simulations of Viscous Flow Around Stepped Circular Cylinder Rune Bj{ø}rkli,” no. June, 2012.

[40] S. K. Chak and P. Venkateswara Rao, “Trepanning of Al2O3 by electro-chemical discharge machining (ECDM) process using abrasive electrode with pulsed DC supply,” *Int. J. Mach. Tools Manuf.*, vol. 47, no. 14, pp. 2061–2070, Nov. 2007.

[41] M. R. Razfar, A. Behroozfar, and J. Ni, “Study of the effects of tool longitudinal oscillation on the machining speed of electrochemical discharge drilling of glass,” *Precis. Eng.*, vol. 38, no. 4, pp. 885–892, 2014.

[42] K.-H. Nguyen, P. A. Lee, and B. H. Kim, “Experimental investigation of ECDM for fabricating micro structures of quartz,” *Int. J. Precis. Eng. Manuf.*, vol. 16, no. 1, pp. 5–12, 2015.

[43] J. D. A. Z. Rolf Wüthrich, *Micromachining using electrochemical discharge phenomenon*. Elsevier Inc., 2014.

[44] A. Allagui and R. Wüthrich, “Gas film formation time and gas film life time during electrochemical discharge phenomenon,” *Electrochim. Acta*, vol. 54, no. 23, pp. 5336–5343, 2009.

[45] A. Hickling and M. D. Ingram, “Contact glow-discharge electrolysis,” *Trans. Faraday Soc.*, vol. 60, p. 783, 1964.

[46] L. a. Kuz’michyova, Y. V. Titova, and a. I. Maksimov, “Yields of hydroxyl radicals and hydrogen peroxide in a glow discharge system with a liquid cathode,” *Surf. Eng. Appl. Electrochem.*, vol. 47, no. 6, pp. 517–519, 2012.

[47] W. G. Graham and K. R. Stalder, “Plasmas in liquids and some of their applications in nanoscience,” *J. Phys. D. Appl. Phys.*, vol. 44, no. 17, p. 174037, 2011.

[48] M. D. Lngram, “Contact Glow-Discharge Electrolysis,” 1963.

[49] A. Allagui, A. E. Rojas, T. Bonny, A. S. Elwakil, and M. A. Abdelkareem, “Nonlinear time-series analysis of current signal in cathodic contact glow discharge electrolysis,” *J. Appl. Phys.*, vol. 119, no. 20, p. 203303, 2016.

[50] A. I. Maksimov and A. V. Khlyustova, “Physical chemistry of plasma-solution systems,” *High Energy Chem.*, vol. 43, no. 3, pp. 149–155, 2009.

[51] K. Kobayashi, Y. Tomita, and M. Sanmyo, “Electrochemical Generation of Hot Plasma by Pulsed Discharge in an Electrolyte,” *J. Phys. Chem. B*, vol. 104, no. 26, pp. 6318–6326, 2000.

[52] A. G. and A. S. J Torres, J Jonkers, MJ van de Sande, JJAMvanderMullen, “An easy way to determine simultaneously the electron density and temperature in high-pressure plasmas by using Stark,” *J. Phys. D. Appl. Phys.*, 2003.

[53] M. D. Calzada, M. Moisan, a. Gamero, and a. Sola, “Experimental investigation and characterization of the departure from local thermodynamic equilibrium along a surface-wave-sustained discharge at atmospheric pressure,” *J. Appl. Phys.*, vol. 80, no. 1, p. 46, 1996.

[54] Y. Temiz, R. D. Lovchik, G. V. Kaigala, and E. Delamarche, “Lab-on-a-chip devices: How to close and plug the lab?,” *Microelectron. Eng.*, vol. 132, pp. 156–175, 2015.

[55] H. a Stone, “Microfluidics: Basic Issues, Applications, and Challenges,” *AIChe J.*, vol. 47, no. 6, pp. 1250–1254, 2001.

[56] S. T. NGUYEN, Nam-Trung et WERELEY, *Fundamentals and applications of microfluidics*, Artech Hou. 2002.

[57] K. Petersen, J. Brown, T. Vermeulen, P. Barth, J. Mallon, and J. Bryzek, “Ultra-stable, high-temperature pressure sensors using silicon fusion bonding,” *Sensors Actuators A. Phys.*, vol. 21, no. 1–3, pp. 96–101, 1990.

[58] A. Ben-Yakar, A. Harkin, J. Ashmore, R. L. Byer, and H. a Stone, “Thermal and fluid processes of a thin melt zone during femtosecond laser ablation of glass: the formation of rims by single laser pulses,” *J. Phys. D. Appl. Phys.*, vol. 40, no. 5, pp. 1447–1459, 2007.

[59] J. B. Werkmeister and A. H. Slocum, “Investigating Different Methods of Bonding Glass Substrates,” *ASPE Proc.*, p. 1597, 2004.

[60] H. Noh, K. Moon, A. Cannon, P. J. Hesketh, and C. P. Wong, “Wafer bonding using microwave heating of parylene intermediate layers,” *J. Micromechanics Microengineering*, vol. 14, no. 4, pp. 625–631, 2004.

[61] Y. Xu, C. Wang, Y. Dong, L. Li, K. Jang, K. Mawatari, T. Suga, and T. Kitamori, “Low-temperature direct bonding of glass nanofluidic chips using a two-step plasma surface activation process,” *Anal. Bioanal. Chem.*, vol. 402, pp. 1011–1018, 2012.

[62] “Sonoscan, sound technology with vision.” .

[63] Z. K. Wang, H. Y. Zheng, W. L. Seow, and X. C. Wang, “Investigation on material removal efficiency in debris-free laser ablation of brittle substrates,” *J. Mater. Process. Technol.*, vol. 219, pp. 133–142, 2015.

[64] G. Araya and G. Gutierrez, “Analytical solution for a transient, three-dimensional temperature distribution due to a moving laser beam,” *Int. J. Heat Mass Transf.*, vol. 49, no. 21–22, pp. 4124–4131, 2006.

[65] O. Manca, B. Morrone, and V. Naso, “Quasi-steady-state three-dimensional

temperature distribution induced by a moving circular gaussian heat source in a finite depth solid," *Int. J. Heat Mass Transf.*, vol. 38, no. 7, pp. 1305–1315, 1995.

[66] D. B. Darmadi, J. Norrish, and A. K. Tieu, "Analytic and Finite Element Solutions for Temperature Profiles in Welding using Varied Heat Source Models," *World Acad. Sci. Eng. Technol.*, vol. 57, pp. 154–162, 2011.

[67] A. Ghosh, S. Hloch, and S. Chattopadhyaya, "Critical Analysis of Moving Heat Source Shape for Arc Welding Process of High Deposition Rate," vol. 3651, 2014.

[68] M. Y. Ha, M. J. Jung, and Y. S. Kim, "Numerical study on transient heat transfer and fluid flow of natural convection in an enclosure with a heat-generating conducting body," *Numer. Heat Transf. Part A-applications*, vol. 35, no. 4, pp. 415–433, 1999.

[69] J. Kidawa-kukla, C. Science, and J. Kidawa-kukla, "Temperature Distribution in a Circular Plate," vol. 7, no. 1, pp. 71–76, 2008.

[70] R. Komanduri and Z. B. Hou, "Thermal analysis of the arc welding process: Part I. General solutions," *Metall. Mater. Trans. B*, vol. 31, no. 6, pp. 1353–1370, 2000.

[71] N. Laraqi, "An Exact Explicit Analytical Solution of the Steady-State Temperature in a Half Space Subjected to a Moving Circular Heat Source," *J. Tribol.*, vol. 125, no. 4, p. 859, 2003.

# Appendix

## Appendix A

The machining time, the optical sensor level and the machining head motion is recorded by the set-up all over the drilling process. The optical sensor level and the machining depth is recorded each 10ms during the drilling. A trigger using the optical sensor level is used to make sure the time recorded is during the drilling and not something else.

The evolution of the drilling over time is extracted from the optical sensor signal (Figure 75). When the tool-electrode touches the work-piece the optical sensor level drops and when drilling occurs the optical sensor level increases in function of the drilling speed. Therefore, the drilling speed is proportional to the optical signal evolution. In Figure 75 each saw tooth refer to a 37.5µm drilling depth. We clearly see the increase of the drilling speed of a step in function of the drilling depth.

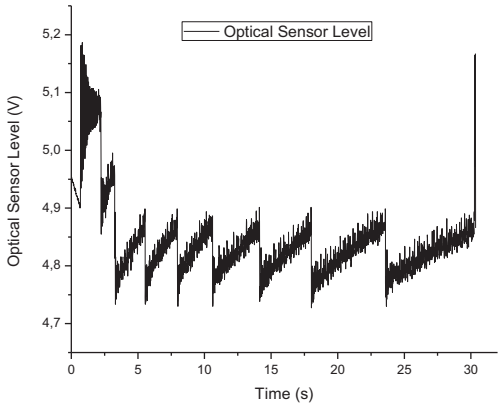


*Figure 75 : Optical sensor level during a hole drilling, the wideness of the curves shows the optical sensor signal noise.*